Coupled heat and water flow dynamics in dry soils.

Application to a multilayer waste cover.

Ph.D. Thesis

Hydrogeology Group (GHS)

Dept. of Geotechnical Eng. and Geosciences,

Technical University of Catalonia, UPC-BarcelonaTech.

Institute of Environmental Assessment and Water Research (IDAEA), CSIC.

Meritxell Gran Esforzado

Advisor:

Jesús Carrera Ramírez

Co-Advisor:

Maarten W. Saaltink

April, 2015

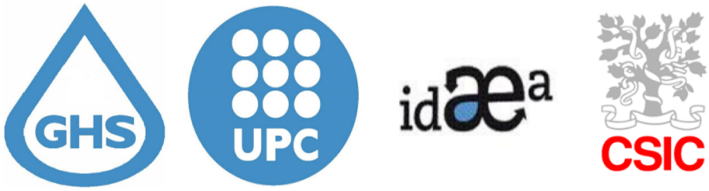

This thesis was funded by ENRESA (Spanish National Company for Nuclear Waste Management) in the framework of the project "Multiphase flow studies for the design of cover layers and the study of the evolution of cells". We also thank the financial support received from the EU WATCH project (WATer and global Change) and the Spanish Research Council ATRAPO project.

A mi familia

Abstract

Unsaturated flow plays an important role in numerous environmental phenomena. It is complex in arid regions, where liquid water fluxes are small and vapor fluxes become relevant, so that heat, water and solute mass transport are needed to understand evaporation. This thesis aims at gaining insight evaporation and vapor flow mechanisms and the relevance of matric potential, temperature and osmotic gradients.

These issues are especially relevant for soil salinization, whose mechanisms are poorly understood despite their global impact. We studied them in open soil evaporation column experiments. We found that a water separation process occurs in the soil. Above a very narrow evaporation front, the soil contains high salt concentrations due the solutes transported by the upward liquid flux and concentrated by evaporation. Below, concentrations are lower than the initial ones, because vapor flows downwards below the evaporation front driven by temperature gradients. Condensation of this downward vapor flux dilutes upflowing water, improving soil conditions and providing an area where root plants could live.

We modeled nonisothermal multiphase flow and reactive transport during the experiments to quantify the actual processes and to understand the nature of the downward vapor flux. Modeling required modifying the retention curve to represent oven dry conditions. Our model supports the traditional division of soil, by an evaporation front, into a dry region and a moist region. This view may suffice for evaluating evaporation rates and water mass balances, but not for assessing salt

processes, which require acknowledging that not only liquid water flow but also vapor diffusion occur below the evaporation front.

Unsaturated flow concepts control the design of covers to isolate solid waste. Their goal is to protect the waste from infiltration during long periods of time by promoting surface runoff and lateral drainage and by hindering biointrusion. Two cover designs were built, both consisting of an evapotranspiration layer, a biointrusion barrier and an infiltration barrier. We analyzed their performance for two years (2009 and 2010, which was very wet) by a thorough monitoring system. We conclude that the upper portion of one cover did work as planned, but the lower infiltration barrier did not, which suggests some design improvements: increase the retention capacity of the sand layers, include filter layers and facilitate lateral drainage by increasing the slope in the top area.

We studied the daily and annual variations of vapor fluxes using data from the covers. We find that most water flow in the top portion of the soil occurs in the gas phase. Vapor fluxes are controlled by temperature and follow its fluctuations, switching direction with a daily frequency and a depth dependent lag. Downward vapor fluxes are dominant during the summer and upward fluxes during the winter. Deeper into the soil, vapor fluxes vary seasonally, flowing almost constantly upwards during the cold season, and vice versa. Rainfall events have a cooling effect, reversing summer vapor fluxes. Yet, the net annual flux is downwards. Furthermore, an approximate analytical solution to calculate diffusive vapor fluxes at any depth, is presented. While vapor fluxes are quantitatively small, they may still represent a significant source of water during summer for shallow roots. Plants may attract water from hot zones around to the root zone, kept colder by the plant shadow and by transpiration.

Numerical modeling is also used to simulate one of the covers. Model output is compared to observations (suction and temperature), which are well reproduced in the top soil layers. The model does not reproduce the failure of the capillary barrier because it did not include gravity fingering, which explains flow through the coarse layer.

Resumen

La zona no satura juega un papel importante en numerosos fenómenos ambientales. Es complejo en zonas áridas, donde los flujos de agua líquida son pequeños y los flujos de vapor adquieren relevancia. El transporte de calor, de agua y de solutos es necesario para entender la evaporación. Esta tesis quiere mejorar el conocimiento sobre la evaporación y los mecanismos de flujo de vapor, y analizar la relevancia de los gradientes de succión, temperatura y osmóticos.

Estas cuestiones son especialmente relevantes para la salinización de suelos, cuyos mecanismos son poco conocidos a pesar de su impacto global. Hemos estudiado experimentos de columna de evaporación en los que se ha encontrado un proceso de separación de agua en el suelo. Por encima del frente de evaporación, que es muy estrecho, el suelo contiene altas concentraciones de sal debido a los solutos transportados por el flujo ascendente de líquido y su posterior evaporación. Por debajo, las concentraciones son inferiores a las iniciales, porque el vapor fluye hacia abajo desde el frente de evaporación impulsado por gradientes de temperatura. Allí condensa, causando la dilución del flujo ascendente de agua, mejorando las condiciones del suelo y proporcionando un área donde las raíces de las plantas podrían vivir.

Mediante un modelo de flujo multifásico no isotermo y transporte reactivo de los experimentos, se han cuantificado los procesos, para entender la naturaleza del flujo descendente de vapor. Se ha modificado la curva de retención para representar condiciones muy secas del suelo. Nuestro modelo es compatible con la división tradicional del suelo, por un frente de evaporación, en una

región seca y una región húmeda. Este punto de vista puede ser suficiente para la evaluación de tasas de evaporación y balances de masa de agua, pero no para la evaluación de los procesos de sales, que requieren no sólo el conocimiento del flujo de agua líquida, sino también la difusión de vapor por debajo del frente de evaporación.

Conceptos de flujo no saturado controlan el diseño de coberturas para aislar residuos sólidos. Su objetivo es proteger los residuos de la infiltración durante largos períodos de tiempo mediante la promoción de la escorrentía superficial y el drenaje lateral, y evitando la biointrusión. Dos diseños de cobertura, basados en una capa para la evapotranspiración, una barrera de biointrusión y una barrera de infiltración, fueron construidos. Analizamos su funcionamiento durante dos años a través de un completo sistema de monitorización. Se concluye que la parte superior de la cobertura funcionó como estaba previsto, pero no así la barrera de infiltración inferior. Se sugieren algunas mejoras de diseño: aumentar la capacidad de retención de las capas de arena, incluir capas de filtro y facilitar el drenaje lateral aumentando la pendiente en la zona superior.

Se han estudiado las variaciones diarias y anuales de los flujos de vapor a partir de datos de la cobertura y de modelación numérica. Encontramos que la mayor parte del flujo de agua en la parte superior del suelo se produce en la fase gaseosa. Los flujos de vapor son controlados por la temperatura y siguen sus fluctuaciones, cambiando de dirección diariamente y con un desfase que va en aumento con la profundidad. Los flujos de vapor descendente son dominantes durante el verano y los ascendentes durante el invierno. A mayor profundidad, los flujos de vapor varían estacionalmente, y fluyen casi constantemente hacia arriba durante las épocas frías, y viceversa. Las lluvias tienen un efecto de enfriamiento, revirtiendo los flujos de vapor en verano. El flujo neto anual es descendente. El modelo necesita simular flujo a través de vías preferenciales. Si bien los flujos de vapor son cuantitativamente pequeños, pueden representar una importante fuente de agua durante el verano para las raíces poco profundas. Se ha presentado también, una solución analítica para el cálculo de flujos difusivos de vapor en el suelo.

Resum

La zona no saturada juga un paper important en nombrosos fenòmens ambientals. És complex en zones àrides, on els fluxos d'aigua líquida són petits i els fluxos de vapor adquireixen rellevància. El transport de calor, d'aigua i de soluts és necessari per entendre l'evaporació. Aquesta tesi vol millorar el coneixement sobre l'evaporació i els mecanismes de flux de vapor, i analitzar la rellevància dels gradients de succió, de temperatura i osmòtics.

Aquestes qüestions són especialment rellevants per la salinització de sòls, els mecanismes són poc coneguts malgrat el seu impacte global. Hem estudiat experiments de columna d'evaporació on s'ha trobat un procés de separació d'aigua al sòl. Per sobre del front d'evaporació, que és molt estret, el sòl conté altes concentracions a causa dels soluts transportats pel flux ascendent de líquid i la seva posterior evaporació. Per sota, les concentracions són inferiors a les inicials, perquè el vapor flueix cap avall des del front d'evaporació impulsat per gradients de temperatura. Allà condensa, causant la dilució del flux ascendent d'aigua, millorant les condicions del sòl i proporcionant una àrea on les arrels de les plantes podrien viure. Mitjançant un model de flux multifàsic no isoterm i transport reactiu dels experiments, s'han quantificat els processos per entendre la naturalesa del flux descendent de vapor. S'ha modificat la corba de retenció per representar condicions molt seques del sòl. El nostre model és compatible amb la divisió tradicional del sòl, per un front d'evaporació, en una regió seca i una regió humida. Aquest punt de vista pot ser suficient per a l'avaluació de tases d'evaporació i balanços de massa d'aigua, però no per a l'avaluació dels processos de sals, que requereixen no només el coneixement del flux d'aigua líquida, sinó també la

difusió de vapor per sota del front d'evaporació. Conceptes de flux no saturat controlen el disseny de cobertures per aïllar residus sòlids. El seu objectiu és protegir els residus de la infiltració durant llargs períodes de temps mitjançant la promoció de l'escorrentia superficial i el drenatge lateral, i evitant la biointrusió. Dos dissenys de cobertura, basats en una capa per l'evapotranspiració, una barrera de biointrusió i una barrera d'infiltració, van ser construïts. Analitzem el seu funcionament durant dos anys a través d'un complet sistema de monitorització. Es conclou que la part superior de la cobertura va funcionar com estava previst, però no així la barrera d'infiltració inferior. Es suggereixen millores de disseny: augmentar la capacitat de retenció de les capes de sorra, incloure capes de filtre i facilitar el drenatge lateral augmentant el pendent a la zona superior. S'han estudiat les variacions diàries i anuals dels fluxos de vapor a partir de dades de la cobertura i de modelació numèrica. Trobem que la major part del flux d'aigua a la part superior del sòl es produeix en la fase gasosa. Els fluxos de vapor són controlats per la temperatura i segueixen les seves fluctuacions, canviant de direcció diàriament i amb un desfasament que augmenta amb la profunditat. Els fluxos de vapor descendent són dominants durant l'estiu i els ascendents durant l'hivern. A més profunditat, els fluxos de vapor varien estacionalment, i flueixen gairebé constantment cap amunt durant les èpoques fredes, i viceversa. Les pluges tenen un efecte de refredament, revertint els fluxos de vapor a l'estiu. El flux net anual és descendent. El model demana simular flux a través de vies preferencials. Si bé els fluxos de vapor són quantitativament petits, poden representar una important font d'aigua durant l'estiu per a les arrels poc profundes. S'ha presentat també, una solució analítica per al càlcul de fluxos difusius de vapor al sòl.

Agradecimientos

Agradezco a mi director, Jesús Carrera la oportunidad de trabajar y aprender con él. A mi co-director, Maarten W. Saaltink, su ayuda y paciencia. A los compañeros del Grupo de Hidrología Subterránea por los momentos compartidos. A los amigos de fuera y dentro de la universidad, por su apoyo y buenos ratos. A mi familia, por creer en mi y por apoyarme siempre.

Table of Contents

List of Figures

List of Tables

Chapter 1

Introduction

1.1 Motivation and Objectives

Unsaturated flow plays an important role in numerous environmental phenomena: quantification of water recharge and water resources, contaminant transport, soil salinization, desertification and many others. The phenomenon is complex because heat, water and solute mass transport occur simultaneously during evaporation. Suction, temperature and osmotic gradients control the multiphase system. Under dry conditions, there is little liquid water flux and recharge, but temperature and vapor pressure gradients can be large, so that vapor fluxes may become significant (*Ross*, 1984; *Scanlon and Milly*, 1994). Under these conditions, which are prevalent in arid countries, understanding evaporation and vapor flow mechanisms and the relevance of matric potential, temperature and osmotic gradients is crucial.

One of the major problems in most arid and semiarid regions is soil salinization (*Van-Camp et al.*, 2004). Evaporation from dry soils plays a role not only in the salinization of irrigated lands but also in the weathering of mine tailings (*Hammarstrom et al.*, 2005). The evaporation front is usually conceived as a gradual transition zone that divides the soil into two areas: above, the soil is

dry and water vapor flows upwards, below, water also flows upwards but in liquid phase (*Gowing et al.*, 2006; *Schneider-Zapp et al.*, 2010). Thus vapor flux is usually viewed as flowing upwards. But this needs not be always the case. *Scanlon* (1992) studied water vapor fluxes in desert soils and suggested the existence of a downward vapor flux driven by thermal gradients. *Scanlon and Milly* (1994); *Milly* (1996) corroborated these observations by a numerical model. *Nassar and Horton* (1989a) studied the combined effect of osmotic and temperature gradients and concluded that solute concentration affects water transport under nonisothermal conditions. The first objective of this thesis is to determine how matric potential, temperature and osmotic gradients interact between them and their impact on water vapor flow and salt concentration during an evaporation experiment. Experimental studies yield direct measurements of state variables (matric potential, water content or temperature) but not flow and phase change processes, which are the ones that are required for properly understanding the phenomenon. These must be indirectly inferred from state variable measurements, which is not easy when the phenomena are complex and coupled. Therefore, quantitative understanding of the above processes requires mathematical modeling.

Most models of evaporation focus on the interactions between water and heat flow (*Jackson et al.*, 1974; *Scanlon and Milly*, 1994; *Boulet et al.*, 1997), concluding that vapor flux is dominant near the surface where the soil is dry. *Gowing et al.* (2006) divided the soil into liquid flow and vapor flow zones separated by an evaporation front. Notwithstanding, these models do not consider the role of salinity. Other studies (*Nassar and Horton*, 1989b) simulated water transport in unsaturated nonisothermal salty soil, but salinity effects in theirs and other models have commonly been analyzed assuming dilute solutions, which is not suitable since vapor pressure in equilibrium with a salty aqueous phase is very sensitive to salinity (*Burns et al.*, 2006). Two other factors must be borne in mind when modeling evaporation from high salinity solutions. First, salts tend to precipitate in the pores (*Nachshon et al.*, 2011) and/or to form a low permeability crust that should be modeled (*Yakirevich et al.*, 1997). Second, under hot and/or dry conditions, the residual saturation of water in soil can no longer be considered a lower bound for saturation (*Milly and Eagleson*, 1982; *Rossi and Nimmo*, 1994; *Prunty*, 2003). A modification of the retention curve must there-

fore be considered to represent water contents under what is usually termed as oven dry conditions. A coupled nonisothermal multiphase flow and reactive transport model of the evaporation experiment was developed to describe the evolution and nature of evaporation-condensation, to evaluate the magnitude of the water fluxes and gain insight into the downward vapor flow mechanism and the relevance of suction, temperature and osmotic gradients.

One common application of unsaturated flow studies is the design of the soil cover systems to isolate solid waste. Soil covers are used worldwide at municipal and industrial landfills and at hazardous and radioactive waste disposal facilities (*Peng and Jiang*, 2009). Their main purpose is to protect the underlying waste from infiltration by promoting surface runoff and lateral drainage, hindering access of roots or animals and controlling moisture and percolation. Surface soil covers are designed in various forms, ranging from simple soil covers to multilayer systems, and relying on different mechanisms, from water-balance covers to hydraulic barrier covers. Cover systems based on resistive barriers in which infiltration is reduced by placing a layer with low saturated hydraulic conductivity, minimize water flux, but tend to leak due to biointrusion, differential subsidence and/or desiccation cracks (*Jessberger and Stone*, 1991; *Smith et al.*, 1997; *Dwyer*, 1998; *Albrecht and Benson*, 2001; *Albright and Benson*, 2003). Evapotranspirative covers rely on water storage principles. While they are effective barriers to percolation in most arid and semiarid environments (*Nyhan et al.*, 1990; *Gee et al.*, 1993; *Ward and Gee*, 1997; *Morris and Stormont*, 1997; *Dwyer*, 1997), they are highly dependent on vegetation which makes them less robust (*Scanlon et al.*, 2005), and less effective in humid climates (*Albright et al.*, 2004). Capillary barriers (fine-grained soil overlying a coarse-grained soil) promote storage in the overlying layer while maintaining the lower one dry. They have proven effective in restricting percolation in arid and semiarid environments (*Ward and Gee*, 1997; *Dwyer*, 1998; *Khire et al.*, 1999; *Scanlon et al.*, 2005) but may fail in wet climates (*Khire et al.*, 1999; *Albright and Benson*, 2003; *Abdolahzadeh et al.*, 2011). As other designs, they can also suffer from damage caused by biointrusion (*Khire et al.*, 1994; *Dwyer*, 2003). Our goal is to find the soil layer combination able to control infiltration, while preventing biointrusion, in a temperate climate where precipitation is highest in low evap-

oration periods. With this aim, we built up and analyzed two fully instrumented pilot field-scale covers.

As mentioned above, vapor fluxes play an important role in unsaturated soils, but they are complex to study under natural conditions because of (1) the high spatial and temporal variability of their direction and magnitude, (2) the low overall mass of water transferred, and (3) the limitations of the measurement techniques (*Scanlon et al.*, 1997). Annual vapor fluxes have been evaluated in desert soils through numerical modeling (*Milly*, 1996). Nevertheless, it is not clear if daily net vapor flows downwards only and always during the summer, or if rainfall episodes promote or hinder vapor flow, or if vapor flux changes in direction behave the same along the year. With the aim of gaining understanding of vapor flow behavior under natural weather conditions, we study it in detail (daily and annual variations) in the covers field-scale experiment.

As we did with the laboratory evaporation experiment, the soil cover is modeled mathematically. Numerical simulation allows a quantitative analysis of the water and energy fluxes and completes the gaps that resulted from the monitoring system. The performance of the two layer combinations and their effectiveness in hindering percolation are evaluated.

In summary, in this thesis we study the behavior of water and energy fluxes in soils under very dry conditions. To gain understanding in the evaporation and vapor flow mechanisms and the relevance of matric potential, temperature and osmotic gradients, two different scales are used, laboratory and field-scale, and two methodologies are applied, experiment and mathematical modelling.

1.2 Thesis Outline

This thesis consists of five chapters in addition to this introduction. Each chapter responds to each of the above mentioned objectives and is based on a paper that is published (chapter 2 and 3) or in preparation-publication process in international journals. Therefore, they can be read

independently. The reference to the papers is indicated in a footnote at the beginning of each chapter.

Chapter 2 contains an analysis of vapor flux and solute transport under evaporation conditions. Laboratory experiments consisted of open sand and silt columns initially saturated with epsomite ($MgSO_4 \cdot 7H_2O$) and halite ($NaCl$) solutions. Salt precipitation occurred only above the evaporation front, which took place within a very narrow band. Vapor flowed both upwards and downwards from this front. The downward vapor flow condensed further down the column, diluting the solution. This gave rise to two areas: a high salinity area above the evaporation front, and a diluted solution area below it. The effects of thermal, suction and osmotic gradients on water fluxes are studied in order to better understand the underlying mechanisms of this phenomenon.

Chapter 3 describes a coupled nonisothermal multiphase flow and a reactive transport model of the salty sand soil column. The model is calibrated with data from the evaporation experiment (volumetric water content, temperature and concentration). The retention curve and relative permeability functions are modified to simulate oven dry conditions. Results show that evaporation is controlled by heat, and limited by salinity and liquid and vapor fluxes. Below evaporation front vapor flows downwards controlled by temperature gradient and thus generates a dilution. Vapor diffusion and dilution are strongly influenced by heat boundary conditions.

Chapter 4 describes the two pilot waste covers, Test I and Test II, that have been built and largely instrumented at El Cabril (Córdoba, South Spain). Their performance was monitored during two years. Both covers consist of (1) an evapotranspiration layer, (2) a biointrusion barrier and (3) an infiltration barrier, but they present different layer combinations. The analysis of the instrumentation suggests that the top layers (the evapotranspiration layers on top of the biointrusion barrier) act in both covers as a capillary barrier hindering water flux into the clay layer in Test I during the first year, but not during the second, which was anomalously wet. The capillary barrier failed both years in Test II. A portion of this infiltrated water flows through the clay and after the second year reaches the layer at the base of the covers but without saturating it.

Chapter 5 focuses on the effect of thermal gradients and rainfall events on the diffusive vapor fluxes in a dry soil. Vapor fluxes have been calculated from the temperature and relative humidity data recorded by the monitoring system installed in the soil cover. Daily and annual vapor flux variations have been studied in detail. An approximate analytical solution to calculate vapor fluxes at any depth has been developed and good results are obtained from the comparison with the field data. Results show that rainfall events have a cooling effect, switching the direction of vapor pressure gradients and leading to a larger and upward vapor fluxes. Nevertheless, these upward fluxes do not counteract the summer downward fluxes and the direction of the net annual vapor flux below the evaporation front is downwards.

Chapter 6 contains a description of the nonisothermal multiphase flow model of Test II. The model is calibrated with data from the monitoring system (suction and temperature) and two years are simulated. Results show that the upper layers are retaining the water from the rainfall events. In fact, the model simulates the capillary barrier effect that they form with the underlying materials so well that no water infiltrates in the layers below. As we know from measured data, water overcomes the capillary barrier in the field. This difference is because water flow through this underlying layer occurs via preferential flow and this mechanism is not present in our numerical model.

The main contributions of this thesis are summarized in Chapter 7.

Chapter 2

Dynamics of water vapor flux and water separation processes during evaporation from a salty dry soil*

2.1 Introduction

Evaporation under very dry conditions may cause salt precipitates, leading to land degradation and desertification. Since dry conditions can be found in most arid and semiarid regions it is not surprising that soil salinization is a major global environmental problem (*Van-Camp et al.*, 2004). Evaporation from dry soils plays a role not only in the salinization of irrigated lands but also in the weathering of mine tailings (*Hammarstrom et al.*, 2005). The phenomenon is complex because heat, water and solute mass transport occur simultaneously during evaporation. Therefore, suction, temperature and osmotic gradients are expected to interact and to control the multiphase system which explains why the detailed mechanisms of soil salinization are poorly understood.

*This chapter is based on the paper with the same title published in Journal of Hydrology 396 (2011) 215-220, doi:10.1016/j.jhydrol.2010.11.011

Evaporation is usually conceived by dividing the soil into two zones separated by an evaporation front: above, the soil is dry and water vapor flows upwards, below, water also flows upwards but in liquid phase (*Gowing et al.*, 2006). *Konucku et al.* (2004) broadened this description by adding a transition zone where water flows in both the liquid and vapor phases while excluding the possibility of a sharp evaporation front.

Still, water vapor is viewed as flowing upwards. Actually, this is not always the case. *Scanlon* (1992) studied water vapor fluxes in desert soils using ^{36}Cl and ^{3}H distributions. Chlorine 36 flux is restricted to the liquid phase, while tritium can flow in both the liquid and vapor phases. Differences between ^{36}Cl and ^{3}H distributions suggested the existence of a downward vapor flux driven by thermal gradients. *Scanlon and Milly* (1994); *Milly* (1996) corroborated these observations by a numerical model. *Boulet et al.* (1997) obtained similar results.

Soluble salts (chlorides and sulphates of sodium, calcium and magnesium) are commonly present (*Abrol et al.*, 1988) and evaporation leads to high solute concentrations. Therefore, the osmotic effects must also be taken into account. This has motivated numerous experimental studies on the effect of thermal and osmotic gradients. *Wheeting* (1925) conducted closed horizontal experiments on columns divided into three zones: unsaturated soil with a high salinity solution, unsaturated soil with a diluted solution and an air gap that separates them. Interpreting Wheeting's experimental results, *Kelly and Selker* (2001) concluded that water activity was reduced in the saline portion, leading to a drop in vapor pressure that drove vapor flux. The air gap diminished this vapor flux. Therefore, they concluded that these processes should be studied in a continuous soil medium. In fact, *Scotter* (1974) had placed crystalline salts at one end of a sealed tube of initially uniformly wet soil under isothermal conditions. He obtained an increase in the water content in the salt zone owing to vapor transport by osmotic effects. The join effect of temperature and salinity gradients was studied by *Nassar and Horton* (1989a), who found that solute concentration affects unsaturated soil water transport also under nonisothermal conditions. A temperature gradient in horizontal closed columns was imposed by *Nassar and Horton* (1989a,b). They observed a

liquid water flow from the cold to the hot end, which offsets a water vapor flow in the opposite direction. These data were used by *Yakirevich et al.* (1997) to test their mathematical model. They highlighted the osmotic effects and proposed a salt crust formation. In fact, *Olivella et al.* (1996a), modeled porosity variatons induced by salt precipitation.

In summary, matric potential, temperature and osmotic gradients can drive vapor and liquid water fluxes, often in opposite directions. One may conjecture that evaporation in bare, dry and salty soil will be controlled by the superposition of these effects, but it has never been studied in detail. The aim of this paper is to determine how all these factors interact between them and their impact on water vapor flow and salt concentration. To this end, an open soil column experiment was performed.

2.2 Materials and Methods

Laboratory experiments were performed on initially saturated soil columns. Sand and silt columns with varying concentrations of epsomite ($MgSO_4 \cdot 7H_2O$) and halite ($NaCl$) were used. In order to achieve controlled and uniform conditions, evaporation was forced by an infrared lamp simulating the effect of the sun. Columns were periodically weighed to monitor evaporation loss.

To study the soil under very dry conditions, the experiment continued until the overall saturation fell to 0.32 and the evaporation had diminished. At this stage, the columns were dismounted to measure temperature, salinity and water volume content versus depth.

2.2.1 Materials

The columns consisted of methacrylate cylinders, 24 cm long and 14.4 cm in diameter enveloped in a thermal insulator (*Termoflex*, 2 cm thick). These cylinders were filled either with silica sand of 0.4-0.8 mm grain size and 2.65 g/cm^3 density or with aluminuous silt (Eijkelkamp) of particle size

about 73μ and $3.96g/cm^3$ density. Four different salt solutions were employed, two with epsomite ($40g/kg$ for a high solute concentration and $14g/kg$ for a low solute concentration) and two with halite ($20g/kg$ for a high solute concentration and $7g/kg$ for a low solute concentration). It should be noted that solute masses of the two salts are comparable because half of the epsomite molecular weight is water. Evaporation was forced by an infrared lamp (Philips PAR38 IR 175R) located 38 cm above the column surface (Figure 2.1) so that radiation at the soil surface was designed to be approximately $90mW/cm^2$, similar to the summer radiation at mid-latitudes.

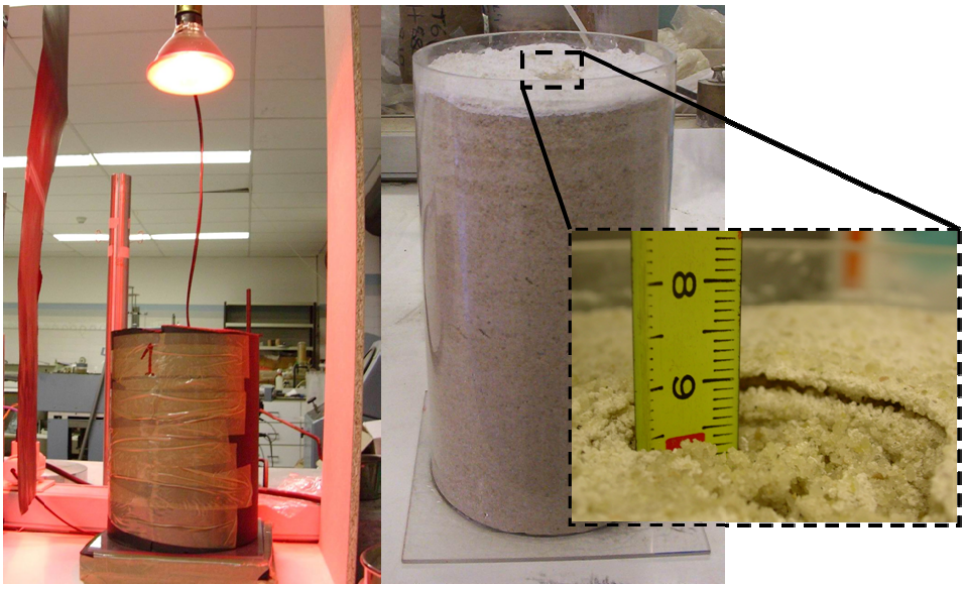

Figure 2.1: Experimental set up. Left, initial setting under the infrared lamp with the column enveloped in a thermal insulator. Right, the column at the end of the experiment, when the sand is dry and an epsomite crust has formed at the surface. Note the detail of this crust where we can observe its width and an air gap between the top of the sand and the salt crust. Consequently the salt crust grows upwards.

2.2.2 Column set up

A synthetic initial solution was created by adding the salt to distilled water. The material (sand or silt) was first mixed with this salt solution and columns were filled with layers that were compacted ($\approx 0.01\ kg/cm^2$) to eliminate air bubbles. The column weight was monitored daily for weight loss

due to evaporation. Relative humidity (RH) and temperature (T) in the laboratory were recorded ($RH \approx 52\%$ and $T \approx 24\,\mathrm{C}$). Profiles of state variables versus depth were collected at the end of the experiment. In order to obtain the time evolution we also set up a group of identical sand columns (four with a low epsomite concentration and four with a low halite concentration), which were dismantled at different stages of the experiment. These columns were dismantled sequentially after reaching average saturation degrees of 74%, 50%, 40% and 32%. This procedure was duplicated to test its repeatability.

2.2.3 Column dismantling

The temperature profile was measured prior to dismantling. To this end, we perforated the soil and introduced a thermal sensor, recording the temperature from top to bottom while the columns were still under the lamp. Thereafter, the salt crust was removed from the surface. Soil samples were then collected by means of a beveled iron ring (3 cm in diameter and 1.5 cm long) every 2.5 cm, approximately. All the samples including the salt crust, were weighed, dried in an oven at 110 C for 24 hours and weighed again. The water content along the column was derived from the weight difference. Next, each sample was diluted by adding a mass of water five times that of the sample mass and the electrical conductivity (EC) of its solution was measured. The salt concentration was obtained from a specifically calibrated EC-concentration relationship. The total mass of dissolved salt was deduced from electrical conductivity measurements after calibration with a given salt concentration solution.

The resulting mass concentration includes both the dissolved and precipitated salts. The salt concentration was calculated by dividing the total mass of salt and the water content by weight. The salts are assumed to be dissolved when the concentration before dilution is lower than the solubility of the salt. Should the dilution be higher, the excess is regarded as a salt precipitate. In the case of epsomite, this task is complicated by the high hygroscopy of $MgSO_4$. Magnesium sulphate presents six different mineral phases depending on its degree of hydration: ep-

somite ($MgSO_4 \cdot 7H_2O$), hexahydrite ($MgSO_4 \cdot 6H_2O$), pentahydrite ($MgSO_4 \cdot 5H_2O$), starkeyite ($MgSO_4 \cdot 4H_2O$), sanderite ($MgSO_4 \cdot 2H_2O$) and kieserite ($MgSO_4 \cdot H_2O$). These phases are rather unstable (hydrated phases evolve rapidly to dry phases and vice versa) with the result that they are not easy to analyze. Therefore, the ratio between $MgSO_4$ and H_2O molar masses (M and W, respectively) was used to distinguish the mineral phases. If W:M=4, the mineral phase is considered to be starkeyite, if W:M=5, it is pentahydrite, if W:M=6, it is hexahydrite and finally, if we have W:M=7, the precipitate is epsomite. If W:M>7, the amounts of precipitate and liquid water are derived by assuming that the solution is in equilibrium with an epsomite precipitate. If the molar mass ratio is between two phases, both are assumed to coexist.

2.3 Results and Discussion

The results of the experiments are first presented in terms of cumulative evaporation (Figure 2.2).

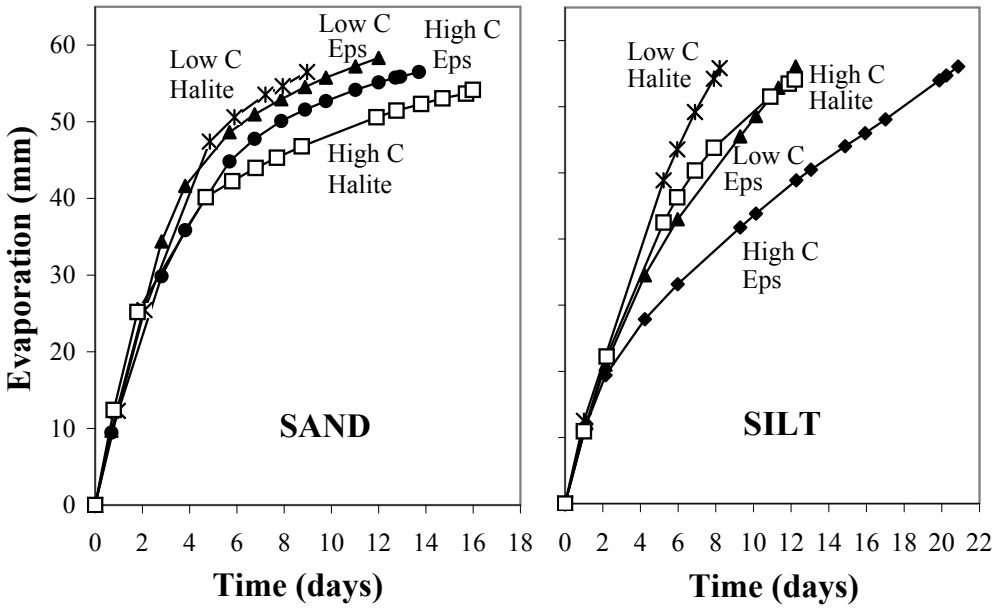

Figure 2.2: Time evolution of cumulative evaporation in sand columns on the left, and silt columns on the right. Note the fall in evaporation with the increase in concentration.

In general, evaporation is consistently slower in epsomite than in halite solutions, except in the

sand column with a high concentration of epsomite. This behaviour reflects the fact that water activity in the epsomite saturated solution (and consequently the vapor pressure and the evaporation rate) is lower than in the halite saturated solution. The reduction in water activity with increasing concentration also explains why low concentration solutions evaporated faster. Epsomite precipitates form continuous hard salt crusts on the column surface (right image in Figure 2.1) whereas halite precipitates form discontinuous easily friable crusts.

Profiles of the volumetric water content, salt concentration and temperature at the end of the experiment are displayed in Figure 2.3.

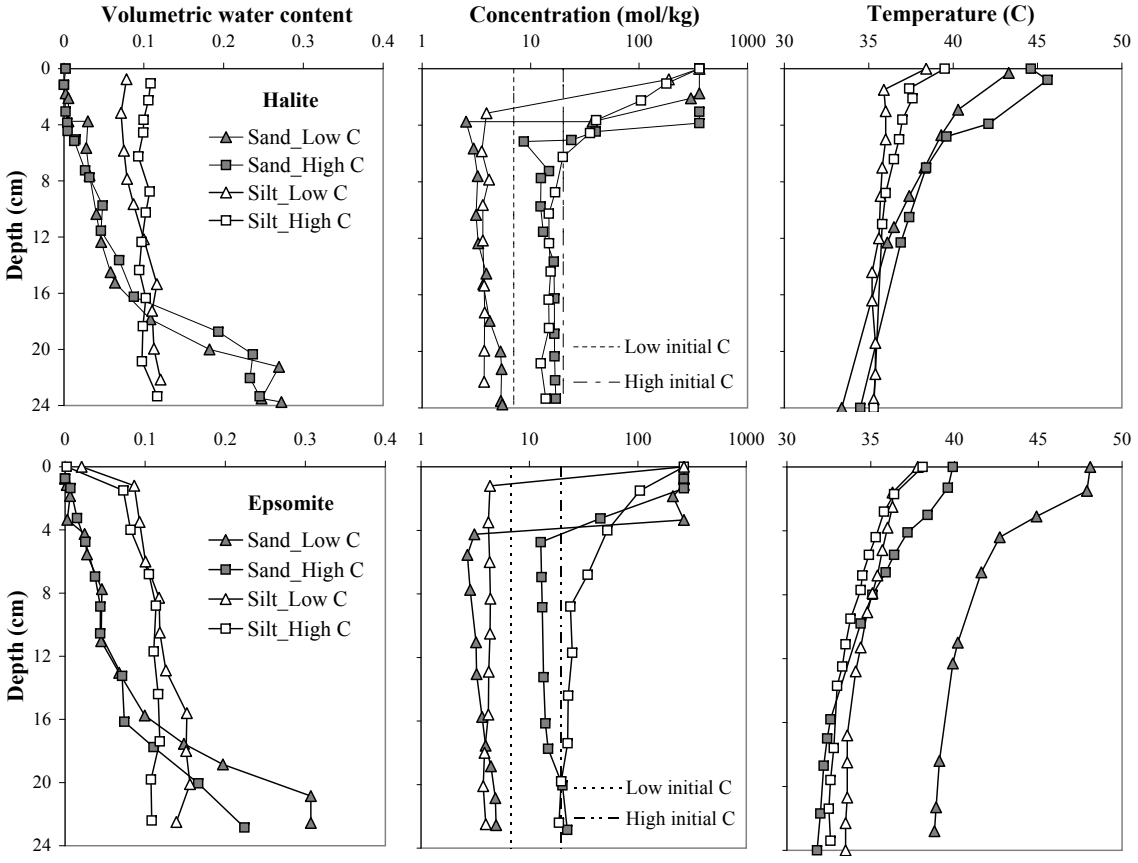

Figure 2.3: Profiles of volumetric water content, salt concentration and temperature at the end of the experiment. Halite for the upper graphs and epsomite for the lower. Solid and hollow symbols represent sand and silt columns, respectively. Concentration values that equal the salt solubility are displayed for the uppermost dry samples with precipitates.

As expected, volumetric water contents differ in the sand and silt columns. The distinctive retention curves of these materials generate different water content profiles. The profile is almost homogeneous in the silt columns whereas an oven dry zone at the top 4*cm* develops in the sand columns. Water content increases abruptly underneath below this oven dry area. This sudden increase appears to show the location of a sharp evaporation front at 4cm depth, which is at odds with *Konucku et al.* (2004), who proposed a broad evaporation zone. Below the evaporation front, the water content increases with depth, resembling the shape of the sand retention curves.

The salt concentration profiles are also different in the sand and the silt columns. Both the sand and the silt profiles exhibit high concentration values in the upper zone, reaching salt solubility and giving rise to precipitates. Below the area of precipitates, concentrations fall below initial values. In the case of the sand columns, the fall is sudden, with salt saturated samples immediately above the samples with concentrations markedly below the initial ones. The fall in concentration coincides with the increase in water content, thus corroborating the above hypothesis of a sharp evaporation front. These concentration values remain lower than the initial ones throughout the column, increasing slightly towards the bottom in the sand columns, but remaining constant towards the base in the silt columns. These unexpected values below the initial concentration can only be explained by condensation, which is most pronounced just below the evaporation front in the sand columns.

The temperature profiles also show significant differences. The temperature range is consistently narrower in the silt than in the sand columns. Temperature in the former only increases at the surface. The sand columns consistently show higher temperatures at the surface and an abrupt change of slope at 4cm depth, where the evaporation front is located. That is, the sand temperature profiles display two different gradients coinciding with the different water content zones. The gradient is high in the dry zone, which reflects the high heat flux and the low thermal conductivity of the dry sand. Below the evaporation front, the soil is wetter, so that its thermal conductivity is higher (*Gens et al.*, 2009). More importantly, the heat flux is much smaller because most of the

downwards heat has been used for evaporation. Both factors (increase in thermal conductivity and decrease in heat flux) contribute to the marked fall in the temperature gradient below the evaporation front. Nevertheless, the temperature gradient in the sand columns remains significantly larger than in the silt columns.

The time evolution of water content, salt concentration and temperature profiles for the sand columns with low concentrations of ($MgSO_4$) or ($NaCl$) are shown in Figure 2.4.

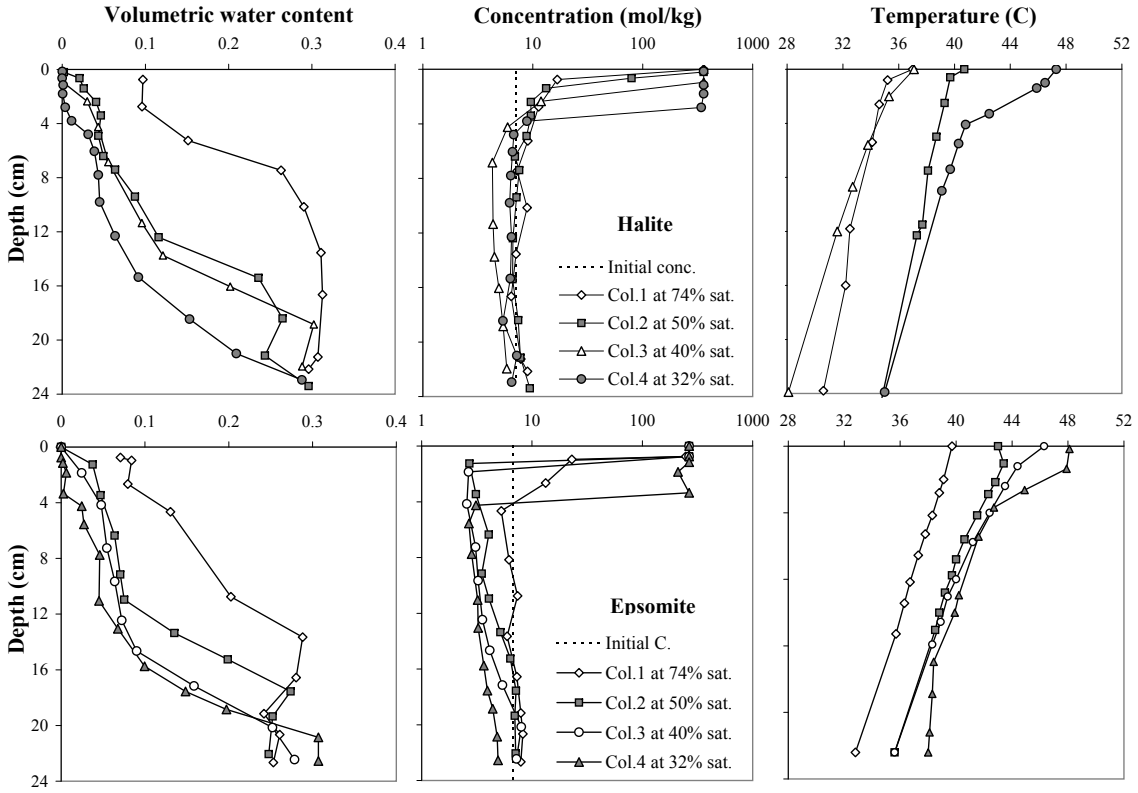

Figure 2.4: Profiles of volumetric water content, salt concentration and temperature profiles for sand columns with low concentration of $NaCl$ (above) or $MgSO_4$ (below) at four sequential stages of desaturation.

Both salts produce similar water content profiles. The columns desaturate especially near the surface and the evaporation front advances deep into the soil. The evaporation front is fed by a reducing flux of liquid from the bottom. Water vaporizes and diffuses to the surface at this front. Contrary to the prevailing belief, all evidences suggests that evaporation is restricted to a very

narrow zone.

In halite columns, concentration profiles show that the high concentration zone grows with time, advancing in depth with the evaporation front and increasing the oven dry area. The sharp fall in concentration below the evaporation front is observed from the early stages. The minimum in concentration is always immediately below the location of the evaporation front derived from water content and temperature profiles. The evolution of low concentration values shows an increased dilution, i.e. low concentrations fall and increase their extension with time.

The time evolution of $MgSO_4$ mineral phases is consistent with the concentration evolution. Precipitates at the surface dehydrate first, followed by the ones that precipitated immediately below at 0.8cm depth. Therefore, the wettest columns present the most hydrated mineral phases (see Table 1). Only the driest column (32% of saturation) at 0.8cm constitute an exception. Column 1 (at 74% of saturation) contains virtually no precipitates.

Table 2.1: $MgSO_4$ salt precipitates found at the surface and at 0.8cm depth, using the ratio between $MgSO_4$ and H_2O molar masses (M and W, respectively) to distinguish the mineral phases.If W:M=7, it is epsomite ($MgSO_4 \cdot 7H_2O$), W:M=6 is hexahydrite ($MgSO_4 \cdot 6H_2O$), W:M=5 is pentahydrite ($MgSO_4 \cdot 5H_2O$) and W:M=4 is starkeyite ($MgSO_4 \cdot 4H_2O$). If the molar mass ratio value is between two phases, both are assumed to coexist.

	W:M		
Depth (cm)	Column2 (50%Sat)	Column3 (40%Sat)	Column4 (32%Sat)
0	5.1	4.5	4.2
0.8	5.2	4.8	5.4

As regards the temperature profiles (Figure 2.4), their time evolution shows that temperature is consistently highest at the surface and the overall temperature increases with time as the soil dries with the exception of halite Column 3. The location of the change in the temperature profile also falls with time while the temperature gradient increases in the upper zone. The evolution of

this gradient coincides with the advance of the evaporation front in the water content profiles and the concentration zone.

2.4 Conclusions

The interactions between the controlling processes warrant a joint discussion. Water content and concentration profiles imply an upward flowing liquid flux as a result of capillarity. This liquid flux transports solutes by advection to the upper zone of the soil where evaporation causes a dramatic increase in concentration. Halite and epsomite precipitate when the solution attains salt solubility. A hard continuous salt crust is formed at the surface of the epsomite columns. The crust brings about changes in soil properties, reducing porosity, increasing thermal conductivity and decreasing water vapor diffusivity. As a result, the evaporation rate diminishes. Despite the fact that crust formation coincides with the fall in the evaporation rate, it cannot be considered to be the main cause of evaporation reduction because halite columns, whose crusts are discontinuous, display a similar reduction in the evaporation rate.

The sand columns desaturate progressively at the top until they become so dry that the evaporation from liquid water can no longer occur at the surface but at the front below the surface. In fact, oven dry conditions prevail above the evaporation front. Below this front, the water content falls to values near residual saturation. This suggests that the drop in the unsaturated hydraulic conductivity due to the reduction in the water content is what controls the location of the evaporation front. The front recedes downwards when the liquid flux cannot sustain the evaporation rate. At this stage, the little water remaining in the soil in oven dry conditions still evaporates. Evaporation causes the concentrations to increase and the water film around soil grains to disappear and prevent solute transport downwards. This may account for the sharp increase in concentration in the sand columns.

Above the evaporation front, water flows in the vapor phase, but again several processes in-

teract. Near the front, vapor pressure is affected not only by temperature but also by suction and concentration that will be very high. Close to the column top, gas pressure is controlled by the top boundary. The increased temperature causes a drop in vapor density, which drives the vapor flux upwards. In the case of epsomite columns, surface vapor density is also affected by the mineral phases that dehydrate as the column dries up. The small difference between the evaporation rate of low and high initial concentrations in the epsomite sand columns (Figure 2.2) may be attributed to this fact. High initial concentrations generate more salt precipitates that require water for their formation. This water remains in the mineral phase until evaporation forces the dehydration of the minerals. Halite columns behave differently and the evaporation rates are sensitive to the initial concentration of the solution. Factors such as the albedo of the crust were not considered at this stage.

The most striking result of these experiments is the marked reduction in concentrations below the evaporation front. Such a reduction demands the presence and condensation of a significant downward vapor flux, which is consistent with *Scanlon* (1992). As pointed out by this author, as well as by *Scanlon and Milly* (1994) and *Milly* (1996), the increase in vapor pressure at the evaporation front due to high temperatures leads inexorably to a downward vapor flux. Nevertheless, the increase in salinity causes an unstable situation (denser water on top) which might be expected to generate high salinity gravity fingers downwards. This counteracts the effect of the dilution that was observed for a high initial concentration of the epsomite silt column (Figure 2.3). The foregoing discussion suggests that fingering, should it occur, must be limited to the early evaporation stages.

Once an evaporation front develops below the surface, high salinities are restricted to very low water contents, which hinders liquid water fluxes and, hence, salt transport. This together with the downward vapor flux explains why the vast majority of columns display a significant dilution.

The shape of concentration profiles is different in the sand and the silt columns. The lower concentration immediately below the evaporation front of the former suggests greater condensa-

tion in the sand columns than in the silt columns. We attribute these differences to two interacting phenomena. First, the water content increases with depth in the sand columns, which inhibits downward diffusion, whereas the nearly uniform profiles of silt (owing to its higher capacity for water retention) allow condensation throughout the column. Second, the temperature gradient below the evaporation front remains fairly high in the sand columns, which promotes condensation and minimum concentrations immediately below this front.

From the foregoing discussion it is clear that a water separation process occurs in the unsaturated zone of the soil. On the one hand, there is an area above the evaporation front with high concentrations fed by salts transported from below and concentrated by evaporation. On the other hand, there is an area below the evaporation front that shows a diluted solution with concentration values lower than the initial one. One of the keys to understanding these processes is the evaporation front. It can be inferred that this front is very narrow. Vapor flows not only upwards from this front because of capillarity gradients but also downwards to the bottom of the column owing to temperature gradients. Condensation of this downward vapor flux accounts for this dilution.

Chapter 3

Modeling evaporation processes in a saline soil from saturation to oven dry conditions*

3.1 Introduction

Understanding evaporation is necessary in many fields of earth system sciences (*Shuttleworth*, 2007). In fact, soil evaporation is crucial in controlling the balance of soil-surface water and energy in arid and semiarid areas (*Saito et al.*, 2006). The actual mechanisms controlling evaporation are intricate (*Sakai et al.*, 2009). Soil evaporation may be controlled by the soil-atmosphere boundary layer when the soil is moist or by hydraulic conditions when it is dry (*Schneider-Zapp et al.*, 2010). In the latter case, evaporation causes the soil to dry and heat up causing liquid, vapor and heat fluxes to interact. The presence of solutes increases the complexity of the system and exacerbates the consequences, leading to salinization.

*This chapter is based on the paper with the same title published in Hydrol. Earth Syst. Sci. (HESS),15, 2077-2089, 2011, doi: 10.5194/hess-15-2077.2011

A number of researchers have analyzed this problem from an experimental perspective (*Wheeting*, 1925; *Scotter*, 1974; *Nassar and Horton*, 1989b; *Scanlon*, 1992). They conclude that water flux in dry and salinized soils is controlled by salinity and temperature gradients. Salinity causes water activity to drop, thus reducing vapor pressure in equilibrium with liquid water and driving vapor towards the saltier zone. Evaporation depends also on temperature and absorbs energy. Thereby, evaporation is affected by water flow and energy and solutes transport. The interaction of matric potential, temperature and salinity gradients under very dry conditions was studied by *Gran et al.* (2011), who observed salinity to decrease below the evaporation front, which they attributed to condensation of downward vapor flux. Unfortunately, experimental studies do not yield direct measurements of flow and phase change processes, which must be indirectly inferred from state variable measurements. This is not easy when the phenomena are complex and coupled. Therefore, quantitative understanding of the above processes requires mathematical modeling.

Most models of evaporation focus on the interactions between water and heat flow (*Jackson et al.*, 1974; *Scanlon and Milly*, 1994; *Boulet et al.*, 1997). These authors conclude that vapor flux is dominant near the surface where the soil is dry, and that water flows in the liquid phase below the evaporation front. A good approximation to water table evaporation under isothermal conditions was obtained by *Gowing et al.* (2006), who divided the soil into liquid flow and vapor flow zones separated by an evaporation front. The width of this front is subject to debate: *Gran et al.* (2011) observed a sharp front, whereas *Konucku et al.* (2004) concluded that a sharp phase transformation could not be expected. Notwithstanding, these models do not consider the role of salinity.

The effect of high salinities was modeled by *Nassar and Horton* (1989b), who simulated water transport in unsaturated nonisothermal salty soil on the basis of steady-state heat and mass transfer. Ironically, salinity effects in theirs and other models have commonly been analyzed assuming dilute solutions, which is not suitable since vapor pressure in equilibrium with a salty aqueous phase is very sensitive to salinity (*Burns et al.*, 2006). This explains the difficulties encountered

by *Nassar et al.* (1992) when modeling evaporation from salty solutions.

In addition to the effect of salinity or water activity, two other factors must be borne in mind when modeling evaporation from high salinity solutions. First, salts tend to precipitate in the pores (*Nachshon et al.*, 2011) and/or to form a low permeability crust that should be modeled (*Yakirevich et al.*, 1997). Crust formation was modeled but not compared with experimental data by *Olivella et al.* (1996b) and both modeled and compared with data by *Fujimaki et al.* (2006) though assuming isothermal conditions. Second, under hot and/or dry conditions, the residual saturation of water in soil can no longer be considered a lower bound for saturation (*Milly and Eagleson*, 1982; *Rossi and Nimmo*, 1994; *Prunty*, 2003). A modification of the retention curve must therefore be considered to represent water contents under oven dry conditions.

The emerging picture is complex. A nonisothermal multiphase flow model is necessary to distinguish advective and diffusive vapor fluxes. High concentrations near the surface require using non ideal solution chemistry (e.g. Pitzer) to simulate osmotic effects on vapor pressure and salt precipitation. Mass balances of water, air, heat and solutes are necessary and the effects of thermal, suction and salinity gradients must be simulated interacting simultaneously. Furthermore, traditional continuum mechanics descriptions (using Darcy and Ficks Laws, or concepts such as retention curve) may not suffice to include energy concepts. For instance, the role of film flows and the use of an enhancement factor for vapor diffusion are controversial. On one hand, molecular dynamics simulations (*Odelius et al.*, 1997) and experimental observations (*Hu et al.*, 1995; *Miranda et al.*, 1997) suggest that adsorbed water may display a nearly crystalline structure (water would be virtually immobile). On the other hand, *Rakhmatkariev* (2006) argues that the mobility of water adsorbed onto muscovite is only slightly less than in the bulk liquid, and *Shokri et al.* (2010) describe a continuous water film feeding the evaporation front. There is also discussion in the use of an enhancement factor for vapor diffusion (*Heitman et al.*, 2008; *Sakai et al.*, 2009) or the need for the Dusty Gas Model (*Thorstenson and Pollock*, 1989). Representing these concepts in the presence of high salinity and temperature gradients is currently under

investigation. Therefore, the question is whether the traditional continuum mechanic model can represent the processes involved in soil salinization. To this end, the experiments of *Gran et al.* (2011) are ideal since they are relatively simple (independently characterized homogeneous sand and controlled boundary conditions) and all relevant state variables (water content, temperature and salinity) were measured. Yet, they appear to be sensitive to all of the above processes.

Therefore, the aim of this work is to test whether traditional models can be used to reproduce the experiments of *Gran et al.* (2011) in order to a) evaluate the magnitude and direction of the water fluxes and gain a greater understanding of the downward vapor flow mechanism, b) describe the evolution and location of condensation-evaporation, and c) to assess the relevance of the matric potential, temperature and osmotic gradients in controlling the aforementioned water separation process.

3.2 Evaporation Experiment and Conceptual Model

Laboratory experiments consisted of open sand columns initially saturated with a 14g/kg epsomite ($MgSO_4 \cdot 7H_2O$) solution. Evaporation was forced by an infrared lamp so that radiation at the soil surface was similar to the summer radiation at mid-latitudes. The experiment continued until the overall saturation fell to 0.32, which was identified after preliminary tests to ensure the occurrence of a well developed crust and a deep evaporation front to allow the study of vapor fluxes. At this stage, the columns were dismounted to measure vertical profiles of temperature, volumetric water content and solute concentration. Two groups of four identical columns were dismounted at different times to obtain the time evolution of those profiles. These columns were dismantled sequentially after reaching saturations of 74% (after 2 days of evaporation), 50% (after 4 days), 40% (5 days) and 32% (12 days).

Both column experiments and results are described in *Gran et al.* (2011) and a diagram is shown in Figure 3.1.

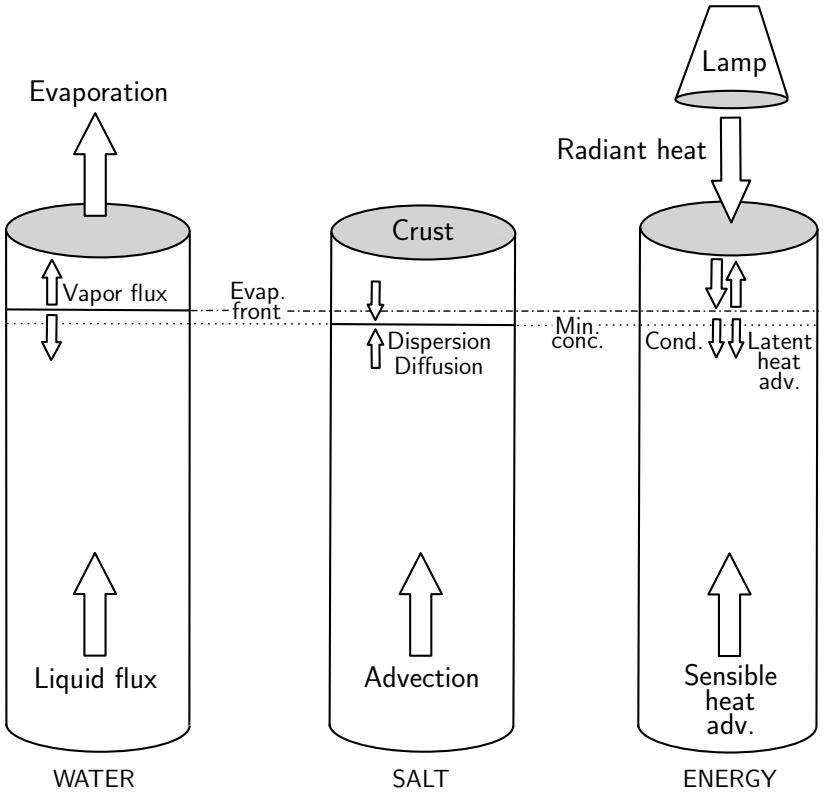

Figure 3.1: Diagram of the design of the evaporation column experiments and their conceptual model. The water fluxes are on the left, the salt fluxes are on the center and the energy ones on the right. The dashed and point lines show the location of the evaporation front and the minimum in salt concentration respectively.

The conceptual model emerging from these experiments requires tighly coupled processes. Capillarity brings about an upward liquid flux and soil drying. The liquid flux transports solutes by advection towards the top, where evaporation leads to a dramatic increase in concentration. A continuous salt crust is formed at the surface. This leads to changes in soil properties increasing thermal conductivity and reducing porosity and vapor diffusivity. Evaporation also reduces the water content and the unsaturated hydraulic conductivity causing the evaporation front to move downwards. Oven dry conditions (i.e. water content well below residual saturation) prevail above the evaporation front. Measurements suggest that this front is very narrow. A water separation process occurs at the front. On the one hand, concentrations are high above the front, where water flow is restricted to vapor phase. On the other hand, underneath the evaporation front,

concentrations are diluted below the initial values. Dilution is probably a result of the vapor pressure increase at the front caused by evaporation. Below the front, the temperature and vapor pressure gradient lead to a downward vapor flux. That is, vapor flows not only upwards from the evaporation front but also downwards. Condensation of this downward vapor flux causes the dilution.

3.3 Processes and Governing Equations

The system is governed by thermohydraulic and geochemical processes. To simulate them, it is necessary to study water flow and heat and reactive transport. Changes in porosity, thermal conductivity, permeability and water activity caused by water content reduction and salt precipitation should be simulated as well as vapor pressure variations in response to changes in water activity. Moreover, the precipitates present in the system (epsomite $MgSO_4 \cdot 7H_2O$, hexahydrite $MgSO_4 \cdot 6H_2O$, pentahydrite $MgSO_4 \cdot 5H_2O$ and starkeyite $MgSO_4 \cdot 4H_2O$) are highly hygroscopic. Therefore, hydratation-dehydratation of the mineral phases must be considered in the mass water balance.

3.3.1 Thermohydraulic Processes

The thermohydraulic model focuses on the mass balance of water (liquid water and vapor) and air (dissolved in water and in the gas phase) in terms of pressure, and the energy balance in terms of temperature. The equations of water and air mass balance are:

$$\frac{\partial}{\partial t}(\omega_l^w \rho_l S_l \phi + \omega_g^w \rho_g S_g \phi) + \nabla \cdot (\mathbf{j}_l^w + \mathbf{j}_g^w) = f^w \tag{3.1}$$

$$\frac{\partial}{\partial t}(\omega_l^a \rho_l S_l \phi + \omega_g^a \rho_g S_g \phi) + \nabla \cdot (\mathbf{j}_l^a + \mathbf{j}_g^a) = f^a \tag{3.2}$$

where subscripts l and g refer to liquid and gas and superscript w and a refer to water and air. ω is the mass fraction (kg kg $^{-1}$) of a component in a phase, ρ is the density (kg m^{-3}) of a phase, S is the hydraulic saturation (m^3 m^{-3}), ϕ is the porosity (m^3 m^{-3}), $\mathbf{j}$ (kg m^{-2} s^{-1}) is the total flux (advective, diffusive and dispersive) and f is an external source/sink term (kg m^{-3} s^{-1}) (i.e. top boundary condition and mineral hydratation-dehydratation). Note that the firsts two terms in the equations represent the change of mass of water (Eq. 1) or air (Eq. 2) in the liquid and gas phase respectively and the third and fourth terms represent the fluxes of water (Eq. 1) or air (Eq. 2) in liquid and gas phase respectively.

The energy mass balance is written as:

$$\frac{\partial}{\partial t}(E_s\rho_s(1-\phi) + E_l\rho_l S_l\phi + E_g\rho_g S_g\phi) + \nabla\cdot(\mathbf{i}_c + \mathbf{j}_{El} + \mathbf{j}_{Eg}) = f^Q \tag{3.3}$$

where E is the specific internal energy, $\mathbf{i}_c$ is the energy flux (J m^{-2} s^{-1}) owing to conduction through the porous medium, the other fluxes ($\mathbf{j}_{El}$, $\mathbf{j}_{Eg}$) are advective fluxes of energy (J m^{-2} s^{-1}) caused by mass motions and f^Q is an internal/external supply (J m^{-3} s^{-1}) that accounts for boundary conditions at the top (i.e. heat entry from the lamp) and at the laterals (i.e. heat exit through column walls).

A state variable is associated with each mass balance: liquid pressure (P_l), gas pressure (P_g) and temperature (T). Constitutive laws must be used to express the mass balance equations as a function of the state variables. The fluxes and constitutive laws that control these balances are shown in Table 3.1. Further details on mass balance equations and constitutive laws are described by *Olivella et al.* (1994, 1996c). Still, it is worth discussing some of the simplifications implicit in Table 3.1. First, gaseous components diffusion is simulated using Fick's Law. Although it is considered less accurate than the Dusty Gas Model (*Thorstenson and Pollock*, 1989), the difference is small when permeability or pressure is high. According to *Webb and Pruess* (2003) results, differences would be negligible in our case. Second, the effects of vapor diffusion enhancement, tortuosity and constrictivity are embedded in one single factor, τ_0. If vapor diffusion

is not enhanced, τ_0 should be smaller than 1. As we adopt higher values (see section 4), we term it enhancement factor. Finally, liquid fluxes are assumed zero ($k_{rl} = 0$) when water saturation falls below the residual saturation, S^0, which may occur under oven dry conditions, as discussed afterwards.

Table 3.1: Constitutive laws, parameters and values used in the numerical model.

Constitutive laws		Parameters and values
Water saturation for ret. curve in modified van Genuchten model	$S_l = S_i + (1 - S_i)S_e$ $S_e = \left(1 + (P_c/P_0)^{\frac{1}{1-\lambda}}\right)^{-\lambda}$ $S_i = \alpha S^0 \ln(P_c^{dry}/P_c)$	$S^0 = 0.08$, $\alpha = 0.1$ $\lambda = 0.93^*$, $P_0 = 0.0025 MPa^*$ $P_c^{dry} = 650 MPa$
Relative permeability function (for a new ret. curve)	$K_{rl} = 0, \quad S_l \leq S^0$ $K_{rl} = \sqrt{S_{ep}}\left(1 - (1 - S_{ep}^{1/\lambda})^{\lambda}\right)^2, S_l > S^0$ $S_{ep} = (S_l - S^0)/(1 - S^0)$	
Intrinsic permeability for Darcy's Law	$q_\alpha = -\frac{k_i k_{r\alpha}}{\mu_\alpha}(\nabla P_\alpha - \rho_\alpha g)$ $k = k_0\, exp(b(\phi - \phi_0))$	$k_0 = 2.8 \cdot 10^{-11} m^2$ $b = 40$, $\phi_0 = 0.4$
Diffusive flux of vapor (Fick's Law)	$i_\alpha = -(\tau\phi\rho_\alpha S_g D_m \mathbf{I})\nabla w$ $D_m = \tau D\left(\frac{(273.15+T)^n}{P_g}\right)$ $\tau = \tau_0 (S_g)^m$	$D = 5.9 \cdot 10^{-6} m^2 s^{-1} K^{-n} Pa^a$ $n = 2.3$ $\tau_0 = 8$, $m = 3$
Conductive flux of heat (Fourier's Law)	$i_c = -\lambda \nabla T$ $\lambda_{dry} = (1 - \phi)^n \lambda_{solid} + \phi^n \lambda_{gas}$ $\lambda_{sat} = (1 - \phi)^n \lambda_{solid} + \phi^n \lambda_{liq}$ $\lambda = \sqrt{S_l}\lambda_{sat} + \left(1 - \sqrt{S_l}\right)\lambda_{dry}$	$\lambda_{sol} = 2 W m K^{-1}$, $n = 2$ $\lambda_{gas} = 0.024 W m K^{-1b}$ $\lambda_{liq} = 0.6 W m K^{-1b}$
Psychrometric Law	$P_v = 136075\, exp\left(\frac{-5239.7}{273.15+T}\right) a_w$	MPa

Where a_w=molar mass fraction, q_α=flow rate (ms^{-1}), k=intrinsic (k_i) and relative ($k_{r\alpha}$) permeability, μ_α=viscosity (Pa s), ρ_α=density (kgm^{-3}), g=gravity (9.8 ms^2), ϕ=porosity, i_α=vapor diffusive flux (Js^{-1}), S=liquid (S_l) and gas (S_g) saturation, w_α=water mass fraction in gas phase (kg of vapour per m^3 gas phase), D_m=diffusion coeff. ($m^2 s^{-1} K^{n-1}$), T=temperature (°C), τ_0=tortuosity coeff., i_c=heat conductive flux (Js^{-1}), λ=thermal conductivity (WmK^{-1}) and P_v=vapor pressure (Pa). Values used for heat capacities: C_s =875J/kgK and C_w =4185J/kgK.
* Parameters obtained experimentally.
[a] From *Philip and de Vries* (1957). [b] From *Campbell and Norman* (1998)

3.3.2 Oven Dry Conditions

As mentioned above, under oven dry conditions (that is, saturations well below residual saturation), the residual saturation can no longer be considered a lower bound for saturation. To reproduce the experimental data (*Gran et al.*, 2011) a modification of the retention curve and relative permeability functions is necessary. To address this, *Milly and Eagleson* (1982) simply considered the residual saturation to be zero; *Rossi and Nimmo* (1994) proposed a different function to extend the capillary curve towards fully dry conditions; and *Prunty* (2003) used the zero value in standard retention curve models but modified the relative permeability function for the dry range.

The *van Genuchten* (1980) model is widely used under moist conditions but requires modification to represent oven dry. The assumption is that soil can reach full drying, i.e. if evaporation takes place in an oven at $105°C$ or near the surface under a dry or hot atmosphere (*Ross et al.*, 1991).

The van Genuchten retention curve is:

$$S_e = \left(1 + (P_c/P_0)^{\frac{1}{1-\lambda}}\right)^{-\lambda} \tag{3.4}$$

where P_c is capillary pressure, P_0 is related to the capillary pressure required to desaturate the soil and λ is a shape parameter of the function. This equation permits to calculate the effective saturation (S_e) as a function of a minimum saturation S_i and the actual saturation (S_l):

$$S_e = (S_l - S_i)/(1 - S_i) \quad or \quad S_l = S_i + (1 - S_i)S_e \tag{3.5}$$

In order to extend this curve for high suctions (i.e. conditions of drying by evaporation) and to represent the oven dry branch that goes from the residual saturation to the ovendryness, the minimum degree of saturation is expressed as follows:

$$S_i = \alpha S^0 \ln(P_c^{dry}/P_c) \tag{3.6}$$

where there are three parameters: α, S^0 and P_c^{dry}.

The latter can be identified with the capillary pressure for the dry material and can be considered equal to $P_c^{ovendryness}$ =1000MPa. However, lower values may be considered if dryness is induced by atmospheric conditions that are less extreme than oven dryness. S^0 is the residual saturation, for which liquid water becomes discontinuous so that liquid permeability is zero. Parameter α scales the transition from the van Genuchten branch to the oven dry branch of the proposed retention curve. Its value may be chosen as $\alpha = 1/ln(P_c^{dry}/P_c^0)$, where P_c^0 is the capillary pressure for which the oven dry branch crosses S^0 (i.e., $S_i = S^0$). It should not be chosen smaller than P_0 (or else, P_c will remain low for S_l much smaller than S^0) nor very large (or else, the oven dry branch will separate from the van Genuchten branch for S_l much larger than S^0). We adopted here $P_c^0 = 0.03$MPa, for which $\alpha = 0.1$, after some trial and error attempts. The remainig parameters (P_0, λ and S^0 were obtained by fitting independent measurements of suction and saturation). This proposed retention curve is a continuous function with continuous derivatives. A similar form was already proposed by *Fayer and Simmons* (1995).

For the relative permeability function, we assume that the distribution of the liquid phase is unaffected by the above modification and only depends on saturation. Therefore, it is given by

$$\begin{aligned} &k_{rl} = 0, \qquad S_l \leq S^0 \\ &k_{rl} = \sqrt{S_{ep}}\left(1-(1-S_{ep}^{1/\lambda})^{\lambda}\right)^2, \quad S_l > S^0 \\ &S_{ep} = (S_l - S^0)/(1-S^0) \end{aligned} \tag{3.7}$$

where S_{ep} is the effective saturation for permeability. Note that for saturations below S^0 the capillary pressure can be calculated from the retention curve, but the relative permeability is zero. This allows representing water isolated in the meniscus that can not flow as a liquid phase but can still evaporate. Figure 3.2 compares the proposed model and the original van Genuchten model, in terms of retention curve and shows the adopted relative permeability curve. The parameters used here (see Table 3.1) are obtained by manual calibration adjusting a numerical model using the data from an experimental retention curve.

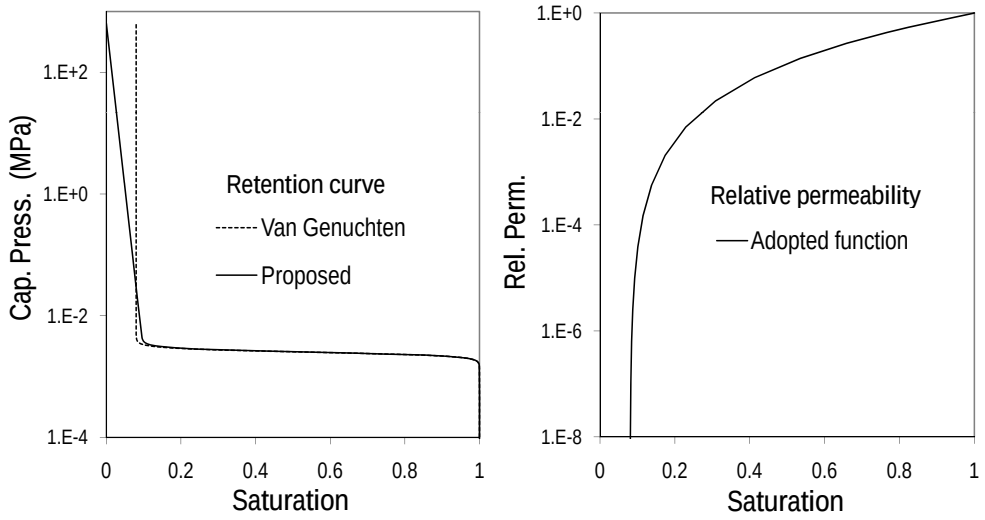

Figure 3.2: Retention and relative permeability curves (original van Genuchten and proposed) for the sand used in the column experiments.

3.3.3 Reactive Transport

The mass balance used for reactive transport can be written as

$$\frac{\partial \phi S_l \rho_l \mathbf{c}_a}{\partial t} = L_l(\mathbf{c}_a) + R \tag{3.8}$$

$$L_l() = -\nabla \cdot (\mathbf{q}_l \rho_l()) + \nabla \cdot (\mathbf{D}_l \phi S_l \rho_l \nabla()) + m_l$$

$$R = r_{eps} + r_{hex} + r_{pent} + r_{stark}$$

$$r_{min} = \sigma_{min} k(\Omega_{min} - 1)$$

where vector $\mathbf{c}_a$ (mol/kg) is the concentration of aqueous species and L_l is the linear operator for the advection, dispersion/diffusion, m_l is the non-chemical source-sink (mol m^{-3} s^{-1}) and $\mathbf{D}_l$ is the dispersion/diffusion tensor ($m^2 s^{-1}$). The values used for the diffusion coefficient and dispersivity are $10^{-9} m^2/s$ (*Lasaga*, 1998) and 0.0015m (between values used by *Aggelopoulos and Tsakiroglou* (2007) and *Zheng et al.* (2008)) respectively. R contains the rates of the kinetic reactions (r_{min}) for all the different mineral phases ($r_{eps}, r_{hex}, r_{pent}$ and r_{stark}), σ_{min} is the mineral reactive surface and Ω_{min} is the ratio between the ion activity product and the equilibrium con-

stant. The reaction rates enable us to calculate the liquid water provided by mineral hydratation-dehydratation. This amount of water is added to the water mass balance as a source/sink term (f^w) in equation 6.1.

$$f^w = (7r_{eps} + 6r_{hex} + 5r_{pent} + 4r_{stark})m_w \tag{3.9}$$

where m_w is the molecular weight of water.

3.4 Numerical Model

The problem is considered one dimensional in a vertical direction. The grid is made up of 240 elements (for 24cm column length). The medium is homogeneous except for the top 1.5cm, where a reduced value of τ_0 (gas diffusion enhancement factor) was used to reproduce the increase in tortuosity caused by precipitated salts in the crust (recall that τ_0 includes the effects of tortuosity, constrictivity and diffusion enhancement). The gas diffusion enhancement factor (τ_0) (see Table 3.1) was calibrated to be 1.2 in the upper zone and 8 below. These values were required to fit the observed evaporation and water content profiles and, at the same time, the observed dilution.
Boundary conditions (BC) for liquid, vapor and heat were chosen to reproduce the laboratory conditions (see Table 3.2). The top boundary is a mixed condition representing gas (air and vapor) and heat inflow-outflows. A radiative heat flux (from the lamp) was added at the top boundary. The lateral and bottom BC were of no-flow for water and solutes, but energy was permitted to dissipate across the insulating layer.

The column was initially saturated in water ($P_g = P_l$ =0.101325MPa). The initial temperature and porosity were $T_0 = 25°C$ and ϕ =0.4, respectively.
Numerical simulations were carried out using the RETRASO-CODE_BRIGHT (RCB) code, which couples the thermohydraulic model CODE_BRIGHT (CB) of *Olivella et al.* (1996c) with the reactive transport model RETRASO of *Saaltink et al.* (2004), which incorporates the approach of *Saaltink et al.* (1998). Furthermore, geochemical calculations are performed with the object-

oriented chemical module CHEPROO (*Bea et al.*, 2009, 2010), which includes high salinity solutions using the equations of *Pitzer* (1973). The feedback of reactive transport in thermohydraulics is performed by a time lag approach. The code solves the thermohydraulic equations (Eq.6.1 to 6.3) for one time step. Results (Darcy fluxes, hydraulic saturation, etc) are used to calculate the reactive transport for the same time step (Eq.3.8). Subsequently, thermohydraulic properties such as porosity changes due to precipitation-dissolution (precipitated mass per unit volume is divided by the solid density of the salts and the volume variation obtained corresponds to the change in porosity) or water activity (computed from the osmotic coefficient (*Felmy and Weare*, 1986)) and the source/sink term (f_l^w) are calculated using the reactive transport results. A new thermohydraulic time step is calculated using these new properties.

Table 3.2: Liquid, vapor and heat boundary conditions and corresponding parameters.

Boundary conditions	Top	Lateral	Bottom
Liquid flux	$j_l = 0$	$j_l = 0$	$j_l = 0$
Vapor flux	$(\omega_g^w)^0 = 0.020 kg/kg$		
$j_g^w = (\omega_g^w)^0 j_g^0 +$	$(P_g)^0 = 0.101325 MPa$		
$+(\omega_g^w)^0 \gamma_g (P_g^0 - P_g) +$	$\gamma_g = 50 kg/s/MPa/m^2$		
$+\beta_g((\rho_g \omega_g^w)^0 - (\rho_g \omega_g^w))$	$\beta_g = 0.03 m/s$		
	$\rho_g = 1.12 kg/m^3$		
Energy flux	$j_e^0 = 750 J/s$	$j_e^0 = 0$	$j_e^0 = 0$
$j_e = j_e^0 + \gamma_e (T^0 - T) + E_g^w (j_g^w)$	$T^0 = 25°C$	$T^0 = 26°C$	$T^0 = 26°C$
	$\gamma_e = 24 J/s/C/m^2$	$\gamma_e = 25 J/s/C/m$	$\gamma_e = 1 J/s/C/m^2$
Salinity flux	$j_s = 0$	$j_s = 0$	$j_s = 0$

Where superscript *0* refers to prescribed boundary values, and subscripts *l*, *g* and *s* to liquid, gas and salinity, respectively. P_g is gas pressure, ρ is density, ω_g^w is the mass fraction of vapor in gas (corresponding to the measured relative humidity above the column), γ_g is leakage coefficient for gas advective flux, β_g is the leakage coeff. for vapor non-advective flux, j_e^0 is a prescribed heat flow from the lamp, γ_e is the energy transfer coefficient for energy flux and E_g^w is the internal energy of water in gas phase per unit mass of water.

3.5 Results and Discussion

Figure 3.3 displays the water saturation, temperature and salinity profiles computed for four different times along with the experimental results at the end of the experiment, after 12 days. Saturation profiles illustrate the progressive desaturation of the columns from the top. The water content drops over time to values near residual saturation at a depth that increases with time. Saturation at the top reaches oven dry conditions (water saturations close to zero). The bottom of this zone represents the location of the evaporation front. Below the front, water content continues to increase downwards, leading to a degree of saturation profile similar to that of the sand retention curve. The good match between model and experiment at the upper oven dry area (above 4cm depth) supports the validity of the retention curve modification (note that without this modification reproducing the step in the saturation profile would not have been possible), which improves the simulation of multiphase flow under very dry conditions.

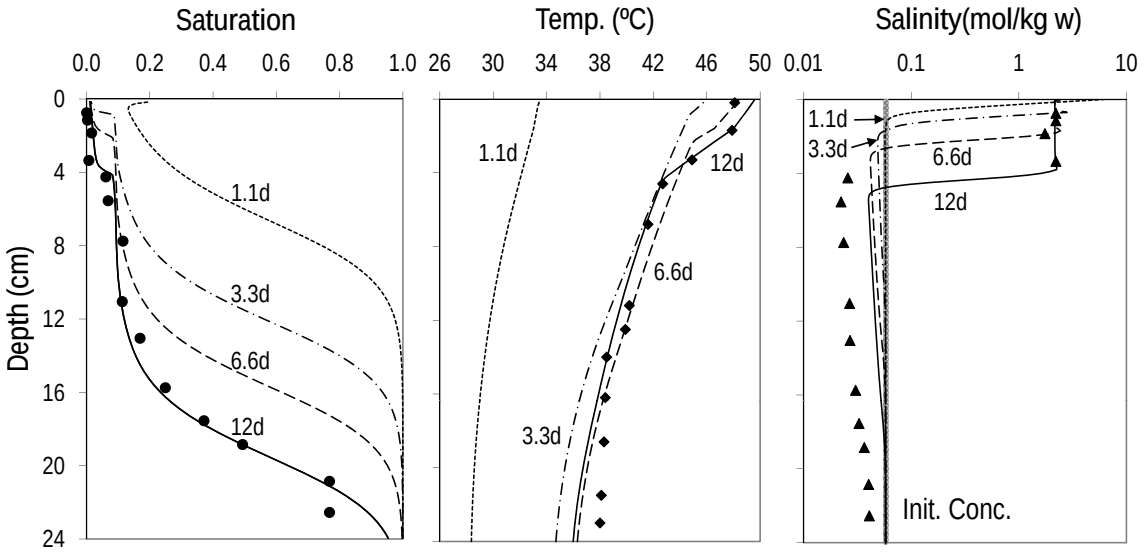

Figure 3.3: Profiles of saturation, temperature and salinity measured at the end of the experiment (symbols) and computed (lines). The time evolution is shown for four different times (after 1.1 days, 3.3 days, 6.6 days and, at the end of the experiment, 12 days). Note that salinity is expressed as concentration in water to facilitate the analysis of mass transport processes.

Temperature rises during the experiment and displays a slope change at the evaporation front. The temperature gradient is larger above than below the front because the evaporation front acts as a heat sink. Another smaller temperature slope change can be detected at a depth of 1.5cmfor the temperature profiles at days 6.6 and 12. This is due to the increase in thermal conductivity caused by salt precipitate at the crust (note that conductivity depends on porosity, see Table 3.1).

The spatial distribution of concentration (expressed as salt mass per unit mass of water to facilitate the analysis of mass transfer processes) is noteworthy. Salinity is extremely high at the surface, where the water content is negligible, reaching salt solubility and producing precipitates. This high concentration zone grows with time, advancing in depth with the evaporation front. Immediately below, salinity drops sharply to values underneath the initial concentration. The minimum concentration is always located immediately below the evaporation front. Further down, salinity rises slightly with depth, but is still more diluted than the initial conditions. A difference between the experimental data and the numerical model is observed: the minimum in the simulated concentration is smaller than the measured one. The water content and temperature profiles do coincide with what might be expected (drier and warmer conditions at the surface than at depth) unlike the concentration profile. Most traditional models (e.g. *Huinink et al.* (2002)) predict a maximum concentration at the evaporation front and a smooth monotonic reduction downwards toward initial concentration, caused by downwards diffusion. The radically different behaviour observed in our concentration profiles can be attributed to vapor fluxes. Actually, the time evolution of cumulative evaporation (Figure 2 of *Gran et al.* (2011)) evolves according to the traditional model (e.g. *Sghaier et al.* (2007)), but the evolution of salt concentration profile does not.

The fact that the model reproduces qualitatively the observations suggests that it can be used to determine the role of water flow, heat and transport processes in the system. We discuss below the mechanism responsible for the dilution of the solution.

Figure 3.4 displays the profiles of water and heat fluxes for the same instants as in Figure 3.3.

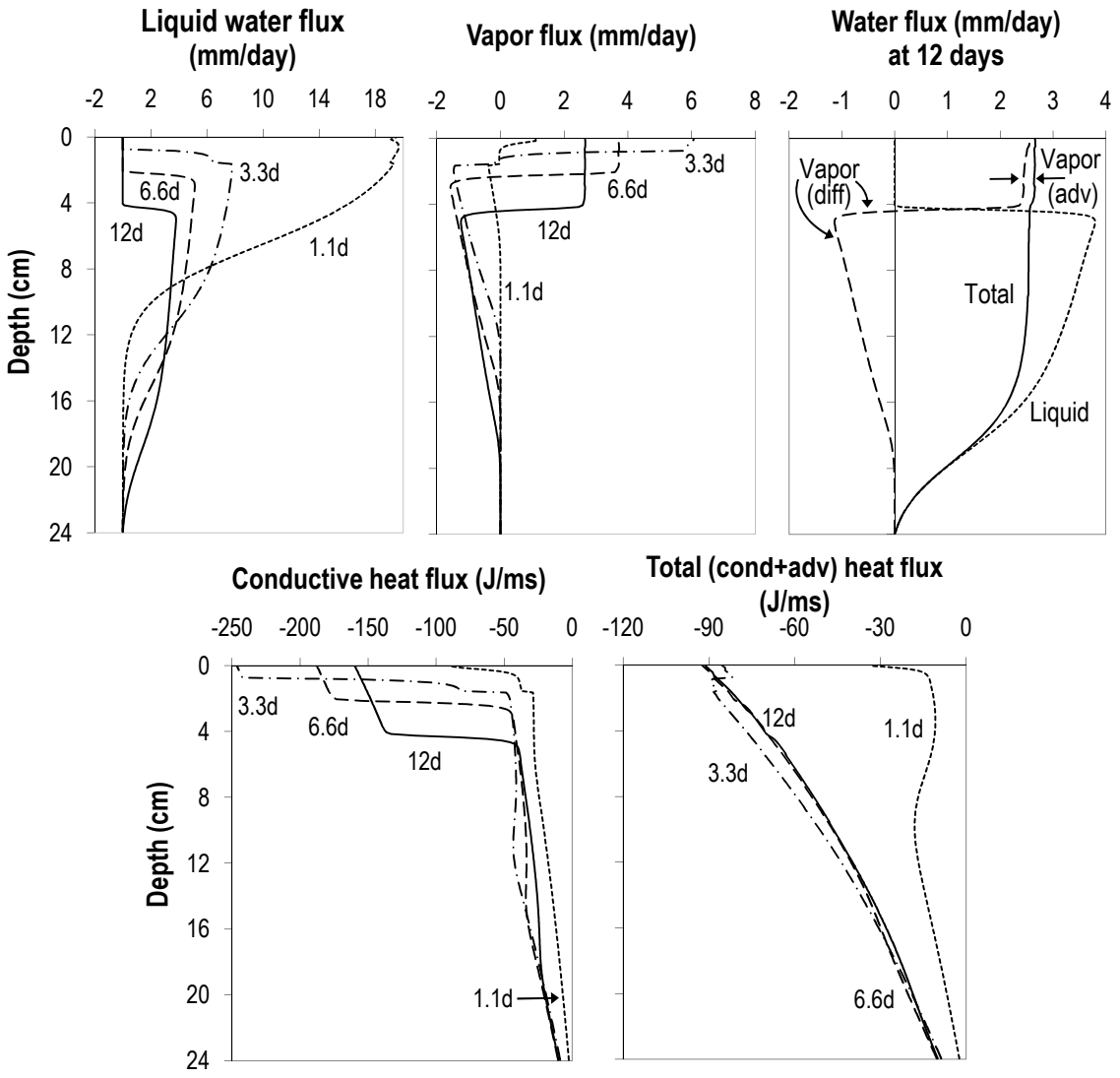

Figure 3.4: Computed profiles of liquid, vapor and total water fluxes (above), and conductive and total (conductive plus advective) heat fluxes (below). Positive and negative values stand for upward and downward flows, respectively. The simulation results are shown for four different times (after 1.1 days, 3.3 days, 6.6 days and 12 days). The difference between the diffusive vapor flux and the total water flux, displayed in the top 4cm of the above graph on the right, is equal to the advective vapor flux.

Liquid water flows upwards because of capillarity throughout the experiment. An evaporation front, located where the liquid flux drops abruptly to zero, may be observed after 3.3 days. Water vapor flux profiles show that vapor flows both upwards and downwards from the evaporation front. This front advances deeper into the soil as the feeding liquid flux from the bottom diminishes over

time. Above this front, water can no longer flow as a liquid. Nevertheless the water content continues to diminish towards the top of the column in response to some residual evaporation above the front. Note that the water content must be very low (very high suction) and/or the salinity very high (high osmotic effect) to ensure an upwards vapor flux despite the upwards increase in temperature. Both factors, high suction and salinity, contribute in this case to the upwards vapor flux above the evaporation front. None of these two factors contribute significantly below the evaporation front, so that vapor diffuses downwards according to the temperature gradient. Condensation of this downward vapor flux accounts for the decrease of the vapor flux at the bottom of the column and for the dilution of the solution below the evaporation front. Both upward and downward vapor fluxes are present throughout the experiment.

The numerical model also enables us to study in detail heat fluxes. Figure 3.4 displays a conductive heat flux downwards throughout the column. This flux is larger in the upper zone, where the soil is dry, and decreases over time. Note the sudden fall in heat flux observed at all time steps at the evaporation front, which is due to the heat sink produced by evaporation. The advance of the evaporation front is observed very clearly and its location is controlled by the above heat flux, which decreases with depth and dryness. The total heat flux graph exposes that conductive and advective (latent) heat fluxes are similar in magnitude but in opposite directions above the front. Below, both fluxes are directed downwards although the advective flux is the dominant one.

Figure 3.5 displays the spatial distribution of the evaporation and condensation rates and the vapor mass fraction profile. The vapor mass fraction profile presents a marked change in the slope and provides evidence of two distinct gradients. Since evaporation occurs at this juncture, the increase in vapor and gas pressure generates vapor diffusion and advection both upwards and downwards.

The graph on the right displays the evolution of the evaporation (negative values) and conden-

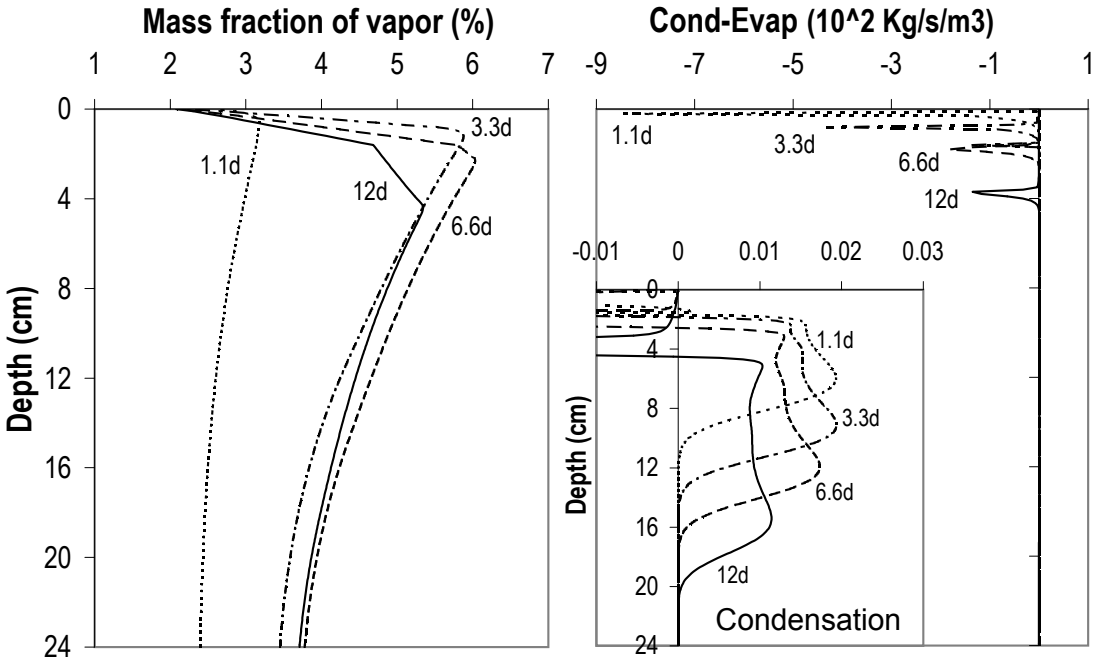

Figure 3.5: Computed profiles of vapor mass fraction and evaporation (negative)/condensation (positive) rates for four different times. Note the change in the vapor mass fraction slope at 1.5cm depth owing to the imposition of the reduction in vapor diffusivity on the salt crust.

sation (positive values). The evaporation rate is higher at the start and decreases as the evaporation front advances deeper into the soil. Note that condensation always occurs below the evaporation front and that its magnitude is substantially lower than that of the evaporation, causing the soil to dry. Condensation extends throughout the relatively dry portion of the column, from residual saturation to saturations around 0.6 (compare the inset of Figure 3.5 and the saturation profiles in Figure 3.3). Vapor condensation occurs from the early stages and its maximum evolves decreasing as it advances into the soil because vapor diffusion is hindered by liquid water (recall Table 3.1, that gas diffusivity is multiplied by S_g^3). This explains the decrease in concentration below its initial value. The fact that the model underestimates the reduction in concentration can be attributed to an excessive reduction of diffusivity or to further gas diffusion enhancement.

3.6 Sensitivity Analysis

Further insight into the above processes and into the role of controlling parameters can be gained from a sensitivity analysis. Processes are strongly coupled, i.e. all the parameters affect all the processes. We focused on the sensitivity of the boundary heat dissipation (γ) and the gas diffusion enhancement factor (τ_0), which proved to be more illustrative. Table 5.3 presents the values adopted for these parameters.

Table 3.3: Studied parameters for the sensitivity analysis: boundary heat dissipation (at the walls and at the bottom) and gas diffusion enhancement factor (τ_0). Compared to the base model (BM): the boundary heat dissipation, by means of γ value, has been doubled and increased by an order of magnitude alternatively and τ_0 value for the upper material (firsts 1.5cm) has been increased from 1.2 to 8 to equal the value for all the column.

	Model					
Parameter	BM	$2\gamma_{bot.}$	$10\gamma_{bot.}$	$2\gamma_{wall}$	$10\gamma_{wall}$	τ_0
γ_{wall}	**1**	1	1	**2**	**10**	1
γ_{bottom}	**25**	**50**	**250**	25	25	25
τ_0	**1.2**	1.2	1.2	1.2	1.2	**8**

Figure 3.6 illustrates the effect of increasing heat dissipation across the walls. The effect of the heat dissipation through the bottom has also been studied but is not shown here (it presents a similar system response but less relevant). Increasing γ at the walls causes an increase in the rate of sensible heat dissipation, thus having less energy available for evaporation. Although Figure 6 shows higher evaporation at the evaporation front, this is overcompensated by a higher condensation below the front. As a result the overall saturation increases and the evaporation front remains closer to the surface. It also leads to a lower overall temperature. Note that as more heat is dissipated the temperature gradient just beneath the evaporation front also increases. This causes an increase in the downwards vapor pressure gradient and in the downward vapor flux, whereas, the upward vapor flux diminishes. The shape of the condensation profile varies to give a bigger maximum concentrated just below the evaporation front. We can infer that the amount of heat

dissipated through the walls controls the thermal gradient in the column.

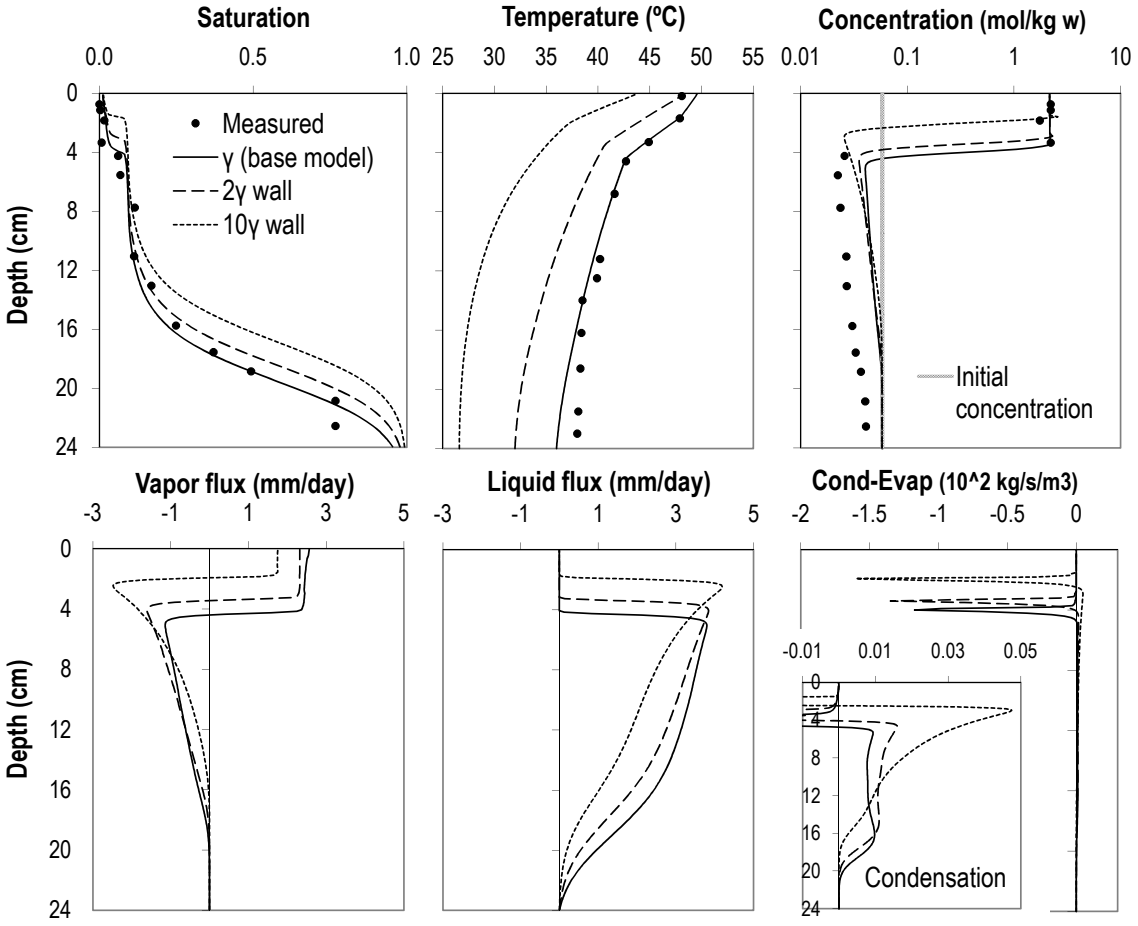

Figure 3.6: Analysis of the effect of boundary heat dissipation. Computed profiles of saturation, temperature, concentration, water mass flux, evaporation and condensation after 12 days.

The gas diffusion enhancement factor (τ_0) was homogenized increasing its value in the upper part of the column (Table 5.3). As a result, the soil dries faster and the overall degree of saturation diminishes. The evaporation front advances deeper into the soil and the area below is colder. The temperature profile changes from three to two different gradients: the temperature gradient near the surface increases and becomes uniform towards the evaporation front. As the lower temperature leads to less lateral heat dissipation, the temperature gradient below the evaporation front decreases. Accordingly, the downward vapor flux diminishes and hence, the condensation.

By contrast, the upward vapor flux increases, showing that vapor can flow more easily towards the surface and explaining the downward displacement of the evaporation front and the column drying. As the evaporation front advances deeper into the soil, condensation takes place further down. Overall, the results applying a different value of τ_0 in the upper part of the column, fit to experimental data suggesting that variations in τ_0 must be included to improve our model.

3.7 Conclusions

The model reproduces quite accurately experimental observations of varied nature (temperature, water content and salt concentration). Most model parameters were either measured (retention curve) or derived from the literature (constitutive laws in Table 3.1). The only parameter that had to be varied significantly to obtain a good match was the vapor diffusion enhancement factor. Reliability of model parameters and the good qualitative fit between observations and model outputs lends support to the validity of the model, which prompted us to analyze and quantify the computed processes. These confirm the initial conjecture about the highly coupled and rather complex nature of evaporation from a salinizing soil. In essence, evaporation is driven by heat, but it can be limited by liquid and vapor flux processes and by salinity. Some conclusions can be inferred from the calibrated model:

- Evaporation causes vapor pressure to increase at the evaporation front causing vapor to flow upwards and downwards. Both fluxes occur throughout the experiment, but the relative importance of the downwards flux increases over time. In our model the downward flux is half that of the upward flux at the end of the experiment.

- The evaporation front is very narrow, which contradicts the analysis of *Konucku et al.* (2004). Most evaporation is concentrated in less than 1cm. Some evaporation occurs above the front, but condensation starts immediately below. This finding may be due to the experimental conditions (loss of heat through the column walls). Without this heat loss, water

vapor could have penetrated further into the soil, which is consistent with the findings of *Scanlon and Milly* (1994).

- Condensation of the downward vapor flux dilutes the solution beneath the evaporation front with the result that salinity drops below the initial value. This finding confirms the existence of a water separation process driven by evaporation, which contradicts the current models of soil salinization and formation of eflorescences. However, reproducing the concentration profiles required a large gas diffusion enhancement factor.

- Heat flows downwards from the surface to the bottom of the column mainly by conduction. Still, advection of latent heat is also relevant. Upwards advection almost compensates downwards conduction above the evaporation front, so that the total heat flux is not very sensitive to the location of the front. Immediately below the front, advection is comparable to conduction, but it diminishes further down as vapor condensate. In short, vapor diffusion leads to a highly relevant energy transport mechanism within the soil.

In summary, our model supports the traditional division of the soil into a virtually dry (and/or saline, as we have seen) region and a moist region, separated by an evaporation front. Vapor diffusion is the only relevant water flow mechanism in the upper region. This view may suffice for evaluating evaporation rates and water mass balances. However, assessing salt processes requires acknowledging that not only liquid water but also vapor diffusion occur below the evaporation front.

Further conclusions can be drawn from the sensitivity analysis:

- Vapor diffusion is very sensitive to the heat boundary conditions. The amount of heat dissipated throughout the column walls controls the temperature gradient. Downward diffusion is enhanced by the lateral heat dissipation through the walls.

- It is the temperature gradient more than the temperature range, what governs the magnitude of vapor fluxes. Therefore, these processes can occur in salinized soils under temperatures lower than the ones observed here.

- The formation of a crust due to salt precipitation reduces porosity and increases tortuosity, which hinders evaporation. These have been simulated by increasing tortuosity at the crust (actually, reducing τ_0 from 8 in the column to 1.2 in the crust). This was necessary to reproduce evaporation rates together with observed temperatures and salinity profiles.

Finally, further research is warranted to resolve a number of issues. The dilution simulated by the numerical model is always lower than that measured in the experiments. The representation of vapor flux may not be accurate, diffusion enhancement factors are very large, which demands deeper analysis of this issue.

Chapter 4

Monitoring and analysis of the hydraulic behaviour of a multilayer pilot cover

4.1 Introduction

Cover systems are one of the main design alternatives for isolating solid waste. Soil covers are widely used at municipal and industrial landfills and at hazardous and radioactive waste disposal facilities worldwide (*Peng and Jiang*, 2009). Percolation reduces leakage, thus reducing risk to human health and environment contamination. Therefore, the main purpose of the cover system is to protect the underlying waste from infiltration by promoting surface runoff and lateral drainage, hindering access of roots or animals and controlling moisture and percolation. A frequent parallel requirement is to minimize gas diffusion, so as to avoid bad odors (organic waste) or release of radioactive gases (radioactive waste). Low infiltration barriers commonly meet this requirement as a side effect. Cover systems are planned to be in place and preserve their functions for long

periods. Therefore, they are usually designed with natural materials.

Surface soil covers are designed in various forms, ranging from simple soil covers to multilayered systems, and relying on different mechanisms, from water-balance covers to hydraulic barrier covers. Cover systems have conventionally been designed based on resistive barriers in which infiltration is reduced by placing a layer with low saturated hydraulic conductivity. (e.g. geomembranes, geosynthetic clay, compacted clay layers). Although hydraulic barriers minimize water movement, they have been proved to leak due to biointrusion, differential subsidence and/or desiccation cracks even in a humid climate (*Jessberger and Stone*, 1991; *Smith et al.*, 1997; *Dwyer*, 1998; *Albrecht and Benson*, 2001; *Albright and Benson*, 2003; *Albright et al.*, 2006).

Alternative designs, known as water balance or evapotranspirative (ET) covers, have been proposed to reduce percolation. ET covers rely on water storage principles, retaining infiltration during periods when precipitation exceeds evapotranspiration and removing it during drier seasons. Infiltration is limited by providing sufficient capacity to store the water until it is either transpired through vegetation or evaporated from the soil. ET covers are effective barriers to percolation in most arid and semiarid environments (*Nyhan et al.*, 1990; *Gee et al.*, 1993; *Ward and Gee*, 1997; *Morris and Stormont*, 1997; *Dwyer*, 1997). However, they are highly dependent on vegetation, which makes them less robust (*Scanlon et al.*, 2005), and on their thickness, which impedes covers design to be extrapolated from site to site (*Gee et al.*, 2006). Therefore, ET covers are often ineffective both in dry and in more humid climates (*Albright et al.*, 2004).

A combination with a capillary break,increasing the water storage capacity of the cover (*Scanlon et al.*, 2005), is the next step to improve the ET covers performance. A capillary barrier consists of a fine-grained soil overlying a coarse-grained soil (often a sand layer overlying a gravel layer). The contrast in their unsaturated hydraulic properties minimize vertical percolation promoting storage in the overlying layer while maintaining the lower one dry. This mechanism works while water content in the upper layer does not reach the point where its matric suction equals the water entry pressure value of the coarse soil below. At that moment, a breakthrough occurs and

water enters into the coarse layer which acts as a drain diverting the infiltrated water laterally. The steeper the slope, the higher the lateral flow along the interface and the more effective the capillary barrier (*Ho and Webb*, 1998). Once the moisture content in the upper layer decreases again, its matric suction rises and the hydraulic barrier becomes reactivated.

Capillary barriers (CB) have proven effective in restricting percolation in arid and semiarid environments (*Ward and Gee*, 1997; *Dwyer*, 1998; *Khire et al.*, 1999; *Scanlon et al.*, 2005) but may fail in wet climates, if percolation from the upper layers is high. The capillary barrier effect may be lost easily during intense and/or continued periods of precipitation (*Khire et al.*, 1999; *Albright and Benson*, 2003; *Abdolahzadeh et al.*, 2011). To prevent this deficiency the topsoil above the CB should be as water retentive as possible and thick, but not too much, to hinder deep-rooted vegetation (*Khire et al.*, 2000). As other designs, CB can also suffer from damage caused by biointrusion (*Khire et al.*, 1994; *Dwyer*, 2003; *Gee et al.*, 2006).

The purpose of this study is to find the soil layer combination able to control infiltration, while preventing intrusion of burrowing animals and root penetration, in a semiarid climate where precipitation is highest in winter (low evaporation periods). To this goal, two pilot field-scale covers were built by combining water-balance and hydraulic barrier designs with a biointrusion and a capillary barrier. The covers were extensively instrumented to enable assessing the performance of the different barriers of each cover and comparing the two designs.

4.2 Pilot Cover Design

The pilot covers were installed at the Spanish facility for disposal of low and intermediate level radioactive waste located at El Cabril (Córdoba, southern Spain). The regional climate is semiarid with mean annual precipitation of 613mm (from 2004 to 2013). Most of the rain falls during the winter and the rest is distributed mainly among autumn and spring, when evapotranspiration rates are low. To overcome the excess of infiltration versus evapotranspiration a cover comprising

topsoil water-balance layers overlying a capillary barrier protected by a biointrusion barrier was designed. Two covers, Test I and Test II, were set up to test different layer combinations. The surface of each cover is approximately $245m^2$ ($22m$ long by $11m$ wide). The geometry of the covers is imposed by the need of covering the concrete cells that contain the radioactive waste together with geographic restrictions. The result are two contrasting slopes: 2% at the upper zone (from now on, platform zone) and 40% at the lower zone (slope zone). Figure 4.1 shows the future final cover laying on the top of the disposal cells and, highlighted in gray color, the portion that inspires the pilot cover (simplified due to symmetry).

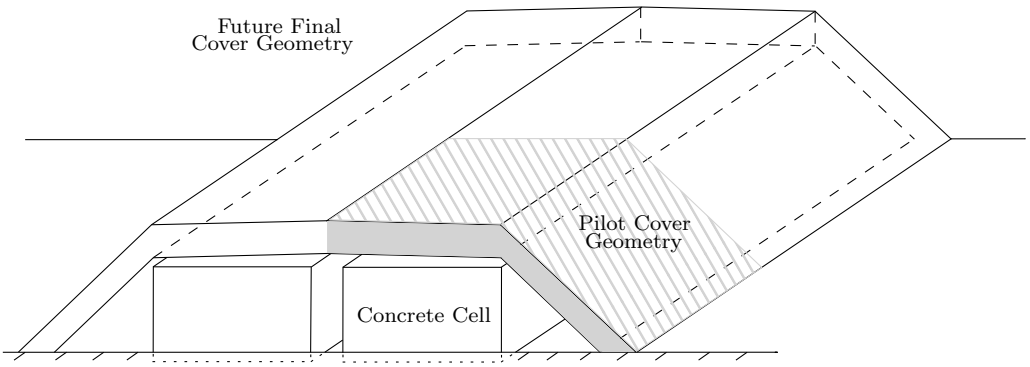

Figure 4.1: Geometry of the future final cover laying above the surface concrete disposal cells. Due to symmetry, the geometry of the pilot cover is simplified to the area shown in gray.

Layering of the two test covers is displayed in Figure 4.2. The total thickness of the pilot cover is 3.15m for Test I and 2.95m for Test II. Every layer or set of layers has a specific purpose. From the surface to the bottom, the layers and their roles are:

- Topsoil with 30% gravel: to reduce erosion from wind and run-off and to store water to facilitate the growth of vegetation promoting evapotranspiration and increasing slope stability. Gravel-soil mixtures with 33% gravel are effective in reducing erosion without affecting vegetation growth or evaporation (*Waugh et al.*, 1994). The gravel diameter is 50-150mm.

- Soil: to retain enough water to allow the establishment of vegetation, promoting evapotranspiration, and enhancing the growth of short-root plants.

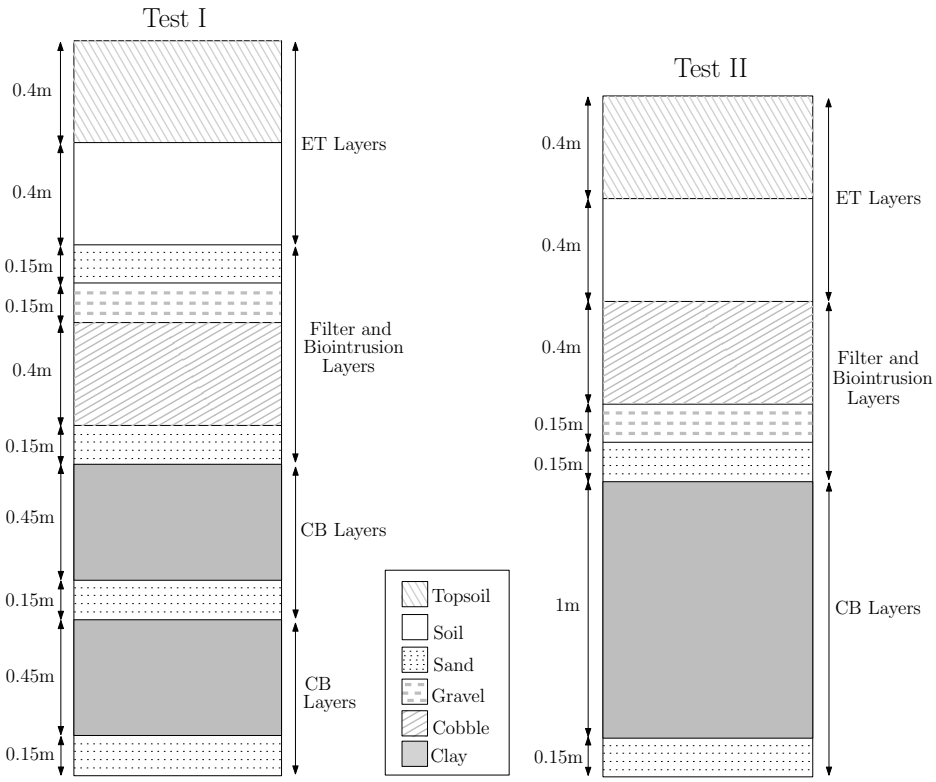

Figure 4.2: Test I and Test II profiles. Both covers present the same two first layers, but then the rest diverge in size and order. Both designs include a capillary barrier consisting of a clay layer above a sand one, but in Test I it is divided into two independent units to study the width and addition effect.

- Sand (only present in Test I): to act like a filter preventing fine soil to mix and contaminate the underlying coarse materials. Sand diameter is 0.5-1mm.

- Gravel and Cobble: to form a biointrusion barrier. A 0.3m of river cobble embedded between 0.1m layers of gravel prevent intrusion by burrowing animals and restrict root growth (*Anderson and Forman* (2002)) and creates an obstacle to ants (*Gaglio et al.* (2001)). In Test I, the gravel layer below the cobble is been replaced by a sand layer. In Test II, the gravel above the cobble is been removed. Animal access is avoided by combining different grain sizes and using materials with rounded corners. The largest grain sizes cannot be supported by small species and at the same time, their rounded corners show poor stability, collapsing when larger species excavate. Ants and small mammals can not dig out preferential

paths. The cobble layer, as a non-retentive material, prevents water storage and root growth through it (as roots prefer to grow laterally in the upper layers with a potential higher water content). Gravel and cobble diameter are 5-20mm and 100-200mm, respectively.

- Sand: to provide a lateral drain for water that infiltrates through the soil and biointrusion layers. Diameter: 0.5-1mm.

- Clay (0.45m width in Test I and 1m in Test II): to act as a low permeability infiltration barrier and as a capillary barrier (together with the underlying sand layer). Moreover, due to its high water retention capacity, the clay is saturated which prevents gas diffusion. The effect of the clay layer width is also tested comparing the use of two layers of 0.5m width (Test I) with one layer of 1m clay (test II).

- Sand: to be a part of the capillary barrier (being the coarse material below the clay). In case of water breakthrough, being highly permeable, it also prevents water storage by draining the infiltrated water and boosting the reactivation of the barrier. Its diameter is 1-3mm.

The topsoil and the soil layers conform the water-balance section which keeps the percolation rates towards the capillary barrier low. Moreover, the soil overlaying the coarser layer (sand in Test I and cobble in Test II) creates a first capillary break. Note, that in Test II the cobble layer is directly below the soil layer (the upper sand is not present and the gravel layer is moved below the cobble). The goal of this variation is to compare their ability as a biointrusion barrier and also to design a cover with a smaller number of layers (the upper part of Test II presents one layer less than Test I).

A HDPE (high density polyethylene) geomembrane underlays both covers to diverge water to a collection system. The geomembrane is 1.5mm thick and is located between two anti-punching sheets of geotextile. Perimeter drains were installed around the cover surface to prevent the entrance of external water into the system and to collect run-off. To prevent material mixing during the cover construction permeable geotextile was placed between all soil layers.

4.3 Monitoring System Design

The monitoring system is critical to evaluate the performance of the covers (*Scanlon et al.*, 2005; *Peng and Jiang*, 2009). A process monitoring approach is followed to analyze the effectiveness of the different layer combinations. That is, many parameters related to flow processes are measured for each layer. This is considered more robust than relaying on a single parameter (*Scanlon et al.*, 2005).

The cover geometry promotes very different flow conditions along its longitudinal section: at the platform zone water flow is assumed to be predominantly vertical due its low slope whereas at the slope zone the covers receive both vertical infiltration and upstream drainage. In fact, the total lateral flux increases linearly with distance from the top if vertical infiltration is constant. Therefore, in order to maintain a similar water content along the cover, the slope should increase linearly with distance from the top. This prompted *Selker* (1997) to propose a parabolic cross section. A two slope system was used instead, to facilitate construction. Still, monitoring must acknowledge the different types of behavior. Accordingly, we define four monitoring sections, 1 through 4, starting from the top (see Fig. 4.3).

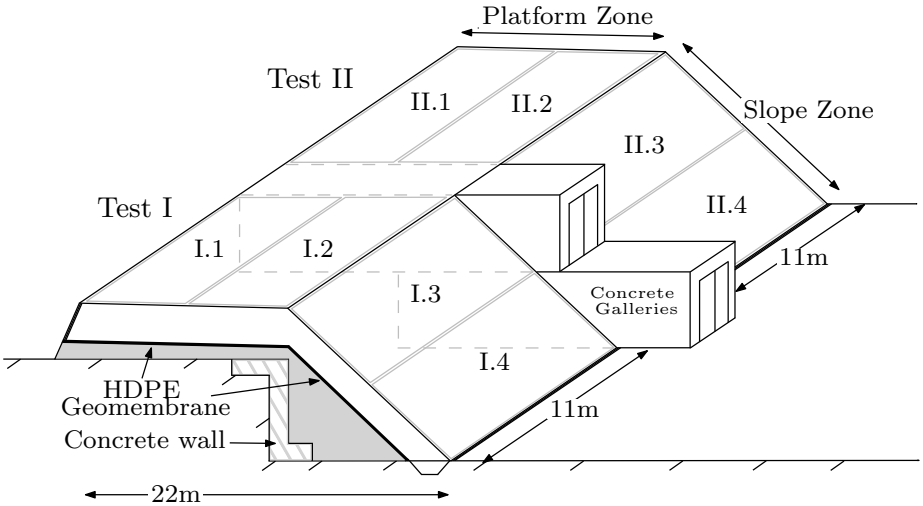

Figure 4.3: Outline of the two adjacent tests and the concrete gallery that separates them. The cover sits on top of a concrete wall which emulates the upper corner of the disposal cells shown in Fig. 4.1. An HDPE geomembrane underlays the cover to collect infiltrated water. Each test is divided in four sections and at the center of each one a complete monitoring system is installed.

Because of the spatial flow variability together with the differences due to soil properties and sensors limitations (restricted measure range), the use of different sensors to record the same variable is required in many layers. Hence a large monitoring system is necessary, which results in a complex scheme of sensors.

Tensiometers are installed to monitor suction,in the materials where very low suctions are expected (i.e. soil and clay layers); psychrometers and matric water potential sensors in layers with medium values, and hygrometers in the materials with potentially highest suctions. If the suction range expected in one layer is wider than the sensor capability, more than one type of sensor is installed (i.e. hygrometer and matric potential sensors in the topsoil layer).

To measure temperature, thermocouples are installed in addition to the suction sensors that also record temperature (hygrometers and psychrometers). Soil thermal properties and heat fluxes are also monitored at the upper layer. Volumetric water content is measured by time domain reflectometry (TDR) sensors in several layers to determine changes in moisture storage. Sensors used to study water and energy fluxes are specified in Figure 4.4. Variables and measurement ranges are also displayed.

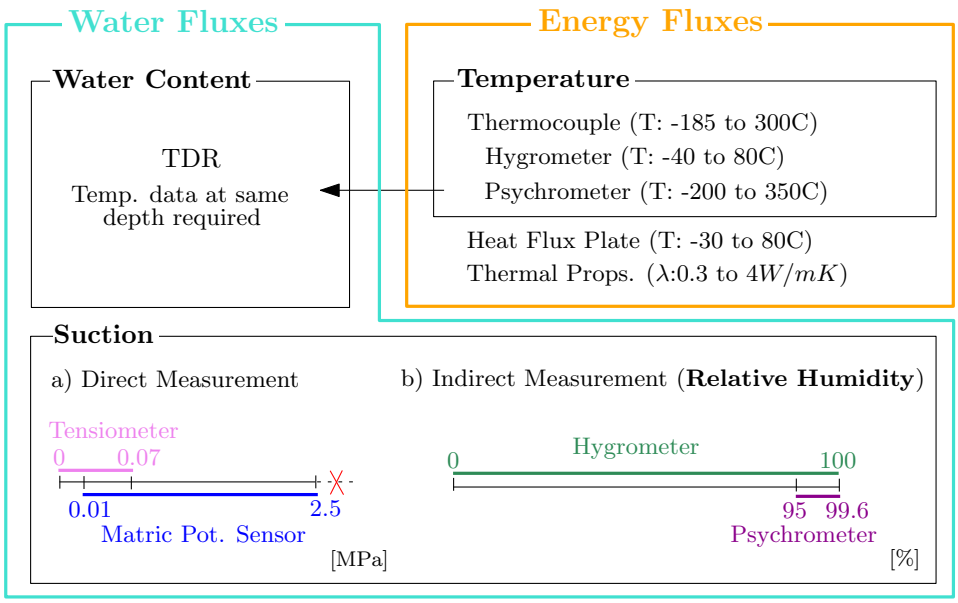

Figure 4.4: Sensors to study water fluxes (blue box) and sensors to energy fluxes study (orange box), measured variables and range of measurement are shown. Water content is measured by TDR sensors and suction by tensiometers and matric potential sensors. Hygrometers and psychrometers are used to cover high suctions range by recording the relative humidity (from which suction is obtained). Soil temperature is registered by thermocouples, hygrometers and psychrometers.

Note that due to the lack of sensors able to measure high suction values, sensors that measure relative humidity are used to cover a wider suction range. By means of the Psychrometric Law (*Edlefsen and Anderson* (1943)) we obtain suction data from the relative humidity value:

$$RH = exp\left(\frac{\psi M_w}{\rho_l RT}\right) \tag{4.1}$$

Table 4.1 presents the precise sensors, brand, producer, variable measured and the number of each type that have been installed in the pilot covers.

The aim of the monitoring system is to record the maximum possible amount of information while avoiding interferences between the sensors (as there are many of them in a reduced space). Depending on the kind of signal emitted by the sensor and the method used to make the measurement, some installing rules and minimum distances between sensors are proposed:

Table 4.1: Variable measured, type of sensor, model, producer and number of units installed.

Group	Sensor Type	Measured Variable	Producer	Number
Heat flux	T Thermocouple	Temperature	TC s.a.	33
	Heat Flux Plate HFP01SC	Heat Flux	Hukseflux	12
	Thermal Props. TP01	λ, C_v, α	Hukseflux	10
Capillary Pressure	Hygrometer HMT333	Suction	Vaisala	45
	Tensiometer STCP-850	Suction	SDEC	18
	Psychrometer PST-55-150-SF	Rel. Humidty	Wescor Inc.	45
	Water Matric Pot. Campbell 229	Rel. Humidty	Campbell Sci.	20
Water Content	TDR STCP-850	Vol. Water Content	SDEC	45

λ is thermal conductivity, α thermal diffusivity and C_v volumetric heat capacity.

- The minimum distance between TDR sensors is 8-10cm in horizontal direction and 15cm in vertical direction.
- Tensiometers need 15cm of distance to any other sensor.
- Psychrometers need 3cm of distance to any other sensor.
- Matric potential sensors need 6cm of distance to any other sensor (this could be less in very dry soils).
- Psychrometers, hygrometers and matric potential sensors should be installed at the same depth to be able to cross data.

Furthermore it is important to remember that, due to correction requirements, TDR sensors need always a temperature reading at the same depth.

The final distributions of sensors for Test I and Test II are given in Figure 4.5. Note that sections 1, 2 and 3 are fully instrumented sections for both tests while sections 4 have a reduced system (these sections are supposed to be more likely influenced by boundaries).

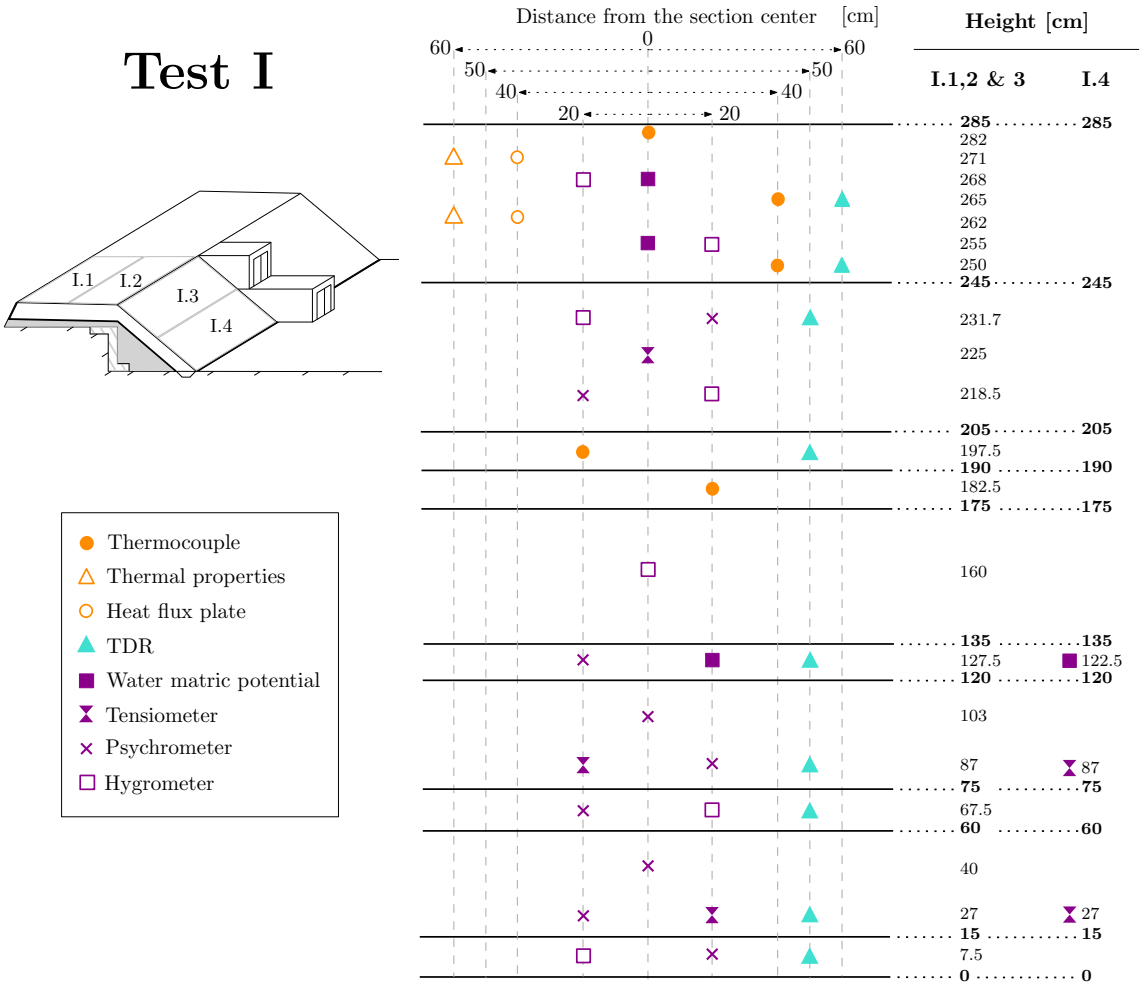

Figure 4.5: Spatial distribution of sensors in Test I. For each section, the heights of the sensors and the layer changes are displayed on the right. The longitudinal distance from the section center is shown on the top. In orange, sensors that measure temperature, energy flux and thermal properties. In blue, water content, and in purple, suction and relative humidity sensors. Note that section 4 is much less instrumented (only the three sensors indicated besides their heights) because it is expected to be more likely affected by boundary effects.

Temperature and soil water content gradients are expected to be greater in the upper layers. Hence the number of sensors is larger close to the surface. Sensors were installed along the cen-

terline of each test section during the cover construction. All the wiring lays horizontally, parallel to the base and ceiling of the layers, avoiding connections among different layers. Wires run from sensors to data loggers inside the concrete galleries for automated data collection. Galleries not only separate the two tests, but also provide room for the data loggers and monitoring systems. Data from a weather station at the site is also collected: temperature, wind speed, wind direction, relative humidity, solar radiation and precipitation are recorded hourly.

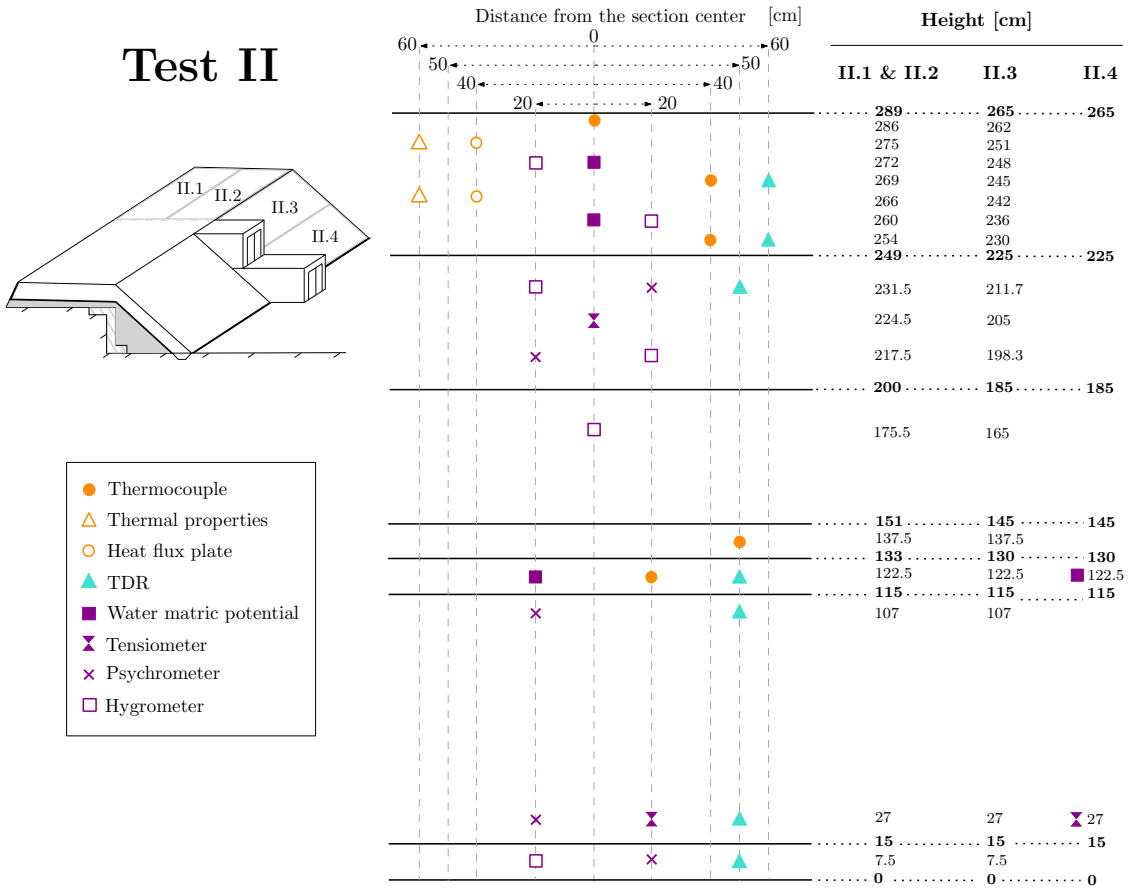

Figure 4.6: Spatial distribution of sensors in Test II. For each section, the heights of the sensors and the layer changes are displayed on the right. The longitudinal distance from the section center is shown on the top. In orange, sensors that measure temperature, energy flux and thermal properties. In blue, water content, and in purple, suction and relative humidity sensors. Note that section 4 is much less instrumented (only the two sensors indicated besides their heights) because it is expected to be more likely affected by boundary effects.

4.4 Results and Discussion

Two year period (from the start of 2009 until April 2011) of temperature, water volume content and suction data is analyzed. The total annual precipitation for 2009 was 629mm and for 2010, 1271mm. Therefore, 2009 is an average year, while 2010 is a year with double the average precipitation. This humid year allows to study the cover performance under very wet conditions.

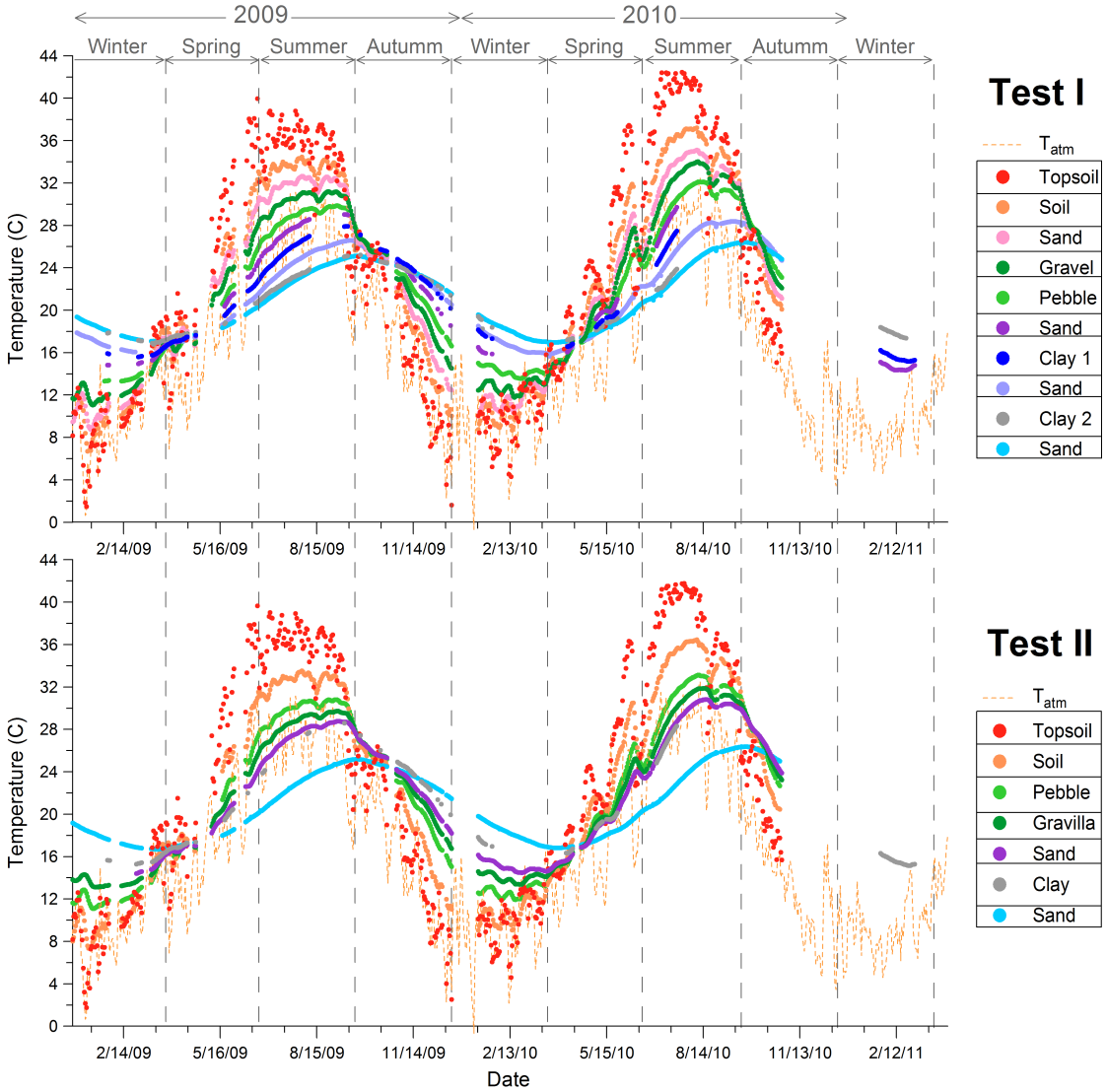

Figure 4.7: Time evolution of the daily mean temperature at several depths during 2009 and 2010 for Test I (upper plot) and Test II (lower plot). The atmospheric temperature registered by the meteorological station is represented by the orange dashed line.

Figure 4.7 displays the time evolution of the daily mean temperature at several depths during 2009 and 2010 for both Test I and Test II. The figure illustrates the typical seasonal fluctuations with decreasing amplitude and delayed peaks with depth. The highest temperatures occur in the topsoil layer (red dots) and decrease downwards into the soil during the summer. The opposite occurs in winter. During the summers, soil temperatures in the first four layers are much higher than air temperature (dotted gray line). During the dry season temperatures rise because reduced evaporation implies the need to increase sensible heat, long wave radiation and conduction into the soil in order to balance the incoming radiation. In fact, a drop in temperature can be observed after each rainfall event.

Analysis of suctions is hindered by several factors: (1) discontinuity in the records (psychrometers and hygrometers stop measuring when entering in contact with liquid water and some rainfall events caused electrical supply to fail); (2) spatial variability (suctions can be highly variable, especially under dry conditions); and (3) reliability because of sensors malfunction. Still, some patterns can be observed.

Figure 4.8 displays the evolution of the daily mean soil matric suction at several layers in Test I (left) and Test II (right). The biggest oscillations in suction are observed in the top layers with highest values during dry periods and abrupt drops during wet periods. The effect of rain episodes can be seen clearly in most top soil sensors. Suction builds during dry periods and drops abruptly after major rainfall events. Sensors in the soil layer (some 60cm depth) display a similar behavior and suggest that the soil capillary barriers were working, at least until the winter of 2009-2010. Section 3 dries (reaches high suctions) later than either sections 1 or 2 and remains slightly wetter than them, which suggests that water is flowing laterally towards section3. In fact, low suctions are not reached in the cobble layer until the anomalously high rains of fall2009 and winter 2009-2010, when water appears to break through the capillary barrier. Unfortunately, suctions were hardly recorded at the sand drain above the clay. In contrast, in the soil layer of Test II, though displaying a more erratic behavior, it is clear that water broke through the capillary barrier in the

spring of 2009, when suctions dropped in the cobble layer. Therefore, water infiltrates into Test II sooner than in Test I. The behavior of Test II is unexpected as the soil layer and the underlying coarse material were meant as a first capillary barrier. The contrast between the two materials is even bigger in Test II than in Test I, (soil on top of cobble instead of soil on top of sand) therefore Test II should be hindering vertical flow as much as Test I. We contend, however, that this bigger contrast caused by the absence of the sand and gravel layer, present in Test I (acting as a filter), may be a weakness of this cover. The soil layer appears to be hydraulically connected to the cobble layer due to either contamination to the cobble layer by soil material (possibly because of burrowing activity perforating the geotextile) or flow driven by instabilities caused by the irregular contact surface between the materials.

Suctions in the clay layer remain constant and low, at values that according to the conducted laboratory test (*Villar and Fernández*, 2011) indicate that clay layers are saturated. Data in the sand layer between the two clay in Test I was hardly recorded, just allowing to see that suctions decrease after the 2010-2011 winter.

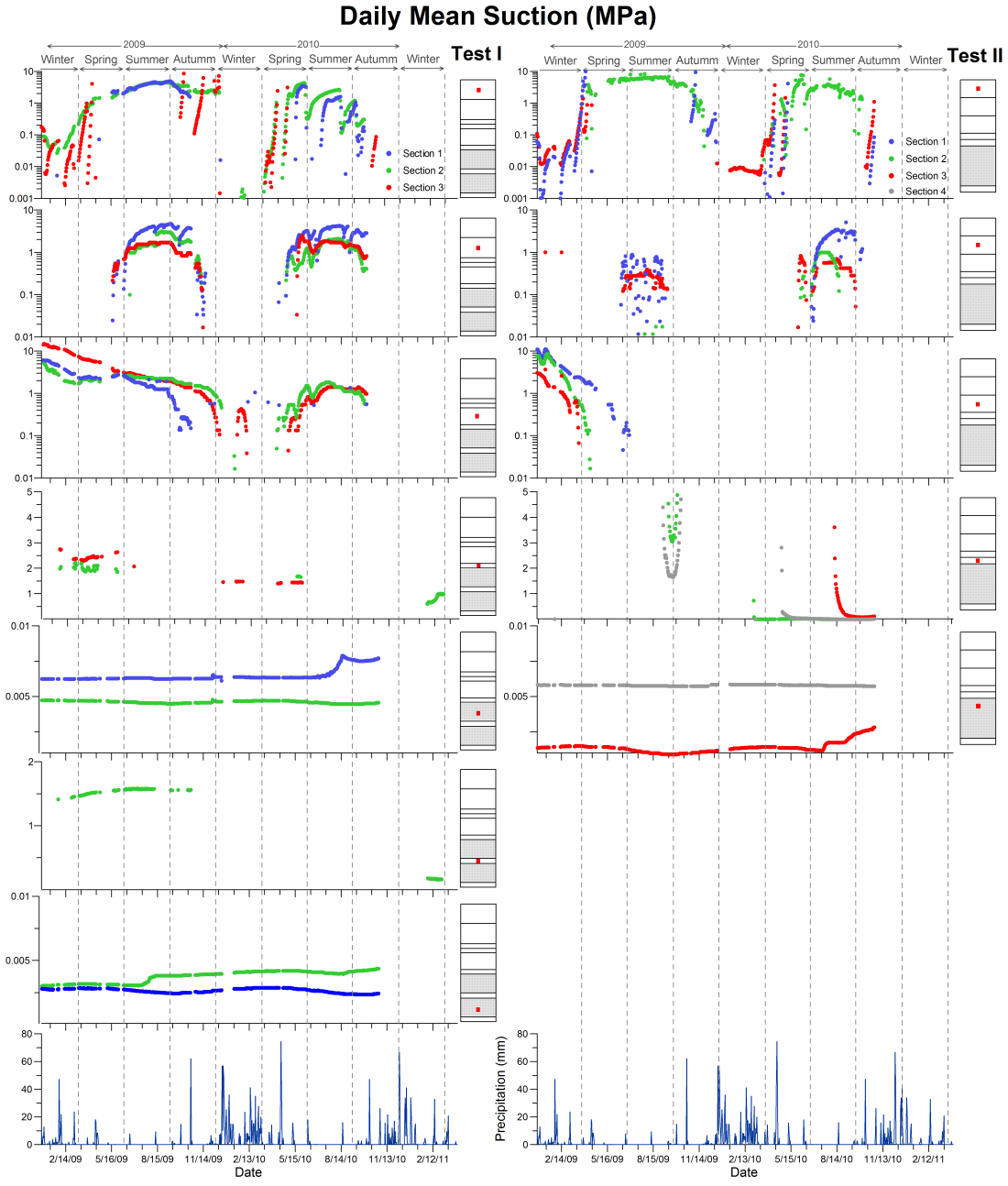

Figure 4.8: Time evolution of the daily mean suctions at several depths during 2009 and 2010 for Test I (left plots) and Test II (right plots). A red point next to each plot indicates the sensor position in the cover. The precipitation is displayed in the bottom plots.

The analysis of infiltration by suction data is complemented with the volumetric water content (θ) data recoded by the TDR sensors (Figure 4.9). Water content data display a better continuity in time than suction data, which facilitates analysis, but available only for the second year (2010).

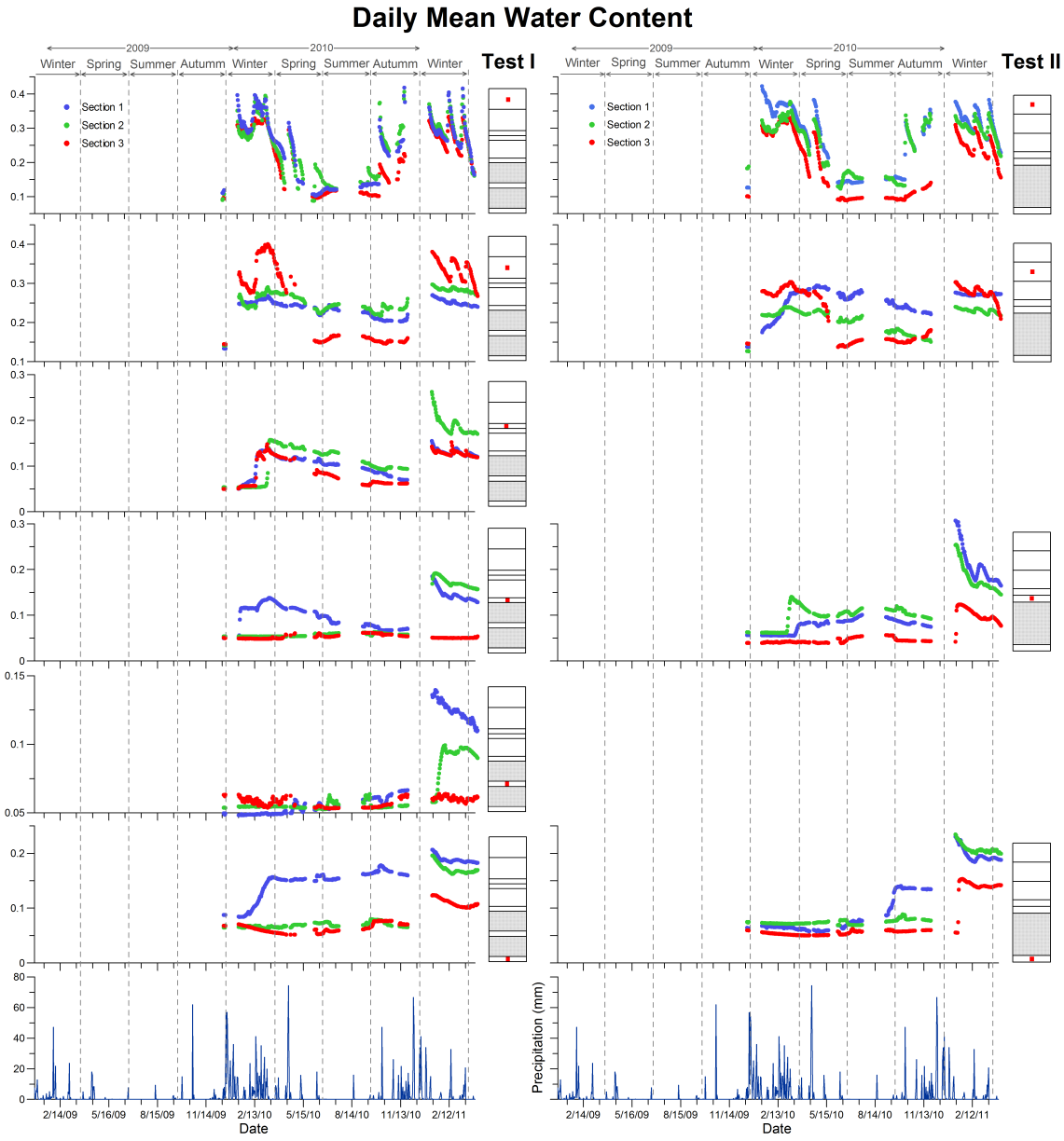

Figure 4.9: Time evolution of the daily mean soil water contents at several depths during 2009 and 2010 for Test I (left plots) and Test II (right plots). A red point next to each plot indicates the sensor position in the cover. The precipitation is displayed in the bottom plots.

In both tests, water content data show the largest fluctuations in the first layer, higher values during wet periods and lower and less variable values during dry periods. The effect of rain episodes can be clearly seen in both tests. The alternation of high and low θ values corresponding to water entries and the subsequent soil drying are evident and present in the three sections of both

covers. As section 3 is located in the slope zone, which promotes larger lateral water diversion, this section dries faster after rainfall events and exhibits the lowest θ values during the summers. At the second layer (soil), the oscillations are smaller than in the first layer, presenting the lowest θ values during the dry periods and the highest at the end of the second year. Here, section 3 displays lower θ values than sections 1 and 2 during the summers, but not during the rainy seasons when θ values are much higher than the ones in section 1 and 2. Furthermore, the oscillations are larger and faster than in the platform zone sections. These observations support the hypothesis of a marked capillary barrier effect, which leads to a lateral flow going from the platform sections to section 3 and causing the sudden increase in section 3 water content during the rainfall events. As this section is in the sloped zone, this high water content is not retained for a long time and it is laterally deviated causing the fast decrease in θ after the rain episodes. This lateral infiltration arrival and its fast removal generates big oscillations in the water content of section 3. When comparing Test I and Test II it can be seen that this mechanism is less pronounced in Test II, which we attribute to the capillary effect breaking more easily in Test II than in Test I. Then water storage in its soil layer is lower, generating less horizontal flow to the slope zone than in Test I. This interpretation is consistent with the analysis of suction data discussed earlier.

The third plot of Test I shows the water content evolution in the sand layer below the soil. An increase of θ can be seen in the winter 2009-2010 after the intense rains occurring during this period. θ decreases during the spring and summer of 2010 to increase again after the rains in the 2010-2011 winter. These increases are expected in section 3, which reached saturation at the soil layer above during the same episodes, but not in sections 1 and 2, which did not. We conjecture that this contradiction may reflect the spatial variability in the water contents at the soil layer in the platform, which may have become locally saturated at points other than the monitored ones. This increase in water contents in the sand layer did not make it across the filter during the winter 2009-2010 in sections 2 and 3. Water contents in the sand above the clay layer (fourth plot) increased in sections 1 and 2, but not in 3 during the 2010-11 winter, suggesting that the capillary barrier is performing better in section 3 (in the slope zone) than in section 1 and 2.

The last plot displays the suctions in the sand layer at the base of the covers. Water content remains stable during most of the year for both tests until a sudden increase takes place. This increase occurs in Test I in the winter of 2010 and for Test II in the winter of 2011. This θ increase in section 1 is due to the type of vertical flow that takes place from the clay to the sand. As the clay presents a very low permeability, the entry of the water flow into the sand does not occur in an homogeneous water front but through preferential flow paths (*Rezanezhad et al.*, 2006). This type of flow is then more difficult to catch by the sensors and, at the same time, is expected to occur more easily in section 1 (where the lower slope shortens the capillary length). Besides, when water entries are more sporadic they are more likely recorded in section 1. When the infiltration becomes larger, as occurs in the spring of 2011 for both tests, the θ increase is captured in all the sections. Furthermore, the sand is not close to saturation, not even during the periods with the higher θ values.

4.5 Conclusions

Two field-scale multilayer covers have been set up in a semiarid climate where the majority of the rain falls when evapotranpiration rates are low. Two designs have been tested to compare different layer combinations. Their effectiveness is been analyzed by means of an extensive monitoring system.

The two upper layers, which rely on evapotranspiration to remove water from the system, proved effective in minimizing percolation by holding water during wet periods and evapotranspirating it during the dry ones. The filter-biointrusion barrier placed in Test I showed better results in preventing percolation than Test II. These layers made the upper part of Test I more effective, leading to a lower percolation reaching the top. It has also been shown that in a year with rain average, 2009, infiltration reaching the sand above the clay layers is much lower than after an extremely wet year (2010 and beginning of 2011). Regarding the capillary barriers performance, they both work well during 2009. For a wet year it is shown that capillary breakthrough occurs

but as a preferential flow only, mainly in the flat part of the covers. After the rainy year (2010) and the next spring (2011), saturating both covers show a general infiltration in all the sections, but without showing the saturation of the sand layers at the bottom of the covers.

The instrumentation designed for the cover displayed a highly varying usefulness. The temperature measurements were used to study the heat fluxes in the soil. TDRs yielded qualitatively, and perhaps quantitatively, reasonable results in all but the clay layers. Matric potential sensors were helpful in the sand layers and in the topsoil (although they went out of range during the driest periods). Hygrometers were useful in the upper layers, adding data when matric potential sensors went out of range. Tensiometers and psychrometers data were not very useful in the soil layers. Psychrometers failed to yield measurements either due to the relative humidity values too close to saturation or because they do not function correctly in direct contact with liquid water. Data from the tensiometers in the upper layers was erratic and not reliable. These difficulties suggest that other monitoring systems might have been more useful. Certainly, drainage rate should have been monitored. Also, electrical resistivity tomography (ERT) might have helped in providing a useful picture of water distribution in the whole cover.

In spite of these difficulties, we can conclude that the upper portion of the Test I cover did work as planned. Lateral water flow through the soil layer proved the effectiveness of the first capillary barrier and identified the importance of the slope to enhance lateral drainage. We recommend the use of the Test I filter-biobarrier combination (including the sand and gravel layers between the soil and the cobble layer) to ensure the first capillary barrier performance. The lower infiltration barrier were not completely effective during a rain average year and did not work in an extremely wet year. Nevertheless, the base sand layers did not reach saturation and water did not infiltrate in large quantities. Acknowledging that construction of a very low permeability layer (of around $10^{-}9$ m/s) is very difficult, we propose modifying the design to ensure that the sand layer above the clay layer remains under suction conditions most of the time. This can be achieved by (1) increasing the slope of the platform zone to accelerate lateral drainage; and (2) using a more

retentive sand (small grain size 0.2 mm) to ensure hydraulic connectivity.

Chapter 5

Effect of thermal gradients and rainfall on vapor diffusion in a dry soil

5.1 Introduction

Unsaturated flow plays an important role in several environmental and water resources phenomena: aquifer recharge, contaminant transport, soil salinization and many others. Under dry conditions, with little or no recharge and high temperature and vapor pressure gradients, vapor diffusion becomes significant (*Ross*, 1984; *Scanlon and Milly*, 1994).

Historically, one of the main obstacles in field studies on unsaturated flow and vapor diffusion is the combination of a low magnitude of water fluxes with the limitations of the measurement techniques (*Scanlon et al.*, 1997). Moreover, the direction and magnitude of vapor fluxes is spatially and temporally highly variable. This complicates the study of vapor fluxes and requires analysis under different conditions (night/day, dry/wet, etc.).

Several studies have been conducted on vapor flow for different conditions. *Rutten et al.* (2010); *Jimenez-Martinez et al.* (2012) among others, focused on flow in the shallow subsurface below

irrigated fields while *Scanlon* (1992); *Scanlon and Milly* (1994) and *Milly* (1996) concentrated on arid and desert zones. *Rutten et al.* (2010) studied the two month evolution of soil moisture under irrigated conditions obtaining a 10mm/yr upward vapor diffusive flux. Under completely different conditions, a desert soil, *Scanlon* (1992) used Chlorine 36 and Tritium tracers in combination with numerical modeling to evaluate flow processes. Observed vapor fluxes were two to eight orders of magnitude higher than liquid fluxes and a net downward vapor flux was suggested. *Scanlon and Milly* (1994) studied the temporal variation of these vapor fluxes in a subtropical arid region. Unfortunately, water potential was not measured in the first soil meter, exactly where variations are expected to be greater. However, they conjecture that the downward driving force for vapor flow during the summer is the temperature gradient. *Milly* (1996) developed a quantitative description of these diffusive vapor fluxes including the dynamic nature of thermal gradients in the work of *Scanlon* (1992). Calculated thermal vapor fluxes were downward for one half of the year (-5 to -15mm/yr) and upward for the other half (5 to 50mm/yr), with a net downward annual thermal vapor flux.

Nevertheless, there remain many unanswered questions: is the daily net vapor flux only downwards and does it always occur during the summer? what would be the effect of episodes with high precipitation during months with low evapotranspiration? does the daily change in vapor flux direction behave the same along the year? With the aim of answering these questions and enhancing our understanding of vapor flux behavior, we study in detail, daily and annual variations of vapor fluxes under natural weather conditions, in a semiarid area (with dry summers and wet winters) and for the first meters of soil. To do so, we analyze a two year data set registered by a monitoring system of a field-scale cover study.

5.2 Materials and Methods

5.2.1 Monitoring System

The site is located in Córdoba (southern Spain), at El Cabril, the Spanish facility for disposal of low and intermediate-level radioactive waste (Fig. 5.1). The waste is protected by a sequence of barriers and the final confinement will be a multilayer cover. A pilot cover has been built at the same facility to test its capacity to minimize vertical water flow (liquid and vapor) and to study the interaction of heat and water flow under natural weather conditions. To this aim, an extensive monitoring system has been installed. Temperature, suction and water content, among others soil variables, are recorded through the whole soil profile (2.8m thick).

The pilot cover and the monitoring system are extensively described in the previous chapter. Here we focus only on sensors used for deriving vapor fluxes. Relative humidity (RH) was measured using psychrometers (for medium soil water contents) and hygrometers (for low soil water contents). Both types of sensors record temperature as well. Their distribution in depth and the different soil layers in the cover are also shown in Figure 5.1. All sensors have been installed ensuring good contact between the sensor and the soil. The wiring orientation is horizontal, parallel to the layering, so as to minimize disturbance to vertical fluxes. Hygrometers and psychrometers record data hourly and every 21 minutes respectively. Data were recorded for two years (2009 and 2010).

Data from the meteorological station at the site is also available. Temperature, wind speed, wind direction, relative humidity, solar radiation and precipitation are recorded hourly. Climate is semiarid with mean annual precipitation from 2004 to 2013 of 613mm (Figure 5.1). Most of the rain falls during the winter and the rest is distributed mainly among autumn and spring. Most of the years have a precipitation between 416 and 628mm. At one end of the range there is an extremely dry year, 2005 with 189.5mm, and at the other end a year which doubles the annual

mean, 2010 with 1271mm. Notice that 2010 is one of the two years analyzed in this study. We will be comparing an average, 2009, with an extremely wet year, 2010.

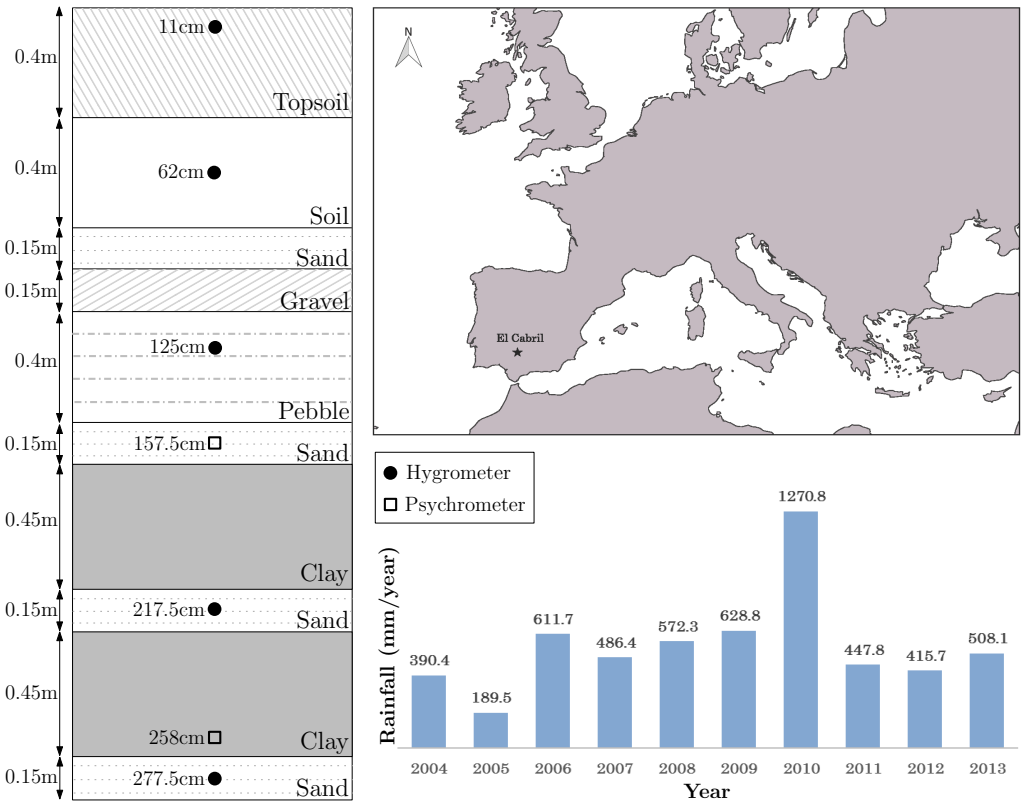

Figure 5.1: Left, spatial distribution of the sensors and layers in the pilot cover. Bold circles stand for hygrometers and empty squares for psychrometers. The label besides each sensor indicates its depth. The location of the site in Córdoba, south Spain, and its historical annual precipitation are on the right.

5.2.2 Methodology for field data interpretation

We analyze diffusive water vapor and energy fluxes from temperature and vapor pressure data.

Vapor pressure (Pv) is obtained from

$$Pv = RH \cdot Pv_{sat} \tag{5.1}$$

where Pv_{sat} is saturated vapor pressure and RH is relative humidity. Numerous expressions are available for Pv_{sat}. We have used the one by *Murray* (1967):

$$Pv_{sat} = 611\ exp(17.27T/(237.2 + T)), \quad [Pa], \quad T[^oC] \tag{5.2}$$

With the calculated Pv, we can obtain the diffusive flux of water vapor between two depths in the soil by Fick's Law (*Philip and de Vries*, 1957):

$$J_v = M_w\ \theta_g\ \tau\ D_0\ \frac{1}{R(T + 273.16)}\ \frac{\partial Pv}{\partial z}, \quad [kg\, m^{-2} s^{-1}] \tag{5.3}$$

Where J_v is diffusive vapor flux, M_w is molecular weight of water (0.018kg/mol), θ_g is volumetric gas content, τ is factor accounting for tortuosity and constrictivity, D_0 is vapor diffusivity in air and R is the gas constant ($8.31 J/mol/K$). We have neglected here vapor diffusion enhancement ($\tau = 1$). Actual application of this equation requires several approximations. First, the P_v gradient is approximated as an incremental ratio between the two points where vapor flux is being calculated. Second, θ_g, τ, and D_0 are likely to evolve in time, so as to be minimum in winter, where temperature is minimum and water content may be highest. For the sake of simplicity, we have taken them as constant ($\theta_g = 0.2$, $\tau = 1$, and $D_0 = 2.4 \cdot 10^{-5} m^2/s$). Heat fluxes are also computed to assess the effect that vapor diffusion may have on energy balances. For comparison purposes, the total heat flux in the soil (J_{heat}) is evaluated as the sum of the advective flux caused by vapor (basically latent) heat ($J_{adv_{vap}}$) plus the conductive heat flux (J_{cond}) described by Fourier's Law (i.e., advective heat fluxes of liquid water are neglected). These fluxes are given by:

$$\begin{aligned} J_{heat} &= J_{cond} + J_{adv}, \quad [Jm^{-2}s^{-1}] \\ J_{cond} &= -\lambda \cdot \nabla T \\ J_{adv} &= [L_0 + C_v T] J_v \end{aligned} \tag{5.4}$$

Where L_0 is latent heat of vaporization ($2.5 \cdot 10^6 J/kg$), C_v is heat capacity of water vapor at constant volume ($1.93 KJ/kg/K$) and λ is thermal conductivity (values shown in Table 5.1).

Table 5.1: Soil thermal conductivity obtained at the laboratory by Villar2011b.

	Vegetal Soil	Soil	Sand	Clay
$\lambda[W/mK]$	0.9	1.8	0.25	1.5

Hourly data are used to study the daily fluctuations of the water vapor and heat fluxes. To analyze the seasonal variability, daily means of temperature and RH are calculated by averaging a minimum of 20 hourly values for each day. If this minimum is not reach, then no mean value is computed for this day. Other reasons for not having data include: sensor out of range, direct liquid contact with the sensor (when the sensor gets dry again, it restarts data collection) or lack of electric supply caused by big rainfall events at the site.

5.2.3 An approximate analytical solution

A fairly good approximation to temperature can be obtained by assuming that (1) surface temperature fluctuates sinusoidally with both a daily and a yearly period and (2) heat transfer is controlled by conduction. Following the approach of Jacob (1950) and Ferris (1951), it is easy to show that the temperature distribution is:

$$T(t,z) = T_{my} + f_d(t,z) + f_y(t_d,z) \tag{5.5}$$

where z is depth below the surface, t is time, t_d is Julian day (functions of t_d are treated as constant during the day), f_d(t,z) is daily temperature fluctuation and $f_y(t_d,z)$ is yearly temperature fluctuation:

$$f_d(t,z) = A_d e^{-\alpha_d z} sin(\beta_d), \quad \beta_d = \omega_d(t - t_{0d}) - \alpha_d z \tag{5.6}$$

$$f_y(t_d,z) = A_y e^{-\alpha_y z} sin(\beta_y), \quad \beta_y = \omega_y(t_d - t_{0y}) - \alpha_y z \tag{5.7}$$

where t_0 is the time with mean temperature, $\omega = (2\pi/P_i)$ is the frequency, A_i is the amplitude, α_i is the decay (with depth) constant and P_i is the period (365.25 days for i=y, and 1 day for i=d).

The decay constants, inverse of damping depths (L_i), are given by:

$$\alpha_i = 1/L_i = \sqrt{\omega_i C/(2\lambda)}, \quad i = d, y \tag{5.8}$$

Daily amplitude is assumed to change along the year as:

$$A_d(t_d) = A_{md} + \Delta A_d \sin(\omega_y(t - t_{0A})) \tag{5.9}$$

where A_{md} and ΔA_d are mean and range of daily amplitude of temperature fluctuations. t_d is Julian day (i.e. A_d is assumed constant during each day) and t_{0A} the day with mean amplitude.

Assuming that vapor pressure in soil is saturated we can rewrite equation 5.3 as

$$J_v = \frac{M_w\, D_p}{R(T + 273.16)} \frac{dP_{vsat}}{dT} \frac{\partial T}{\partial z} \tag{5.10}$$

The last term can be obtained from equation 5.5. As for the second term, we have approximated it as

$$E(T) = \frac{1}{(T + 273.16)} \frac{dP_{vsat}}{dT} = aT^2 + bT + c \tag{5.11}$$

A 99.97% correlation in the range from 5 to 41^oC was obtained with $a = 5.87 \cdot 10^{-4} Pa\ ^oC^{-4}$, $b = 2.52 \cdot 10^{-3} Pa\ ^oC^{-3}$ and $c = 0.205 Pa\ ^oC^{-2}$.

For the purpose of computing average fluxes, we separate daily and yearly fluctuations, which allows us to write

$$J_v = -\frac{M_w\, D_p}{R} \left[a f_d^2 + E'(T_{md}) f_d + E(T_{md})\right] \left(\frac{\partial f_d}{\partial z} + \frac{\partial f_y}{\partial z}\right) \tag{5.12}$$

$$with \quad \frac{\partial f_i}{\partial z} = -\alpha_i A_i e^{-\alpha_i z} \sqrt{2} sin(\beta_i + \frac{1}{4}\pi), \quad i = d, y \tag{5.13}$$

Where $E'(T_{md}) = (2aT_{md} + b)$ is the derivative of equation 5.11, and $T_{md} = T_{my} + f_y(t_d, z)$ is the mean temperature during each day. The first term represents vapor flux driven by daily

temperatures fluctuations, which is usually much larger at shallow depths than the second term, which represents fluxes driven by yearly fluctuations of temperature. Integrating over every day and dividing by the day length (Pd), we obtain the mean daily flux:

$$\bar{J}_{vd}(t_d, z) = -\frac{M_w\, D_p}{2R}\left(-\alpha_d\, E'(T_{md})A_{dz}^2 + (aA_{dz}^2 + 2E(T_{md})\right)\frac{\partial f_y}{\partial z} \tag{5.14}$$

Where $A_{dz} = A_d(t_d)e^{-\alpha_d z}$ is the amplitude of daily fluctuations.

Integrating equation 5.14 over a year and dividing by the length of a year (Py), we obtain the mean yearly flux $\bar{J}_{vy}(z) = \bar{J}_{vyd} + \bar{J}_{vyy}$, as the sum of the mean yearly fluxes driven by daily and yearly fluctuations, respectively:

$$\bar{J}_{vyd} = \frac{M_w\, D_p\, \alpha_d\, A_{md}^2 e^{-2\alpha_d z}}{2R}\left(-E'(T_{my})\left(1 + \frac{1}{2}\left(\frac{\Delta A_d}{A_{md}}\right)^2\right) + 2aA_y\left(\frac{\Delta A_d}{A_{md}}\right)\cos(\beta_A)e^{-\alpha_y z}\right) \tag{5.15}$$

$$\bar{J}_{vyy} = \frac{M_w\, D_p\, \alpha_y\, A_y^2 e^{-2\alpha_y z}}{2R}\left(E'(T_{my}) + aA_{md}\frac{\Delta A_d}{A_y}\left(\cos(\beta_A) - \sin(\beta_A)\right)e^{(\alpha_y - 2\alpha_d)z}\right) \tag{5.16}$$

Where $\beta_A = \omega_y(t_{0y} - t_{0A}) - \alpha_y z$ quantifies the phase shift of yearly fluctuations in daily temperature amplitude.

Equations 5.15 and 5.16 become more comprehensible when the range of daily temperatures fluctuations (ΔA_d) is assumed zero. Then the mean yearly flux reduces to

$$\bar{J}_{vy} = \bar{J}_{vyd} + \bar{J}_{vyy} = \frac{M_w\, D_p\, E'(T_{my})}{2R}\left(\alpha_d\, A_{md}^2\, e^{-2\alpha_d z} + \alpha_y\, A_y^2\, e^{-2\alpha_y z}\right) \tag{5.17}$$

This is the sum of two terms, the first being a daily term decreasing exponentially with a damping depth of $(2\alpha_d)^{-1}$ and the second, a yearly term decreasing with a damping depth of $(2\alpha_y)^{-1}$.

It is interesting to notice in equation 5.17, that the mean yearly vapor flux (1) is always down-

wards while daily fluxes (Eq. 5.14) may be upwards or downwards; (2) is very sensitive to temperature fluctuations (factors A_i^2) and increases with mean temperature (factor $E'(T_{my})$), so that it can be high in mid- and high latitude arid environments, and (3) decays exponentially with depth, but with a damping depth equal to half that of temperature. The latter implies a relatively low penetration for daily fluctuating vapor fluxes, but it may still be significant (below root depth) for vapor fluxes driven by seasonal fluctuations of temperature.

5.3 Results

5.3.1 Results for the Direct Measurements

Figure 5.2 displays the daily mean evolution of RH and temperature recorded by sensors and vapor pressure calculated using equation 5.1. Daily precipitation is shown at the bottom. RH ranges between 98% and 100% for most sensors, except the shallowest one (11cm depth), which fell to 88% during the summer of 2009. Low RH was also recorded initially by the sensor at 125 cm depth (cobble layer), which we attribute to the layer being initially dry. Temperature records display the expected seasonal variations with summer maxima much higher than air temperature, which reflect the high radiation and low soil moisture, and winter minima similar to air temperature. Temperature fluctuations penetrate into the soil with a significantly delay and a decrease in amplitude. As a result, temperature decreases with depth during summer and increases during the winter.

The evolution of calculated Pv resembles closely that of temperature. This reflects the fact that RH is close to 100% and Pv very close to Pvsat, which is a function of temperature. Consequently, Pv values are highest during the summer close to the surface (11cm depth) and have similar values with depth and decrease with depth, whereas the opposite occurs during the winter. Atmospheric and soil Pv have similar values during the winter and differ most during the summer. This is related to the higher evaporation during the summer.

Calculated water and energy fluxes are shown in figure 5.3. These fluxes are calculated only for the upper part of the soil because we consider that diffusive vapor flux does not occur in clay layers. The diffusive vapor fluxes range from 0 to 3.4mm/year. The maximum daily flux (upwards) is 2.3mm/year while the minimum mean value (downwards) is -3.4mm/year. The magnitude of both vapor and heat fluxes and their oscillations are larger near the surface, from 11 to 62cm depth and decrease with depth. The diffusive vapor and heat fluxes are mainly upwards in wintertime and downwards during the summer months. In 2009 the downward fluxes start at the beginning of spring while in 2010, the wetter year, they do not start until mid spring. Major rainfall events cool the soil surface, thus changing the direction of the fluxes. Table 5.2 displays the annual mean of the diffusive vapor fluxes for 2009 and 2010 for two different intervals of the soil.

Table 5.2: 2009 and 2010 diffusive vapor flux annual means for two different intervals. Upwards, positive values, and downwards, negative. Each year and depth presents the total daily annual mean and, in brackets, the total of downward and upward fluxes separately.

	$J_{v_{11-62cm}}[mm/yr]$	$J_{v_{62-125cm}}[mm/yr]$
2009	-0.15 (-0.52, 0.37)	-0.44 (-0.66, 0.22)
2010	-0.42 (-0.7, 0.3)	-0.33 (-0.59, 0.26)

Table 5.3 shows the maximum and minimum value of the diffusive vapor fluxes for both years and for the two different soil sections. Negative values, downward fluxes, and positive values, upward fluxes.

Table 5.3: Maximum (upwards flux) and minimum (downwards flux) value for the diffusive vapor flux in 2009 and 2010 and for the two different soil segments.

	$J_{v_{11-62cm}}[mm/yr]$	$J_{v_{62-125cm}}[mm/yr]$
2009, Max	2.94	1.2
2009, Min	-4.2	-2.17
2010, Max	3.11	1.1
2010, Min	-5.2	-2.3

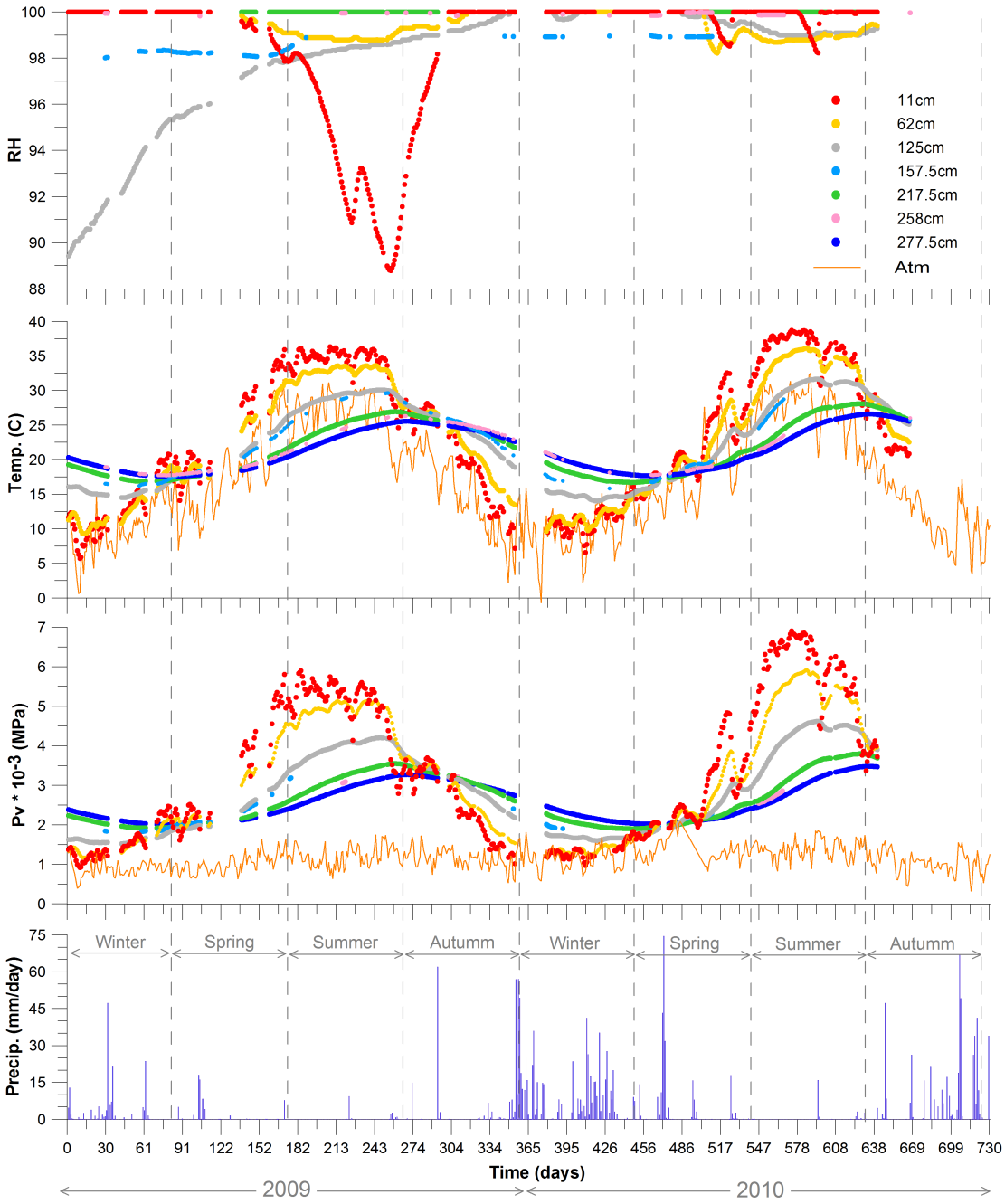

Figure 5.2: Daily mean evolution of relative humidity (RH), temperature and vapor pressure (Pv) at seven different depths. Points represent hourly data collected by sensors and orange line stands for atmospheric temperature and vapor pressure measured by meteorological station. Daily precipitation is shown at the bottom of the graph and gray dotted vertical lines point season changes.

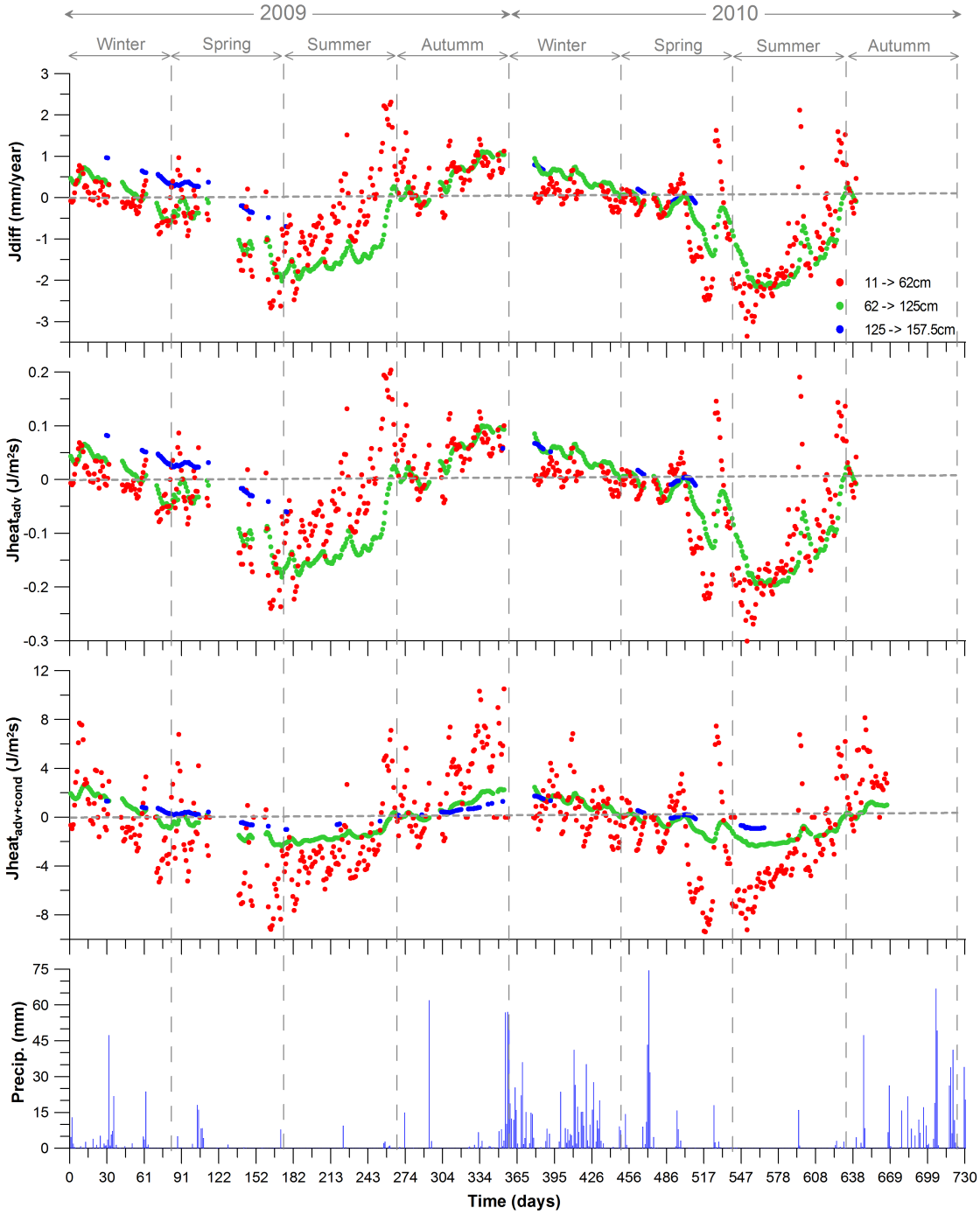

Figure 5.3: Evolution of the daily mean of diffusive vapor flux, advective heat flux and the sum of advective and conductive heat fluxes for 2009 and 2010. These fluxes are calculated between the following depths: from the surface to the base, from 11cm to 62cm, from 62cm to 125cm and from 125cm to 157.5cm. Positive values represent upward fluxes towards the soil surface and negative values, downward fluxes. The precipitation record is at the bottom of the figure and the gray dotted vertical lines stand for season changes.

To study the behavior at a daily scale we selected a period in summer (August 10th-17th, 2009) and in winter (January 21th-29th, 2010). Both periods contain a rainfall event. Figure 5.4 and 5.5 show, for the summer and winter period, respectively, hourly evolutions and diurnal and nocturnal profiles of both before and after the rainfall.

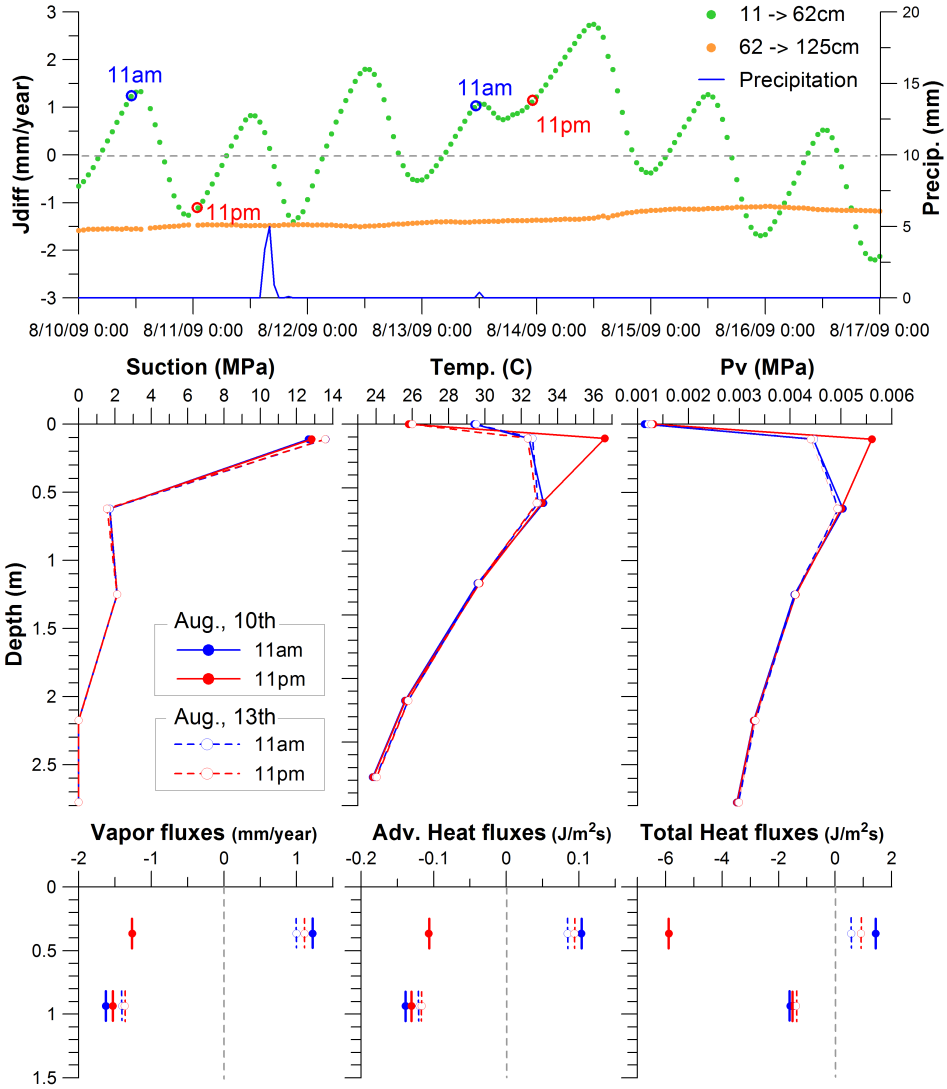

Figure 5.4: At the top, hourly evolution of vapor diffusion fluxes from 11 to 62cm and from 62cm to 125cm depth during summer time, before and after a rainfall event. Below, profiles of suction, temperature, vapor pressure, diffusive vapor flux, advective heat flux and the sum of advective and conductive heat fluxes at two specific day times (11am and 11pm), before the rain (August 10th, solid lines) and after the rain (August 13th, dotted lines). Positive and negative values represent upward and downward respectively. Meteorological recorded data is used to represent the surface data (0cm depth) in Pv and temperature profiles.

In summer (Fig. 5.4), the diffusive vapor flux at the upper part of the soil, from 11 to 62cm, clearly shows the daily oscillations with a minimum of -2.2mm/yr and a maximum of 2.7mm/yr. These oscillations do not propagate to the deeper interval of 62 to 125cm depth. The 11-62cm vapor diffusion flux presents positive values during morning and negative values during afternoon and night. After a rainfall event, fluxes stay positive during all day to decrease again to a negative values a couple of days later. Rainfall provides water for evaporation, thus cooling the soil surface and promoting upwards vapor diffusion. The 62-125cm vapor diffusion flux remains negative and almost constant.

Before (Aug, 10th) and after the rain (Aug, 13th), suction decreases with depth and barely change in time. Temperature decreases with depth, below 62cm. Above it, daily oscillations cause temperature gradients to change in magnitude and direction. In the morning, temperature at 11cm is still lower than at 62cm depth, while at night the gradient is inverted and the highest temperature occurs at 11cm (due to previous hours of insulation). After the rain, values at 11cm remain lower than at 62cm during all day. The evaporation after the rain, cools the soil and generates an upward gradient towards the surface. Pv profile behaves as the temperature profile, showing the Pv dependence with temperature. At night and before the rain, the positive Pv gradient below 11cm promotes the downward vapor flux along the soil profile (see vapor fluxes plot, down to the left of the figure). In the morning, before rain and all day after rain, gradients are negative above 62cm leading to an upward vapor flux (positive values). Gradients are positive below 62cm, causing a downward vapor flux. Therefore, below 62cm vapor fluxes are always downwards, while above it vapor fluxes alternate direction depending on the time of the day and the occurrence of rain. Consequently, advective heat fluxes follow the same behavior. Total heat fluxes (advective plus conductive) act likewise but with larger values.

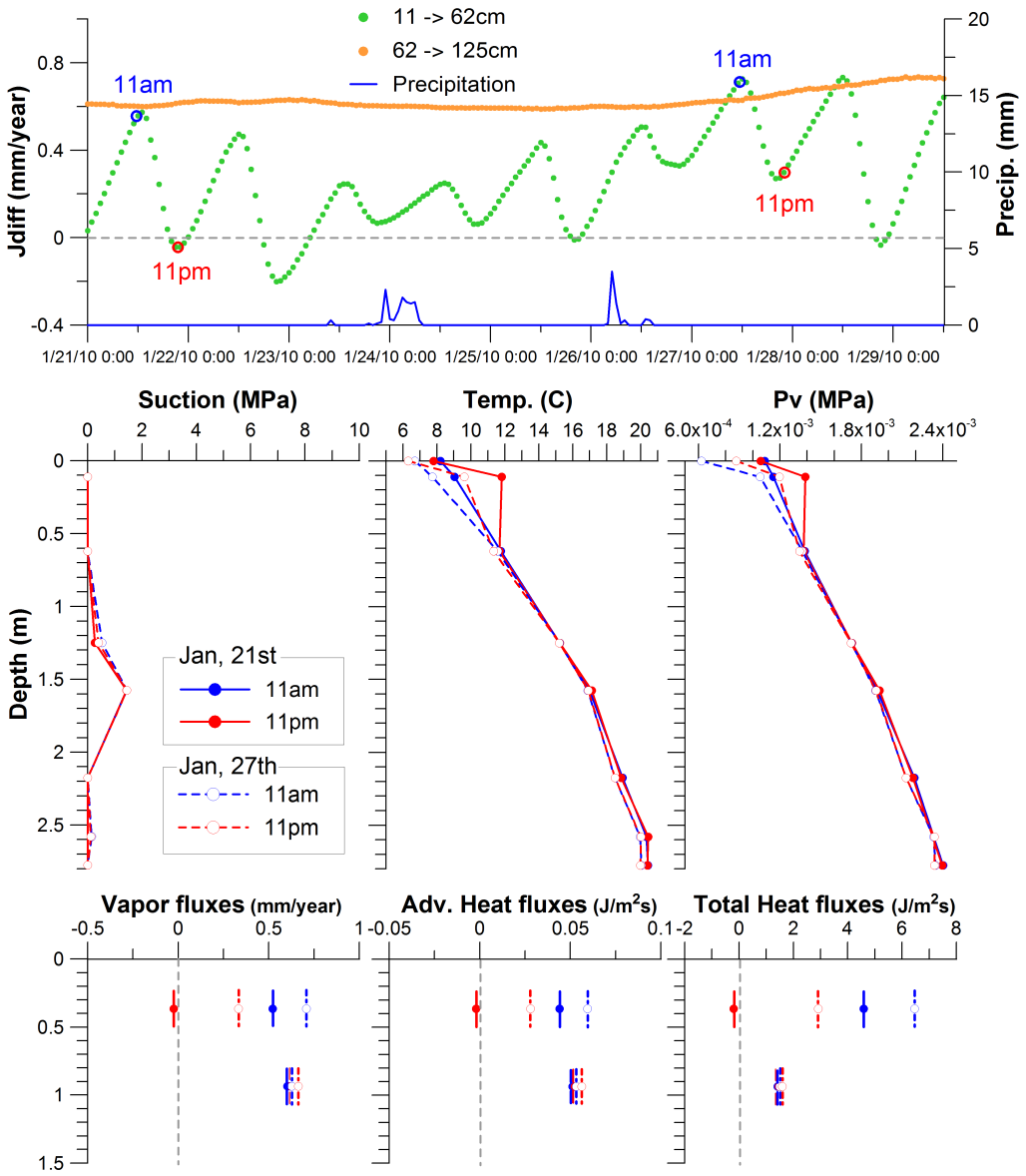

Figure 5.5: At the top, hourly evolution of the vapor diffusion flux from 11 to 62cm and from 62cm to 125cm depth during winter time, before and after a rainfall event. Below, profiles of suction, temperature, vapor pressure, diffusive vapor flux, advective heat flux and the sum of advective and conductive heat fluxes at two specific times a day: 11am and 11pm, before the rain (January 21st, solid lines) and after the rain (January 27th, dotted lines). Positive values represent upward fluxes towards the soil surface and negative values downward fluxes. Meteorological recorded data is used to represent the surface data (0cm depth) in Pv and temperature profiles.

The upper part of the figure 5.5 shows the hourly evolution of the vapor diffusive fluxes from 11 to 62cm and from 62 to 125cm together with the hourly precipitation (right axis) for the winter

period. The diffusive vapor flux close to the soil surface, from 11 to 62cm, clearly shows the daily oscillations with a minimum of -0.2mm/yr and maximum of 0.7mm/yr (almost one order of magnitude smaller than in the summer period, Fig. 5.4). The 11-62cm vapor diffusion flux presents positive values during most of the day time and negative values only during a few hours at night. After a rainfall event, the magnitude of the fluxes increases and remain positive during all day. A few days later, vapor fluxes diminish and return to negative at night. These oscillations do not propagate to diffusive vapor flux at the 62 to 125cm interval, which remains almost constant and positive (the opposite of the summer period). Notice that the magnitude of the vapor fluxes is smaller in winter (Fig.5.5) than in summer (Fig.5.4).

Before (Jan, 21st) and after the rain (Jan, 27th), suction profile remains close to zero during all day, while temperature and Pv display negative gradients through the bottom of the cover for all times except for the 11cm depth at 11pm before the rain. At this point, temperature and Pv are higher than at 62cm depth, leading to a change in temperature and Pv gradients. This generates a downwards gradient that leads to a negative vapor flux from 11 to 62cm depth. At 11pm after the rain, when evaporation has cooled the soil, temperature at 11cm starts to rise but remains lower than at 62cm depth. Therefore, Pv gradient is negative along the whole soil profile, leading to an upward vapor flux. From 62cm to 125cm the Pv gradient is always negative generating upward vapor fluxes. Advective heat fluxes follow the behavior of vapor fluxes. Total heat fluxes (advective plus conductive) act likewise but in larger amounts. Fluxes from 62 to 125cm depth were always downwards during the summer (Fig.5.4) and upwards during the winter (Fig.5.5).

5.3.2 Results of the Analytical Solution

When comparing the temperatures calculated by the analytical solution with the field temperatures, some of the parameters describing temperature fluctuations in the analytical solution 5.5 were fitted to observations. Thermal conductivity (λ) was taken equal to 0.8 W/mK to calculate temperatures at all depths except at 125cm depth (cobbles) where $\lambda = 0.7 W/mK$ was taken. Notice

that λ is included in the damping depth calculation (Eq.5.8) and that these λ values were chosen to represent all the different layers above each depth. For $C = 2 \cdot 10^6 J/m^3/K$, we obtain $L_d = 0.11m$ and $L_y = 2m$. The other fitted parameter was the range of daily amplitude of temperature fluctuations (ΔA_d), which was diminished from 6 to 2°. Figure 5.6 displays the temperature registered by the sensors against the calculated (5.5) along one year and for different depths.

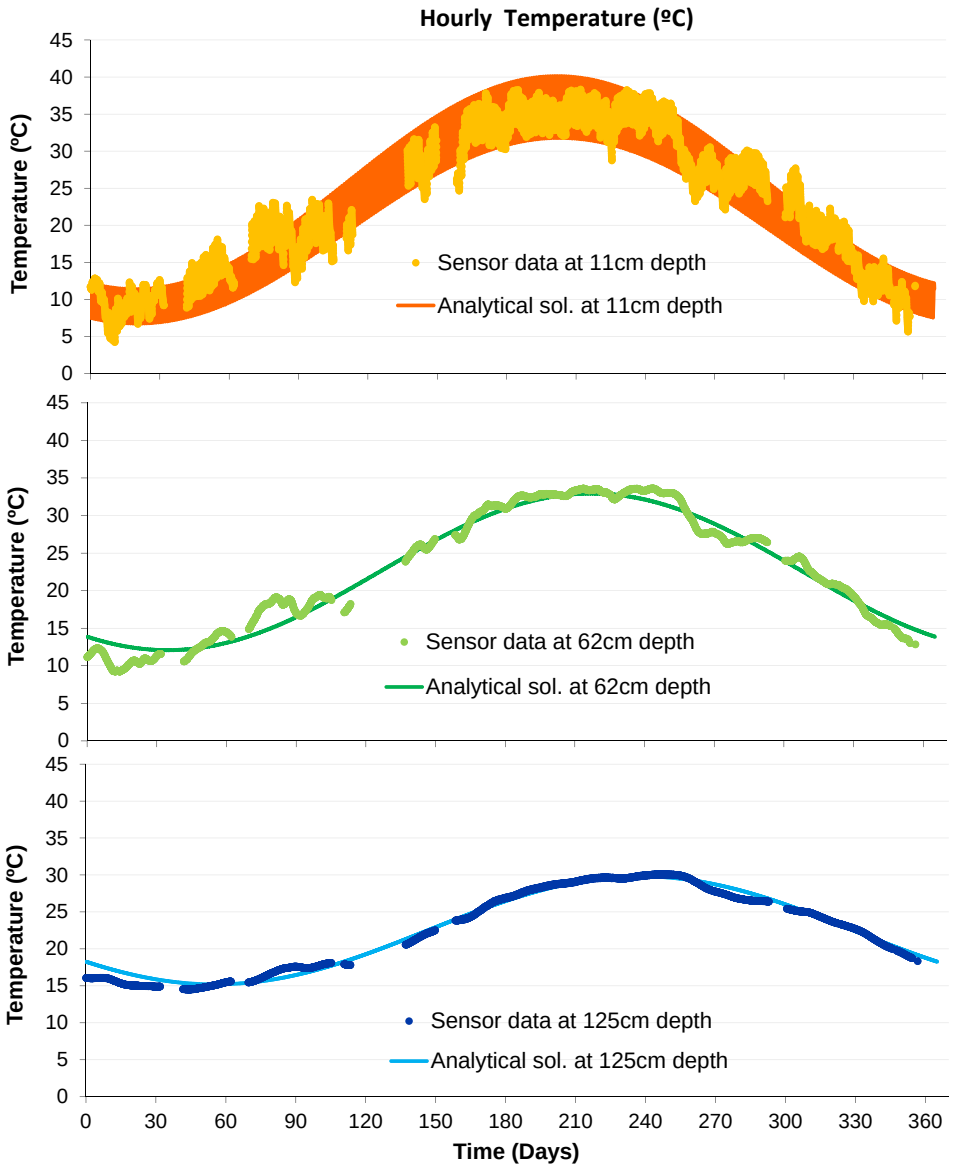

Figure 5.6: Hourly temperature registered by sensors versus hourly calculated (Eq. 5.5) along one year and for three different depths (11cm, 62cm and 125cm)

Instantaneous (hourly data, both from sensors and calculated by the analytical solution) and mean daily fluxes along the year, are shown in Figure 5.7.

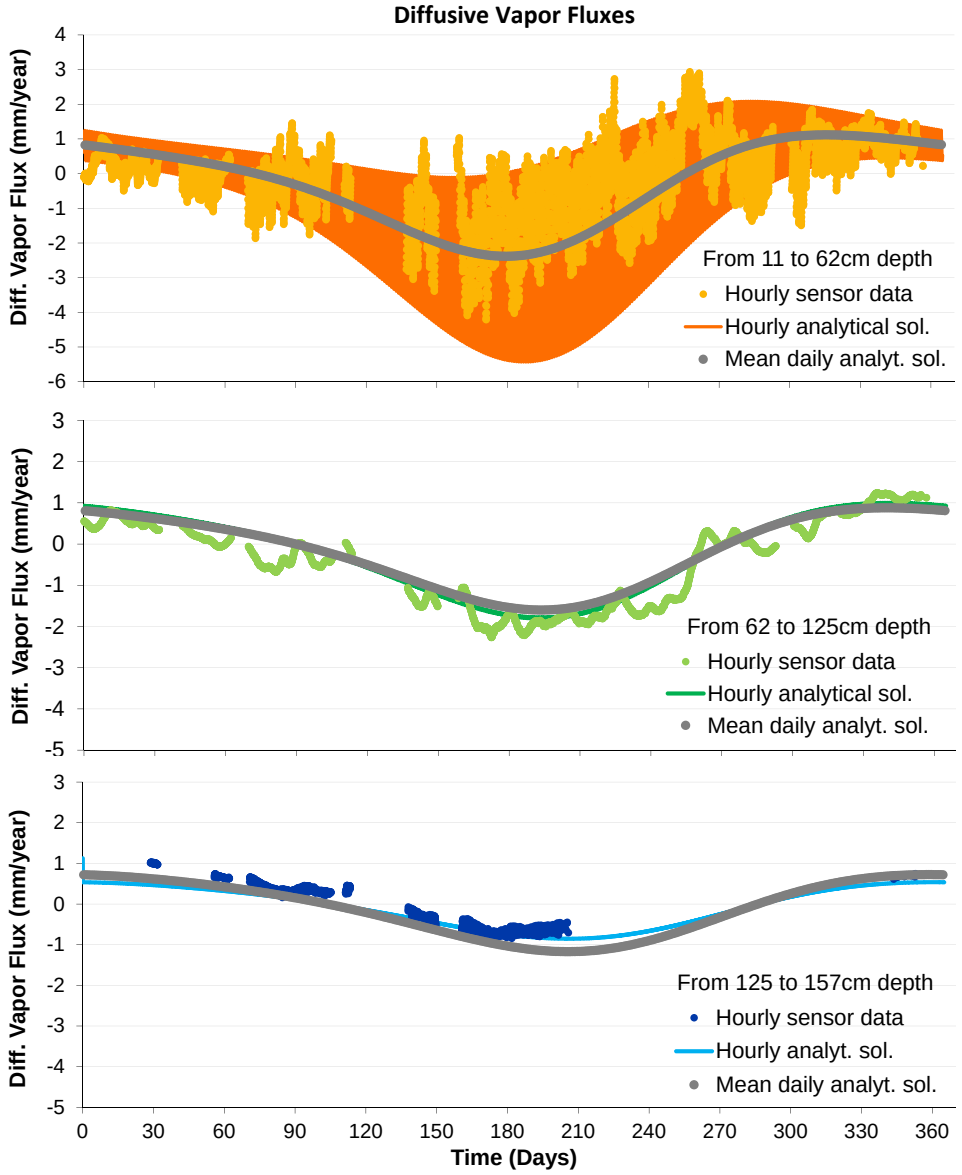

Figure 5.7: Hourly vapor fluxes between two depths calculated from sensor data and the analytical solution, versus mean daily fluxes (Eq. 5.14) along the year and for three different depths

It can be seen that peak fluxes are relatively large at shallow depths during the summer, but very small in winter. Contrary to the instantaneous fluxes, the mean daily flux is driven by yearly temperature fluctuations, even at shallow depths.

The total yearly fluxes at different depths and the logarithm of the mean yearly flux along the soil profile are shown in Figure 5.8.

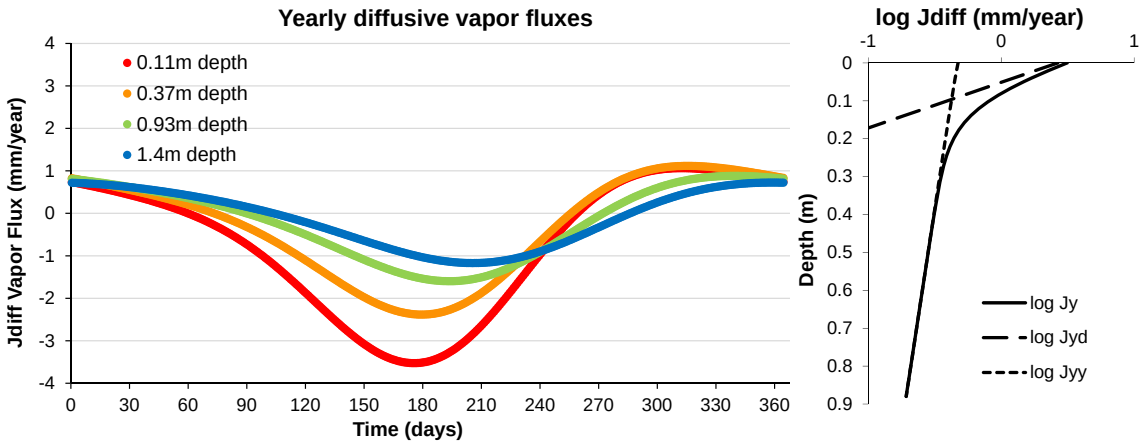

Figure 5.8: Total yearly fluxes at different depths, on the left, and the logarithm of the mean yearly flux along the soil profile, on the right. The daily ($J_y d$) and the yearly term ($J_y y$) are also shown in dashed lines.

The two terms that form the mean yearly flux, the daily term, $J_y d$ (eq. 5.15) and the yearly term, $J_y y$ (eq. 5.16), are also represented.

5.4 Discussion

RH ranges mostly between 98% and 100% (Fig.5.2). That is air within the soil is always close to water saturation. Thus, Pv will not be very sensitive to water content variations but only to temperature changes. Temperature evolution is conditioned by seasonal changes but also presents decrease in temperature, more evident close to the surface, that are caused by rainfall events. Precipitation increases soil water content, promoting evaporation (more water available together with a summer increase of energy) and cooling the soil. Hence, after a rainfall event, most of the energy is used for evaporation instead of heating up the soil. Atmospheric and soil temperature are similar during winter time, when evaporation is small, but this difference increases through the

year with a maximum in the summer. During the dry season, temperatures at 11 and 62cm depth are the highest of the soil profile. The same behavior is observed in Pv evolution.

Diffusive vapor fluxes are controlled by Pv gradients (Eq. 5.3 and 5.11), which in turn are governed by soil temperature gradients (Eq. 5.2). Temperature variations are larger close to the surface (Fig.5.2), causing large fluctuations in Pv gradients and vapor fluxes in the upper part of the soil (from the surface to 62cm depth).

Comparing Fig.5.4 and 5.5, it can be seen that during the winter vapor fluxes are one order of magnitude smaller, because both temperature gradients are lower due to lower temperatures and because the sensitivity of Pv_{sat} to temperature drops with it (eq. 5.11). The patterns of yearly fluctuations of vapor fluxes are reproduced at the daily scale, only at shallower depths. Vapor diffuses downwards during most of the day for the summer time while during winter time, upward fluxes are dominant. Rainfall events throughout the year cause a dop of Pv near the surface leading to peaks of ascending vapor fluxes.

The analytical model of eq. 5.15 and eq. 5.16 suggests that the mean annual vapor flux is downwards everywhere and reaches a value of 3 mm/year at the surface where daily temperature oscillations are the main driving force. This value decreases exponentially with a characteristic depth ($(2\alpha_d)^{?1}$) of about 5 cm. Below this depth vapor diffusion is controlled by annual oscillations and is much lower, further decreasing with a characteristic depth ($(2\alpha_d)^{?1}$) of about 1 m. Of course, one has to bear in mind that our analytical model assumes saturated vapor pressure, which may not be the case especially within the few centimeters near the surface, where there are no data available.

Calculations of mean annual vapor fluxes from data directly (Table 5.2) reveal some differences between the normal year of 2009 and the wet year of 2010. The mean vapor flux close to the surface (from 11 to 125cm) is higher in 2010 (-0.42mm/yr) than in 2009 (-0.15mm/yr), thus in a wetter year this downward vapor flux increases. If upward and downward fluxes are considered

separately, in 2010 downward vapor fluxes increase while upward fluxes change only slightly. Looking at maximum and minimum vapor fluxes (Table 5.3), it is clear that largest fluxes take place close to the surface and in 2010, and that the maximum downward fluxes are larger than the maximum upward fluxes. Therefore, the wetter the year the larger the downward vapor fluxes. As the advective heat flux is driven by vapor flux, it behaves likewise, carrying heat out of the soil in wet seasons and into it in dry seasons (Fig. 5.3). The conductive heat flux has the same direction as the advective flux and is much larger. So the total heat flux is upwards during winter and downwards during summer time.

The diffusive vapor fluxes resulting from the approximate analytical solution matches closely the ones calculated from the sensor measurements (Fig. 5.7). This suggests that the analytic solution proposed can be a useful tool to calculate vapor diffusive fluxes when only data from the soil surface is available.

5.5 Conclusions

Diffusive vapor fluxes are controlled by temperature gradients through the Pv gradients. As close to the surface temperature gradients change following daily oscillations, vapor fluxes in the upper part of the soil (a depth between 11 to 62cm) switch daily from downwards to upwards and vice versa. For summer time, vapor diffuses upwards during the morning and downwards during afternoon and night, while during winter time upward fluxes are dominant (only downwards for a few night hours). Below 62cm, vapor flows almost constantly upwards during wet and cold seasons and downwards during the hot and dry periods. Therefore, vapor fluxes vary daily in the upper part of the soil and seasonally deeper down.

Rainfall events have a cooling effect, decreasing the soil temperature, inverting the Pv gradient and leading to a larger and upward vapor fluxes. Nevertheless, precipitation is concentrated in

winter time when the vapor fluxes are one order of magnitude lower than in summer time and the larger amount of available water leads to a higher downward vapor fluxes. Therefore, these upward fluxes do not counteract the summer downward fluxes and the direction of the net annual vapor flux is downwards.

From the comparison of two different years with respect to precipitation, 2009 and 2010, the following conclusions can be drawn. The dry season is longer in 2009 than in 2010 which suggests that during a dry year downward vapor fluxes are higher than during a wet year, but surprisingly, in the upper part of the soil it is quite the opposite. That is because rainfall events increase soil water content, promoting evaporation and leading to a larger downward vapor fluxes. Thus, the magnitude of the downward fluxes is more relevant than the occurring time interval (duration of the dry season). Therefore, the downward diffusive vapor fluxes in a wetter year, are larger than in a dry year. Furthermore, an approximate analytical solution to calculate diffusive vapor fluxes at any depth, is presented.

What is clear is that vapor fluxes driven by temperature gradients, while quantitatively small, may still represent a significant source of water during summer for shallow roots. This may be especially important for plants, which may attract water from hot zones around the plant to the root zone, which is kept colder by the plant shadow.

Chapter 6

Field Data and Numerical Modeling of Water and Energy Balances for a Cover in a Semiarid Area

6.1 Introduction

Soil covers are used worldwide for long-term isolation of buried waste, ranging from municipal and industrial landfills to hazardous and radioactive waste disposal facilities (*Peng and Jiang*, 2009). Many different designs have been developed with the goal of protecting the underlying waste from infiltration and biointrusion. Water-balance covers, hydraulic barriers and capillary barrier covers have been tested in different climates (arid, semiarid, humid, cold, etc). As a result, an extensive list of weaknesses have been highlighted. Most common failures are due to biointrusion, desiccation cracks or precipitation rates exceeding the cover water retention capacity and/or its evapotranspiration rate (*Jessberger and Stone*, 1991; *Khire et al.*, 1994; *Smith et al.*, 1997; *Dwyer*, 1998; *Khire et al.*, 1999; *Albrecht and Benson*, 2001; *Albright and Benson*, 2003; *Dwyer*,

2003; *Albright et al.*, 2006; *Gee et al.*, 2006; *Abdolahzadeh et al.*, 2011).

To improve cover designs, it is essential to analyze and predict their performance. Arid and semiarid areas are commonly viewed as the most suitable for waste disposal despite the limited understanding of unsaturated flow processes and the technical limitations to measure low water fluxes (*Scanlon et al.*, 1997). Mathematical modeling is a useful tool to describe the mechanisms that control these water and energy fluxes and to evaluate the durability of the cover.
Many modeling studies have been conducted to covers design but few compared model results with field measurements (*Khire et al.*, 1999; *Scanlon et al.*, 2005; *Benson et al.*, 2004, 2005; *Ogorzalek et al.*, 2008; *Bohnhoff et al.*, 2009). One of the main problems in modeling unsaturated flow in landfill covers is inaccurate water balances caused by both over-predicted and unpredicted runoff fluxes (*Khire et al.*, 1999; *Benson et al.*, 2004, 2005; *Ogorzalek et al.*, 2008) and underestimation of infiltration (*Khire et al.*, 1997). Furthermore, many of these models use relevant input parameters like soil hydraulic properties taken from calibration (*Ogorzalek et al.*, 2008) or have been implemented using codes that do not simulate capillary barrier effects (*Albright et al.*, 2013).

Variations like climate, type of construction, layering and used soils require more study (*Bohnhoff et al.*, 2009). There is still a need to find the soil layer combination able to control infiltration, while preventing biointrusion in semiarid climates where precipitation occurs during low evaporation rate periods. Especially in dry zones, evaporation and heat and water transport have an important effect on each other. Therefore, the coupled interaction between unsaturated flows and evaporation must be included in the numerical simulations. With the aim of studying these processes, two pilot covers were built in a semiarid area where precipitation concentrates in winters. These covers combine water-balance and hydraulic barrier designs with a biointrusion and a capillary barrier. They were studied using the data recorded by a thorough monitoring system (volumetric water content, suction and temperature). The data showed the relevance of the capillary barrier formed by the first two layers. However, the deeper layers did not work as well as the top layers and some sensors did not work, so that the analysis was hindered by the scarcity of data.

In this work, a coupled nonisothermal multiphase flow model of a multilayer cover in a semiarid region is presented. Here, soil parameters measured at the laboratory and meteorological data registered at the site are used as input data. A two year period is simulated, atmospheric boundary conditions are applied at the surface and the dip and strike of the layers are accounted for in the calculation of the amount of rain and the incoming atmospheric short wave radiation. Even though the model is one dimensional, lateral drainage is taken into account through a flux boundary condition all along the cover width. Our goal, is 1) to test whether the interaction of evaporation, heat and water flow can satisfactorily describe the performance of the cover and 2) to analyze the behavior of and quantify the water and energy fluxes in the different hydraulic barriers separately and to test their performance in minimizing infiltration.

6.2 Pilot Cover and Conceptual Model

Two pilot waste covers, Test I and Test II, have been built and heavily instrumented at El Cabril (Cordoba, southern Spain). Their performance was monitored during two years by recording suction, temperature and water content through the whole soil profile. Both covers consist of an evapotranspiration layer, a biointrusion barrier, which also acts a a capillary barrier, and an infiltration barrier. Cover and monitoring system designs and results are described in Chapter 4 and a detailed analysis of the diffusive vapor fluxes behavior has been presented in Chapter 5.

The conceptual model emerging from the previous analysis of the pilot cover is based on the relevance of the capillary barrier effect coupled with the upper layers retention and evapotranspiration capacity. The two top layers (topsoil and soil) retain the infiltrated rain water to be evapotranspired. The second layer (soil) together with the third layer (coarse layer of sand in Test I, and cobbles in Test II) form the first capillary barrier. In the soil, water not only accumulates but it is also diverted laterally downslope while keeping the underlying coarse layer dry. This capillary barrier worked well the first year, but failed after an anomalously wet second year in Test I. In Test

II, it failed both years leading to larger infiltration. This shows the relevance of the first capillary barrier to minimize percolation. For the deeper layers, data is scarcer, making the comparison between the clay layers of the two tests more difficult.

6.3 Processes and Governing Equations

The system is governed by thermohydraulic processes. Therefore, coupled water flow and heat transport must be simulated. Under natural weather conditions, the interaction soil-atmosphere must be included as well and accounted for in both water and energy balances. Natural oscillations of the atmospheric conditions will cause large and rapid changes of temperature, water content and suction in the upper layers. These changes as well as those of thermal conductivity and permeability should be simulated. As lateral flow can form a substantial part of the water balance (*Hopp et al.*, 2011) it must also be included in the numerical model.

6.3.1 Thermohydraulic Processes

The thermohydraulic model focuses on the mass balance of water (liquid water and vapor) and air (dissolved in water and in the gas phase) in terms of pressure, and the energy balance in terms of temperature. The equations of water and air mass balance are:

$$\frac{\partial}{\partial t}(\omega_l^w \rho_l S_l \phi + \omega_g^w \rho_g S_g \phi) + \nabla \cdot (\mathbf{j}_l^w + \mathbf{j}_g^w) = f^w \tag{6.1}$$

$$\frac{\partial}{\partial t}(\omega_l^a \rho_l S_l \phi + \omega_g^a \rho_g S_g \phi) + \nabla \cdot (\mathbf{j}_l^a + \mathbf{j}_g^a) = f^a \tag{6.2}$$

where subscripts l and g refer to liquid and gas and superscript w and a refer to water and air. ω is the mass fraction (kg kg $^{-1}$) of a component in a phase, ρ is the density (kg m^{-3}) of a phase, S is the hydraulic saturation (m^3 m^{-3}), ϕ is the porosity (m^3 m^{-3}), $\mathbf{j}$ (kg m^{-2} s^{-1}) is the total flux

(advective, diffusive and dispersive) and f is an external source/sink term (kg m^{-3} s^{-1}). Note that the first two terms in the equations represent the change in the mass of water (Eq. 1) or air (Eq. 2) in the liquid and gas phase respectively and the third and fourth terms represent the fluxes of water (Eq. 1) or air (Eq. 2) in liquid and gas phase, respectively. The energy mass balance is written as:

$$\frac{\partial}{\partial t}(E_s\rho_s(1-\phi) + E_l\rho_l S_l\phi + E_g\rho_g S_g\phi) + \nabla\cdot(\mathbf{i}_c + \mathbf{j}_{El} + \mathbf{j}_{Eg}) = f^Q \tag{6.3}$$

where E is the specific internal energy (Jkg^{-1}), $\mathbf{i}_c$ is the energy flux (J m^{-2} s^{-1}) due to conduction, the other fluxes ($\mathbf{j}_{El}$, $\mathbf{j}_{Eg}$) are advective fluxes of energy (J m^{-2} s^{-1}) driven by fluid (l, liquid or g, gas) flow, and f^Q is an internal/external heat source (J m^{-3} s^{-1}). A state variable is associated with each mass balance: liquid pressure (P_l), gas pressure (P_g) and temperature (T). Constitutive laws are used to express the mass balance equations as a function of the state variables. Table 6.1 displays the most important constituve laws. For a complete list we refer to *Olivella et al.* (1994, 1996c).

Oven dry conditions are simulated by modifying the Van Genuchten retention curve and relative permeability functions that were presented in Chapter 3. Therefore, liquid fluxes are assumed zero ($k_{rl} = 0$) when water saturation falls below the residual saturation, S^0 but saturation may keep decreasing by evaporation. Vapor diffusion enhancement, tortuosity and constrictivity are not simulated ($\tau = 1$ in the diffusion coefficient equation in table 6.1).

Table 6.1: Constitutive laws, parameters and values used in the numerical model.

Constitutive laws		Parameters & values
Water saturation for ret. curve in modified van Genuchten model	$S_l = S_i + (1 - S_i)S_e$ $S_e = \left(1 + (P_c/P_0)^{\frac{1}{1-\lambda}}\right)^{-\lambda}$ $S_i = \alpha S^0 \ln(P_c^{dry}/P_c)$	$S^0 = 0.1$
Relative permeability function (for a new ret. curve)	$K_{rl} = 0, \quad \text{if } S_l \leq S^0$ $K_{rl} = \sqrt{S_{ep}}\left(1 - (1 - S_{ep}^{1/\lambda})^{\lambda}\right)^2, \text{ if } S_l > S^0$ $S_{ep} = (S_l - S^0)/(1 - S^0)$	
Darcy's Law	$q_\alpha = -\frac{k_i k_{r\alpha}}{\mu_\alpha}(\nabla P_\alpha - \rho_\alpha g)$	
Diffusive flux of vapor (Fick's Law)	$i_\alpha = -(\tau\phi\rho_\alpha S_g D_m \mathbf{I})\nabla\omega$ $D_m = \tau D\left(\frac{(273.15+T)^n}{P_g}\right)$	$D = 5.9 \cdot 10^{-6} m^2 s^{-1} K^{-n} Pa^a$ $\tau = 1, n = 2.3$
Conductive flux of heat (Fourier's Law)	$i_c = -\lambda\nabla T$ $\lambda_{dry} = (1 - \phi)^n \lambda_{solid} + \phi^n \lambda_{gas}$ $\lambda_{sat} = (1 - \phi)^n \lambda_{solid} + \phi^n \lambda_{liq}$ $\lambda = \sqrt{S_l}\lambda_{sat} + \left(1 - \sqrt{S_l}\right)\lambda_{dry}$	$\lambda_{sol} = 2 W m^{-1} K^{-1}, n = 2$ $\lambda_{gas} = 0.024 W m^{-1} K^{-1b}$ $\lambda_{liq} = 0.6 W m^{-1} K^{-1b}$
Psychrometric Law	$P_v = 136075\ exp\left(\frac{-5239.7}{273.15+T}\right)$	MPa

Where q_α=flow rate (ms^{-1}) of phase α, k=intrinsic (k_i) and relative ($k_{r\alpha}$) permeab., μ_α=viscosity (Pa s), ρ_α=density (kgm^{-3}), g=gravity , ϕ=porosity, i_α=vapor diffusive flux (Js^{-1}), S=liquid (S_l) and gas (S_g) saturation, w_α=water mass fraction in gas phase (kg of vapour per m^3 gas phase), D_m=diffusion coeff. ($m^2 s^{-1} K^{n-1}$), i_c=heat conductive flux ($Jm^{-2}s^{-1}$), λ=thermal conductivity (WmK^{-1}) and P_v=vapor pressure (Pa).
[a] From *Philip and de Vries* (1957). [b] From *Campbell and Norman* (1998).

6.3.2 Boundary Conditions

Atmospheric Boundary Conditions

The atmospheric boundary conditions model the soil-atmosphere interaction for the three components (water, air and energy), which are a function of their state variables (P_l, P_g and T), and meteorological data (temperature, relative humidity, wind velocity, radiation, precipitation, etc).

The dip and strike of the layers are included to calculate the amount of rain and the incoming direct solar radiation. The resulting water and energy fluxes are included in the water and energy mass balances through the source/sink term. All the equations used are displayed in Appendix A.

Lateral Flow Sink Term

The lateral drainage sink term (*Carrera et al.*, 1991; *Galarza et al.*, 2001) has been added to the existing code to account for the water flow diverted laterally through the soil. Neglecting lateral variations in state variables, we can simulate a two dimensional problem using a one dimension model. This sink term (q_l) depends on the soil permeability (K_{hid}), the slope (α) and the distance to the ridge of the cover (L). The amount of energy carried by this water flux is taken into account in the energy balance. Lateral water flow is assumed to increase per unit of longitude and vertical inflow and outflow (from the layer above and to the underlying one), are considered constant through the longitudinal section.

$$q_l = \frac{K_{hid} \cdot \alpha}{L/2} \qquad K_{hid} = k_{int} \cdot k_{rel} \cdot \frac{\rho g}{\mu} \tag{6.4}$$

Drain Boundary Condition

A drain boundary condition is used at the base of the cover to avoid liquid water entry and to enable liquid water outflow (j_l) when P_L overcomes P_l^0:

$$\begin{cases} j_l = \gamma_l \left(P_l^0 - P_l\right), & if P_l > P_l^0 \\ j_l = 0, & if P_l \leq P_l^0 \end{cases}$$

Gas inflow (j_g) is given by $j_g = \gamma_g \left(P_g^0 - P_g\right)$. Where γ was given a sufficiently high value to practically fix P to P^0. Values of P_l^0= P_g^0=0.101325 MPa are prescribed.

6.4 Numerical Model

The model is a 1D column 2.89 m long with 46 elements and 47 nodes which represents one of the covers, Test II. The distance between nodes is not constant. The grid is refined near the limits of the layers and close to the surface. Seven layers are represented with six different materials. Material properties are displayed in table 6.2. The topsoil, the soil and the clay values were obtained at the laboratory by *Villar* (2011); *Villar and Fernández* (2011). The topsoil intrinsic permeability, was raised 2 orders of magnitude with respect to the laboratory results to increase water entry through the surface. Values taken from literature are used for cobble, sand and gravel layers. Note that the modified retention and permeability curves are used for the first layer (topsoil), and the conventional *van Genuchten* (1980) model is used for the rest of the materials. The boundary conditions (BC) are: 1) Atmospheric BC at the top, with temperature, relative humidity, solar radiation, precipitation and wind velocity registered by the meteorological station at the site, and the dip (40%) and strike (60°SE) of the cover also included; 2) the drain BC at the bottom; and 3) the lateral flow all along the cover profile, with a 40% slope to simulate the slope zone of Test II. The initial temperature is 20°C for all the nodes, P_g = 0.1MPa and P_l = 0.02 (approximate value registered by sensors at the upper layers).

Table 6.2: Parameters used in the numerical model for the retention curve, intrinsic permeability and porosity of the different materials.

		Topsoil	Soil	Cobble&Gravel	Sand	Clay
VG retention curve	λ:	0.2	0.22	0.75	0.5	0.2
	P_0[MPa]:	0.13	0.16	0.1	0.2	0.09
VG modified retention curve		P_c^{dry} =650MPa α = 0.1				
Intrinsic permeability	[m^2]	$1\cdot10^{-13}$	$5.6\cdot10^{-16}$	$1\cdot10^{-12}$	$1\cdot10^{-13}$	$1\cdot10^{-17}$
Porosity		0.32	0.28	0.32	0.35	0.32

Note that for the van Genuchten (VG) modified retention curve, two extra parameters are used in the upper layer (topsoil).

Numerical simulations were carried out using the code CODE_BRIGHT (*Olivella et al.*, 1996c), a finite element code that couples water flow and energy transport in a multiphase approach. The code acknowledges evaporation-condensation and its effect on the energy balance. The code also simulates soil-atmosphere interaction and thermohydraulic properties (such as thermal conductivity and permeability) that depend on water content.

6.5 Results and Discussion

Figure 6.1 displays the evolution of daily mean temperatures, during two years, computed at six different depths along with data recorded by sensors at Test II. The six plots illustrate the typical seasonal fluctuations with decreasing amplitude and delayed peaks at increasing depth. The largest fluctuations and highest temperatures occur in the topsoil layer and decrease with depth. The simulations reproduce the seasonal behavior of the temperatures at all depths and also the large fluctuations in the first layer. A difference between the calculated and the measured temperatures is observed during the summer of 2010, when temperatures are slightly underestimated. The underestimation of temperature the second year is somewhat puzzling, and even more, is that this underestimation grows with depth. This is surprising because the peak temperatures were well captured by the model during the first year. This second year was wetter and vegetation had grown on the cover. If anything, both factor should have contributed to reduce, rather than increase temperatures. It is clear that something is missing in the model. To be able to reproduce the soil temperatures, the wind velocity at the cover is assumed to be half of that registered by the meteorological station. This supposition is reasonable because the station is not located at the cover side but at a more exposed spot. To account for the presence of the vegetation in the cover surface during the second year, the roughness length (parameter related to the horizontal wind speed near the ground) in the evaporation and sensible heat calculations was also modified.

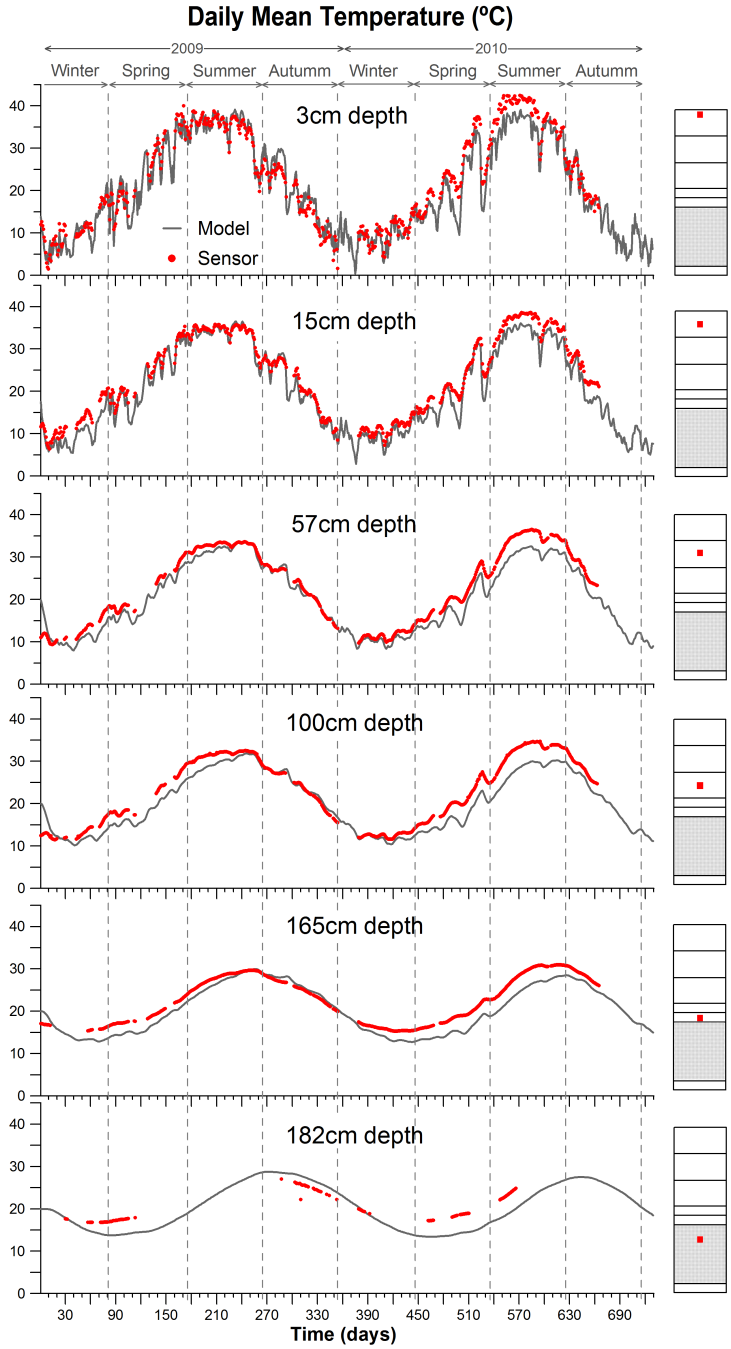

Figure 6.1: Daily mean evolution of the temperatures computed along with the data registered by sensors during two years. The layer schema on the right of each plot, shows the location of the measured-simulated depth in the cover. In red dots, sensors data, and in gray lines, the model.

Figure 6.2 displays the two year evolution of daily mean suctions computed at six different depths along with recorded data. Daily precipitation is shown in the upper part of the first plot (with a descending axis). To capture the maximum information of the suction evolution in the upper layer (where the fluctuations are largest), data from two different sensors is shown in the first two plots. For the the remaining dephts, data for one sensor are displayed along the computed suction.

The model reproduces the biggest oscillations and highest values during dry periods and abrupt drops during wet periods for the first layer (two first plots). The computed values match both overall values and oscillations of suction recorded by the sensors. In the soil layer (third plot) less recorded data are available for comparison. Nevertheless, the model appears to reproduce the values and the tendency of the data during dry periods. The differences between the model and the sensors start at the cobble layer (fourth plot).

The model reproduces the first decrease in suction due to the break of the capillary barrier, but then remains stable for the rest of the simulated period. Looking at the deeper layers (fifth and sixth plots) the computed suctions stay constant for the whole two years, and consequently no water entry is simulated by the model after 100cm depth. Therefore, the model simulates a perfect capillary barrier, which contradicts observations. We attribute this problem to the nature of water to flow through the cobble layer. As discussed in Chapter 4, water crosses this layer through fingers, a mechanism that is not included in our numerical simulations.

Figure 6.3 displays the two year evolution of the energy fluxes at the soil surface. The energy flux is divided into sensible heat, latent heat and net radiation (R_n). Their hourly calculated values together with the direct solar radiation are shown.

The net radiation is calculated as

$$R_n = (1 - A_l)R_g + \epsilon R_a - \epsilon\sigma T^4 \tag{6.5}$$

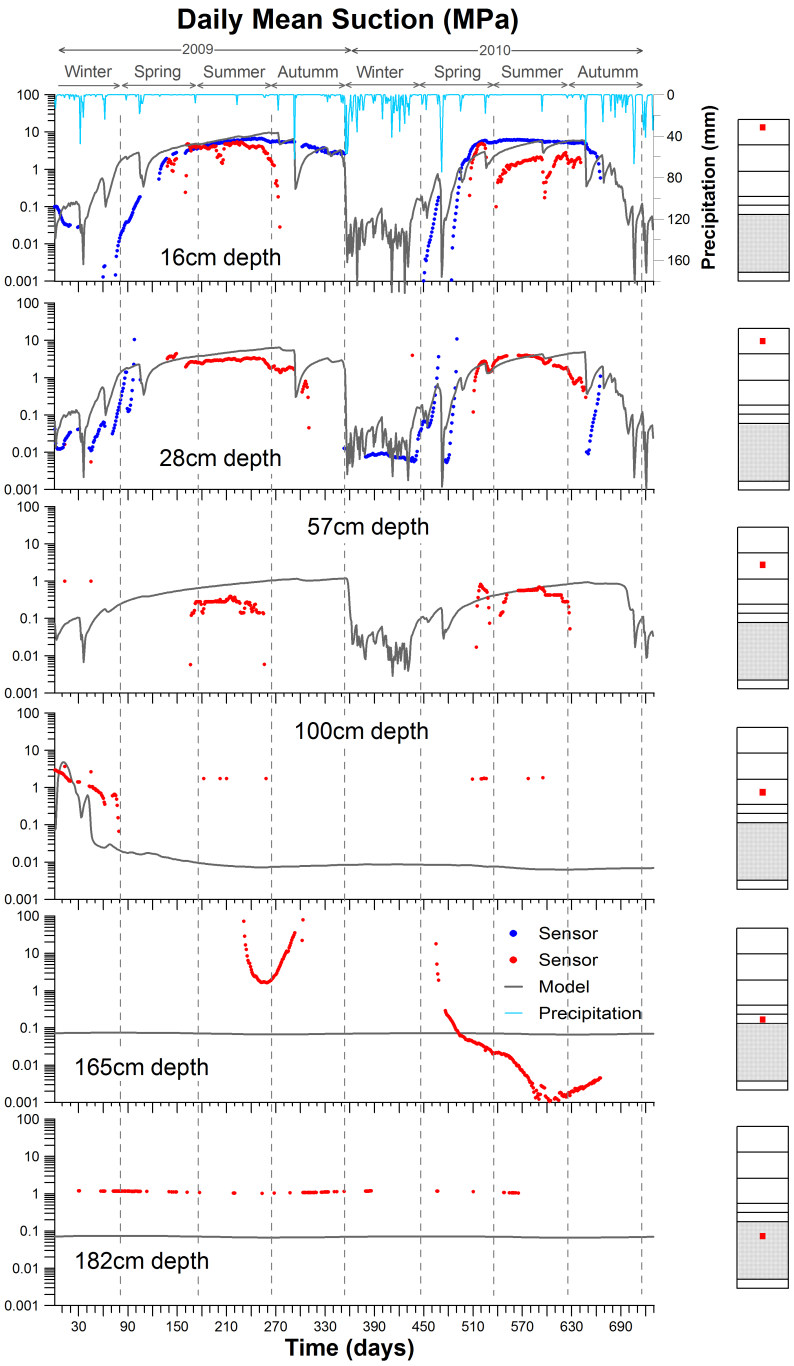

Figure 6.2: Daily mean evolution of the computed suctions along with the sensors data during two years. The layer schema on the right, shows the location in the cover. In red and blue dots, sensors data, in gray and blue lines, the numerical simulations and the precipitation respectively.

Where A_l is the albedo, R_g is the direct solar short wave radiation (recorded by the meteorological station), R_a is the diffuse atmospheric radiation, ϵ is the emissivity and σ is the Stefan-Boltzman constant ($5.67 \cdot 10^{-8} Js^{-1}m^{-2}K^{-4}$). The latent heat is the amount of energy required to evaporate liquid water, and the sensible heat is the flux of energy between the surface and the atmosphere by the combined effect of thermal conduction and thermal convection. The equations used to calculate both fluxes are given in Appendix A.

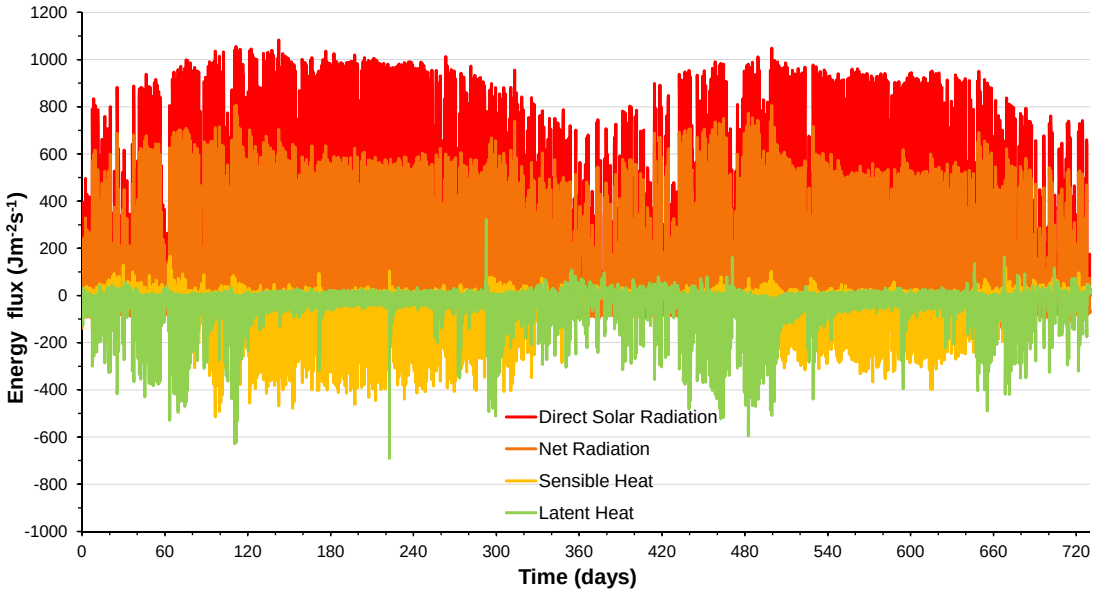

Figure 6.3: Two year evolution of the energy fluxes at the soil surface. Hourly calculated values of solar radiation (R_g), net radiation (R_n), sensible heat and latent heat. In positive, the fluxes entering into the soil and in negative, the outflows that go from the soil surface to the atmosphere.

The energy fluxes evolution (Fig. 6.3) shows the fluctuations of the incoming radiation, larger during the summers, and how it is divided into sensible and latent heat depending on the precipitation. During wet periods, energy is mostly spent evaporating the infiltrated water (negative fluxes) but there are also some positive fluxes that indicate that condensation is taking place at the soil surface. During the summer, when the soil is dry, most of the incoming energy is spent in heating the soil. Therefore, the soil temperature is larger than the atmospheric. This causes a sensible heat flux from the soil to the atmosphere (negative). Small positive fluxes of sensible energy are also displayed for the periods where the soil is cooler than the air.

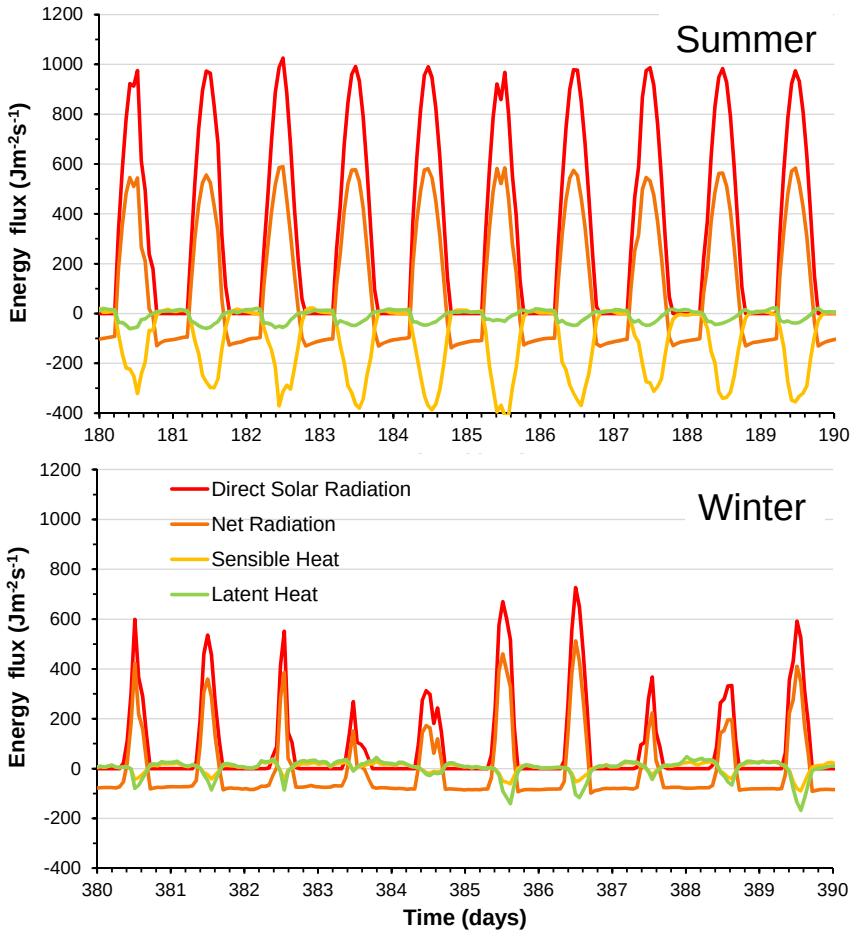

Figure 6.4: Comparison of energy fluxes evolution at the soil surface for some summer and winter days. Hourly calculated values of solar radiation (R_g), net radiation (R_n), sensible heat and latent heat. In positive, the fluxes entering into the soil and in negative, the outflows to the atmosphere.

Figure 6.4 shows the detail of these energy fluxes for some summer and winter days. The summer plot shows that during the day, radiation is positive (input), while sensible heat is negative. All input fluxes are greatly reduced at night. During the winter, both day and night fluxes are much smaller than in summer time. During the day, the negative sensible heat fluxes are small and during the night the fluxes are positive and sometimes compensate the day ones. Latent heat flux is small during the summer, because the soil is dry, but there are still negative fluxes during the day and no or small positive fluxes during the night. This suggests that there is condensation occurring at the soil surface during the night. The same behavior is observed for winter, but with larger negative latent heat fluxes due to some small rainfall events.

Figure 6.5 displays the two year evolution of water fluxes at the soil surface. The hourly calculated values of rain, infiltration (water available for infiltration, that is rainfall minus runoff) and evaporation, are displayed. The rain and the infiltration (always positive fluxes) are concentrated mainly during winter and spring. In the precipitation events occurring during the summer there is no runoff, everything infiltrates, while during the wet season there is a fraction of the rain that does not enter into the soil. Evaporation (negative fluxes) takes place almost everyday but fluxes become large after rainfall events.

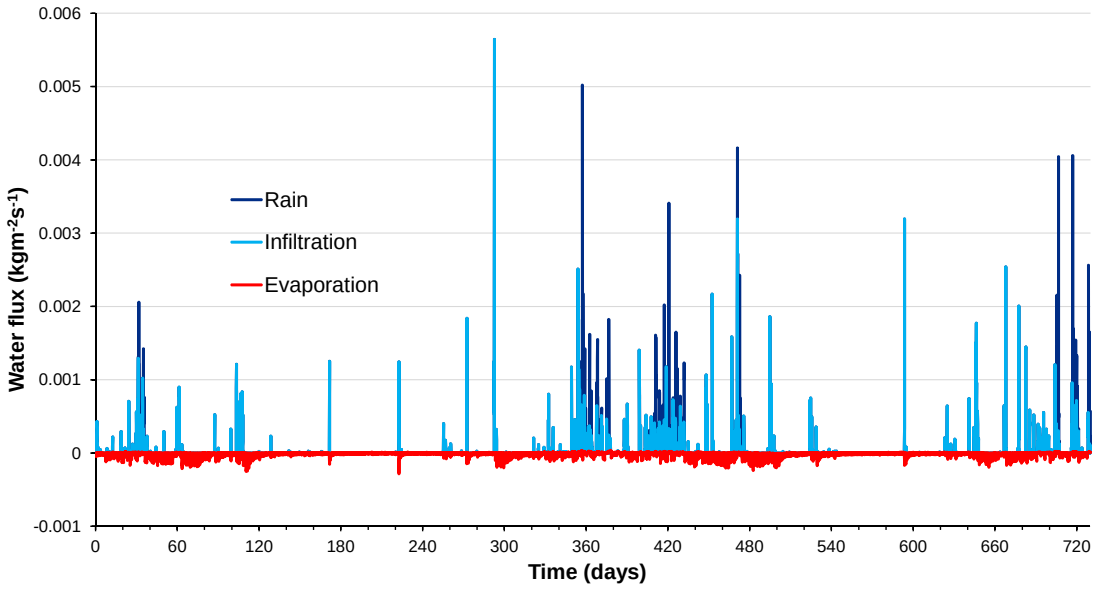

Figure 6.5: Two year evolution of water fluxes at the soil surface. Hourly calculated values of rain, infiltration (rain + runoff) and evaporation. In positive, the fluxes entering into the soil and in negative, the outflows that go from the soil surface to the atmosphere.

Figure 6.6 displays the detail of these water fluxes for some winter days. Different kinds of responses are taking place. With the first rain (day 24), all the precipitation infiltrates (no runoff) and the day after, the evaporation is bigger than it was before the rain. Around days 31 and 32, a bigger event occurs where the first rain infiltrates completely. After a few hours, the soil is saturated and runoff starts. At the end of the event, almost all the rain runs off. The same occurs for the precipitation on day 35. Evaporation presents a peak everyday (when the incoming radiation is maximum) and it is larger after the rains decreasing slowly the days after.

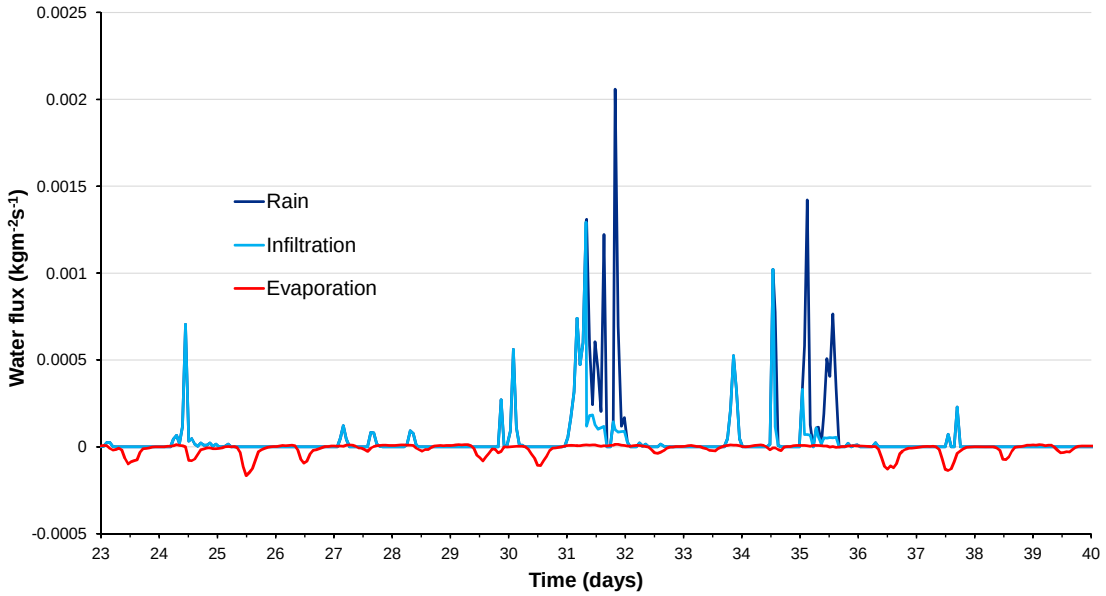

Figure 6.6: Detail of the evolution of water fluxes at the soil surface for some winter days. Hourly calculated values of rain, infiltration (rain + runoff) and evaporation. In positive, the fluxes entering into the soil and in negative, the outflows.

The energy balance in the cover is presented in Table 6.3. The integrated annual fluxes of direct solar radiation, net radiation, sensible heat flux, latent heat flux and the change in energy storage are displayed separately for the two years of the study. The radiation entering through the soil surface was larger the first year, as was the net radiation, because 2010 was a really wet year whith less insolation hours. The total sensible heat loss was also bigger in 2009. On the other hand, the latent heat flux, promoted by the availability of water, was larger in 2010, but not enough to counteract the loss of heat due the sensible heat in 2009. As a result, the cover lost heat during 2009 and gained it in 2010.

Table 6.3: 2009 and 2010 energy balance. Integrated annual fluxes of the direct solar radiation, net radiation, sensible heat flux, latent heat flux and the change in energy storage. Positive fluxes for the incoming fluxes and negative for the outflows.

Energy Bal. [kg/m^2]	Solar Rad.	Net Rad.	Sensible Heat	Latent Heat	Storage
2009	$7 \cdot 10^9$	$2.4 \cdot 10^9$	$-1.6 \cdot 10^9$	$-9 \cdot 10^8$	$-8 \cdot 10^7$
2010	$6 \cdot 10^9$	$1.8 \cdot 10^9$	$-7.7 \cdot 10^8$	$-1 \cdot 10^9$	$2.7 \cdot 10^6$

The cover water balance is presented in Table 6.4. The integrated annual fluxes of infiltration, evaporation, the drain flux (at the base of the cover), the lateral water flux and the change in water storage are displayed separately for the two years of the study. As we mentioned before, 2010 was an anomalously wet year, where precipitation was double that of 2009. Therefore, both infiltration and evaporation were largest. Even though infiltration was larger in 2010 than in 2009, the lateral flow ended up smaller. There is no water flow at the base of the cover for neither year and the annual change in water storage was positive for both, and largest in 2010.

Table 6.4: 2009 and 2010 water balance. Integrated annual fluxes of infiltration, evaporation, drain flux (at the base of the cover), lateral water flux and change in water storage. Positive fluxes for the incoming fluxes and negative for the outflows.

Water Bal. [J/m^2]	Rain	Infiltration	Evaporation	Lateral Flow	Drain Flow	Storage
2009	591	417	-360	-28	0	29
2010	1185	647	-412	-19	0	215

6.6 Conclusions

The model is able to closely reproduce the observed temperatures in the whole cover and the suction in the upper layers of the cover. Most model parameters were measured and some derived from the literature (see Tables 6.1 and 6.2). The measured parameters that were changed are the topsoil intrinsic permeability and the wind velocity. The qualitative good match between sensors data and computed values in the upper layers validates the model for this portion of the cover and allows us to analyze and quantify the simulated processes. These confirm the previous hypothesis (Chapter 4) of the first layers minimizing percolation through the cover. The following conclusions can be derived from the calibrated model:

- The top layers are highly effective in minimizing percolation. The first two layers (topsoil and soil) retain the infiltrated water during rainfall periods until it is evaporated during dry

periods.

- The second layer (soil) and the third one (cobble layer) are acting as a capillary barrier almost hindering all infiltration through the underlying materials.

- The model does not reproduce the water flux through the cobble layer because water crosses this layer through fingers, a mechanism that is not included in our numerical simulations.

- During wet periods, most incoming energy is converted into latent heat (by evaporating the infiltrated water) while it is transformed to sensible heat which mostly flows from the surface to the atmosphere in the dry periods.

- Latent heat is negative during the day but also displays small positive fluxes during the night which suggests that condensation is taking place at the soil surface.

- The increase in precipitation (rain in 2010 was double that of 2009) causes infiltration to rise. At the same time, both runoff and evaporation also increase to balance infiltration, resulting in a lower lateral drainage than in 2009. Therefore, more precipitation does not imply more lateral drainage.

- In the summer, the rains do not cause runoff. During the wet season, rain infiltrates completely during the first hours. If the rain continues, the soil saturates, runoff starts and at the end of the event, almost all rain becomes runoff.

- The cover is losing heat during 2009 and gaining slightly during 2010. The soil water content in the cover increases during both years.

In summary, our model supports the previous interpretation made from the field data and allows the detailed study of water and energy fluxes close to the soil surface. The upper layers performance is optimal, minimizing infiltration even during a year where precipitation is double the annual mean. Nevertheless, to be able to study the behavior of the lower layers and to quantify

the infiltration that reaches the base of the cover, the simulation of preferential flow (*Nimmo*, 2012) through the soil is needed.

Chapter 7

Conclusions

The objective of this thesis has been to gain understanding in evaporation and water and energy transfer mechanisms in dry soils. The main results we have found are summarized in this concluding chapter.

Evaporation from a salty soil generates salt accumulation near the surface with the subsequent deterioration of the soil quality. Salinization mechanisms are poorly understood despite their global impact. The interaction between the controlling processes is studied by an open soil column experiment. Results show that a water separation process occurs in the unsaturated zone of the soil. Above the evaporation front, which we found is very narrow, the soil contains high salt concentrations due the solutes transported by the upward liquid flux and concentrated by evaporation. Below, concentrations lower than the initial one are found. From the evaporation front, vapor flows not only upwards because of capillarity gradients but also downwards due to temperature gradients. Condensation of this downward vapor flux explains the dilution below the evaporation front. This mechanism dilutes water a few centimeters below the surface improving soil conditions and providing an area where where root plants could live.

Mathematical modeling of nonisothermal multiphase flow and reactive transport during the

column experiment allows quantifying the processes. Evaporation causes vapor pressure to increase at the evaporation front causing vapor to flow upwards and downwards. Downwards flux increases over time and at the end of the experiment is half that of the upward flux. The evaporation front is very narrow, most evaporation is concentrated in less than 1cm, and some evaporation occurs above the front, while condensation starts immediately below. Condensation of the downward vapor flux dilutes the solution with the result that salinity drops below the initial value. Heat flows downwards from the surface to the bottom of the column mainly by conduction. Still, upwards advection of latent heat almost compensates downwards conduction above the evaporation front. Therefore, advection of latent heat is also relevant. In summary, our model supports the traditional division of soil, by an evaporation front, into a dry region and a moist region. Vapor diffusion is the only relevant water flow mechanism in the upper region. This view may suffice for evaluating evaporation rates and water mass balances. However, assessing salt processes requires acknowledging that not only liquid water but also vapor diffusion occur below the evaporation front.

Surface soil covers are used worldwide to isolate solid waste. Their main goal is to protect the underlying waste from infiltration during long periods of time by promoting surface runoff and lateral drainage and by hindering biointrusion. Conventional designs based only on water balance methods or on capillary barriers, usually fail due to biointrusion or desiccation cracks. Two cover designs were built up, both consisting of an evapotranspiration layer, a biointrusion barrier and an infiltration barrier. The performance of both covers is analyzed for two years (an average year, 2009, and an anomalously wet year, 2010) by a thorough monitoring system. The first two layers (topsoil and soil) display the largest oscillations in temperature, soil water content and suction. The effect of the precipitation events (suction decrease and water content increase) is quite apparent in these layers. The second and third layer (sand in Test I and pebble in Test II) form the first capillary barrier. Water is diverted laterally above this layer proportionally to its slope. As a result, water content decreases fast after rainfall events at the sloping portion of the cover (section 3). The capillary barrier failed both years in Test II and failed at the end of the wet

year in Test I. These data illustrate the relevance of this first capillary barrier and highlights the value of the natural filter layers (only present in Test I, a geotextile layer was expected to provide filtering in Test II) to minimize percolation during the first year. For the deeper layers, data is scarcer, hindering the infiltration analysis and making unfeasible the comparison between the two clay capillary barriers. Furthermore, the water flows from the clay to the underlying sand not as an homogeneous front but via preferential paths (*Nimmo*, 2012), which makes it more difficult to the monitoring system to measure it. The second year, water infiltrates into the base of both covers but without reaching saturation. It is clear that the infiltration barrier was not sufficient. To improve its function in future designs, we suggest increasing the retention capacity of the sand layers, including the filter layers and facilitating lateral drainage by increasing the slope in the top area.

Vapor fluxes play an important role in unsaturated soils. When the soil is dry, there is little liquid recharge and temperature and vapor pressure gradients are large. As a result, vapor fluxes become relevant. Nevertheless, their high spatial and temporal variability, the low magnitude of their fluxes and the limitations of the measurement techniques complicates their study. We have studied the daily and annual variations of vapor fluxes using the data from the cover field-scale experiment. Diffusive vapor fluxes are controlled by temperature gradients because the air in the soil is close to saturation (relative humidity of 100%), so that vapor pressure is a function of temperature. However, the non-linear dependence of saturation vapor pressure on temperature causes the vapor pressure to increase with temperature. As a result even if the temperature gradients reverse so that the mean gradient is zero, there will be a net vapor flux from the zone of highest temperature fluctuations. Close to the surface vapor fluxes follow daily oscillations of temperature, switching direction with a daily frequency and a depth dependent lag. At the studied depths, during the summer, vapor diffuses upwards during the morning and downwards during afternoon and night, while during winter time upward fluxes are dominant (only downwards for a few night hours). Deeper into the soil, vapor fluxes vary seasonally, flowing almost constantly upwards during wet and cold seasons and downwards during the hot and dry periods. Rainfall events have a

cooling effect, decreasing soil temperature, inverting the vapor pressure gradient and leading to a larger and upward vapor fluxes. Nevertheless, precipitation is concentrated in winter time where the magnitude of the fluxes is one order of magnitude smaller than in summer time. Therefore, these upward fluxes do not counteract the summer downward fluxes and the direction of the net annual vapor flux is downwards. Furthermore, it has been observed that the downward diffusive vapor fluxes in a wetter year, are larger than in a dry year. What is clear is that vapor fluxes driven by temperature gradients, while quantitatively small, may still represent a significant source of water during summer for shallow roots. Plants may attract water from hot zones around the plant to the root zone, which is kept colder by the plant shadow and by transpiration.

Mathematical modeling is also used to study coupled water and energy fluxes in the soil cover and to complete the gaps left by the monitoring system. As this is a soil under natural weather conditions our numerical model includes a top atmospheric boundary condition. Meteorological data is used to simulate two years, 2009 and 2010, for one of the covers, Test II. The complete profile of the cover is simulated and a water lateral boundary condition is included to account for the expected lateral drainage. The model is calibrated with data from the monitoring system (suction and temperature). Results show that the top layers are highly effective minimizing percolation. The first two layers (topsoil and soil) are retaining the infiltrated water during the rainfall period until is evapotranspirated during the dry season. The second layer (soil) and the third one (pebble layer) are acting as a capillary barrier hindering infiltration to the underlying materials. In fact, what field data displays is that this first capillary barrier fails during the rainy season, but the model is not reproducing this water entry. This difference between data and simulation is because water flows through the pebble layer via fingers and this mechanism is not present in our actual numerical model. Water balance display that the first layer is effectively generating runoff, which increases during the second year (30% of the precipitation in 2009 and 45% in 2010). Lateral drainage is also occurring and represents approximately the 5% of the rainfall. Evaporation is high both years, especially during the summer, and increases after rainfall events. The energy balance shows higher fluxes during the summer where sensible energy flux is much higher than

latent energy flux. During the winter, sensible and latent energy fluxes are almost equal. To be able to study water fluxes through the base of the cover, preferential flow needs to be included the numerical model.

Appendix A

This appendix is an extract from the user's guide (*Saaltink et al.*, 2008) of the program RetrasoCodeBright (RCB). A description of the dip and strike feature, which is not present in the current manual, can be found at the end of this appendix.

Atmospheric Boundary Conditions

RCB permits the simulation of meteorological/atmospheric phenomena, such as rain, evaporation, radiation and heat exchange between soil/atmosphere. These phenomena are simulated as flow boundary conditions for the three components (water, air and heat) written as functions of the state variables (P_l, P_g and T) or dependent variables (S_l, ω_g^w) and meteorological data that vary in time (atmospheric temperature and pressure, relative humidity, cloud index, rain fall and wind velocity). In what follows, these functions will be explained. Note, that positive fluxes are always considered into the modelled domain and negative fluxes outward. For instance, evaporation normally is negative, because it is a flux outward the domain.

The flux of water (j^w) is the sum of rainfall (P), evaporation (E), advective flux of vapour by the gas phase (j_g^w) and of surface runoff (j_{sr}):

$$j_w = P + E + j_g^w + j_{sr} \tag{1}$$

Evaporation is given by an aerodynamic diffusion relation:

$$E = \frac{k^2 v_a \phi}{\left(\ln \frac{z_a}{z_0}\right)^2} \left(\rho_{va} - \rho_v\right) \tag{2}$$

where ρ_{va} and ρ_v are the absolute humidity (mass of vapour per volume of gas, which can be calculate from relative humidity, H_r, and temperature) of the atmosphere and at the node of the boundary condition, respectively, k is the von Karman's constant (= 0.4), ϕ is the stability factor, z_0 is the roughness length, v_a is the wind velocity and z_a is the screen height at which v_a and ρ_{va} are measured. In theory, ρ_v must be the value at roughness length (z_0). Instead, RCB calculates ρ_v from the state variables at the node of the boundary condition. Hence, the same values are assumed at this node and at z_0.

The advective flux of vapour by the gas phase (j_g^w) is given by:

$$\begin{cases} j_g^w = \omega_g^w q_g & P_g > P_{ga} \\ j_g^w = \dfrac{\rho_{va}}{\rho_{ga}} q_g & P_g \le P_{ga} \end{cases} \tag{3}$$

where P_{ga} is the atmospheric pressure, ρ_{ga} is the atmospheric gas density and q_g is the flux of the gas phase:

$$q_g = \gamma_g \left(P_g - P_{ga} \right) \tag{4}$$

where γ_g is a leakage coefficient. Surface runoff (j_{sr}) is written as:

$$\begin{cases} J_{sr} = \gamma_w \left(p_l - p_{ga} \right) & P_l > P_{ga} \\ J_{sr} = 0 & P_l \le P_{ga} \end{cases} \tag{5}$$

where γ_w is another leakage coefficient. It must be said that ponding is not explicitly simulated, that is, RCB does not have a special element representing storage of water in a pond. When one assumes no ponding a very high value for γ_w can be used (but no to high to avoid numerical instabilities). Then, if the soil is saturated ($P_l > P_{ga}$) all rainfall that cannot infiltrate will runoff.

For the flux of air only the advective part is considered:

$$J_a = \omega_g^a q_g = \left(1 - \omega_g^w \right) q_g \tag{6}$$

The energy flux (j_e) is divided into the sensible heat flux (H_s), convective or latent heat flux (H_c) and radiation (R_n):

$$J_e = H_s + H_c + R_n \tag{7}$$

The sensible heat flux (H_s) is, like evaporation, calculated through an aerodynamic diffusion relation:

$$H_s = \rho_{ga} C_a \frac{k^2 v_a \phi}{\left(\ln \frac{z_a}{z_0}\right)^2} \left(T_a - T_0\right) \tag{8}$$

where C_a is the specific heat of the gas. The convective or latent heat flux (H_c) is calculated taking into account the internal energy of liquid water, vapour and air:

$$H_c = h_v \left(E + J_{wg}\right) + h_{la} \left(P + J_{wl}\right) + h_{a0} J_a \tag{9}$$

where h_v, h_{la} and h_{a0} are the free energy of vapour, liquid water and air, respectively. These three properties depend on the temperature, for which the temperature of the node of the boundary is taken for h_v, and h_{a0} and the dew point, which depends on the atmospheric vapour pressure, for h_{la}.

The radiation (R_n) can be given as a measured data or it can be calculated as:

$$R_n = \left(1 - A_l\right) R_g + \varepsilon R_a - \varepsilon \sigma T^4 \tag{10}$$

where R_g is the direct solar short wave radiation, R_a is the long wave atmospheric radiation, A_l is the albedo, ε is the emissivity, σ is the Stefan-Boltzman constant (5.67×10^{-8} J s^{-1} m^{-2} K^{-4}). Both the albedo and emissivity are considered function of the liquid saturation (S_l):

$$A_l = A_d + \left(A_d - A_w\right)\left(S_l^2 - 2S_l\right) \tag{11}$$

$$\varepsilon = 0.9 + 0.05 S_l \tag{12}$$

where A_d and A_w are the dry and wet albedo. The long wave atmospheric radiation (R_a) depends on the atmospheric temperature and absolute humidity according to an empirical relation:

$$R_a = \sigma T_a^{\,4} \left(0.605 + 0.048 \sqrt{1370 \rho_{va}}\right) \tag{13}$$

The calculation of the solar radiation (R_g) takes into account the time of the day and the year according to:

$$\begin{cases} R_g = \dfrac{\pi R_G}{2d_s}\sin\left(\dfrac{\left(t - t_m + 0.5d_s\right)\pi}{d_s}\right) & t_m - 0.5d_s \le t \le t_m + 0.5d_s \\ R_g = 0 & \text{otherwise} \end{cases} \tag{14}$$

where d_s is the time span between sunrise and sunset and t_m is the time at noon and R_G is the daily solar radiation calculated by an empirical relation:

$$R_G = \int_{t_m - 0.5d_s}^{t_m + 0.5d_s} R_g dt = R_A\left(0.29\cos\lambda + 0.52 I_n\right) \tag{15}$$

where λ is the latitude and I_n is the cloud index (= 1 for a clear sky, = 0 for a completely clouded sky) and R_A is the daily solar radiation in absence of atmosphere:

$$R_A = S_0 r_s\left[\frac{d_d}{\pi}\cos\lambda\cos\delta\sin\left(\frac{\pi d_s}{d_d}\right) + d_s\sin\lambda\sin\delta\right] \tag{16}$$

where S_0 is the sun constant (= 1376 J m^{-2} s^{-1}), r_s is the relation between the average distance between the earth and the sun and that of a given moment, d_d is the duration of a day (= 86400 s) and δ is the declination of the sun. The values of d_s, r_s and δ are calculated as follows:

$$d_s = \frac{d_d}{\pi}\text{acos}\left(-\tan\lambda\tan\delta\right) \tag{17}$$

$$\begin{aligned} r_s = 1.00011 + 0.03422\cos\left(2\pi\frac{t - t_0}{d_a}\right) + 0.00128\sin\left(2\pi\frac{t - t_0}{d_a}\right) + \\ + 0.000179\cos\left(4\pi\frac{t - t_0}{d_a}\right) + 0.000077\sin\left(2\pi\frac{t - t_0}{d_a}\right) \end{aligned} \tag{18}$$

$$\delta = -\delta_{\max}\sin\left(2\pi\frac{t - t_s}{d_a}\right) \tag{19}$$

where d_a is the duration of a year (= 365.241 days = 3.15568×10^7 s), t_0 is the time of January first, t_s is the time when autumn starts (September 21th at the northern hemisphere) and δ_{max} is the maximum declination of the sun (= 0.4119 rad = 23.26°).

Dip and Strike Extension

The strike (σ) of an inclined plane is the orientation of a horizontal line on this plane, expressed as an angle relative to the north in clockwise direction. The dip (β) is the maximum angle between a horizontal plane and the inclined plane (see figure 1).

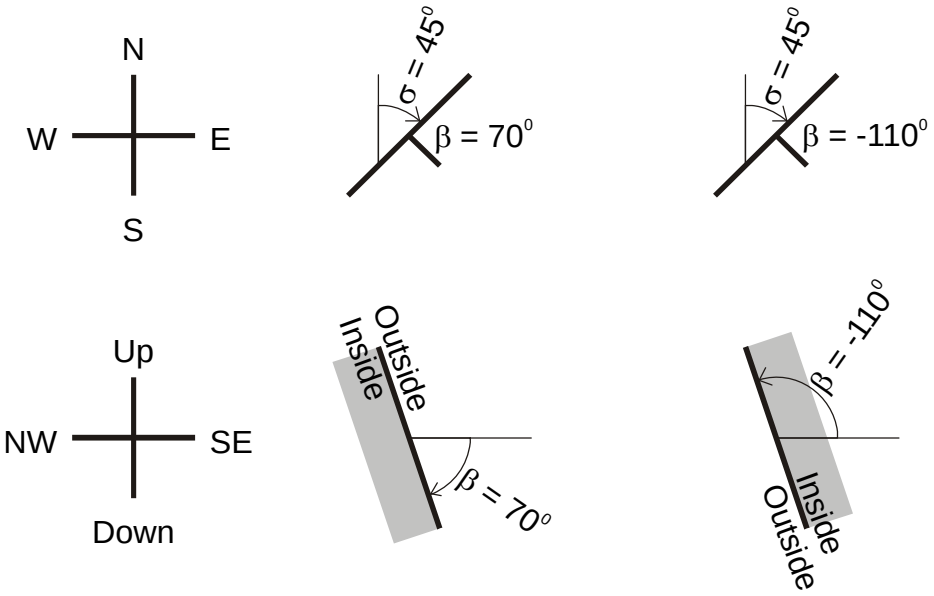

Figure A.1. Illustration of dip (β) and strike (σ). Note that a dip between -0.5π and 0.5π (-90^0 and 90^0) refers to a plane with its outside facing upwards. A dip between 1.5π and 0.5π (90^0 and 270^0) or between -1.5π and -0.5π refers to a plane with its outside facing downwards.

The vector **p** is a vector of length 1 orthogonal to the inclined plane pointing towards the outside. It can be calculated from the strike and dip as:

$$\mathbf{p} = \begin{pmatrix} \cos\sigma \sin\beta \\ -\sin\sigma \sin\beta \\ \cos\beta \end{pmatrix}$$

The vector **s** is a vector of length 1 pointing to the sun (*Blanco-Muriel*, 2001; *Sproul*, 2007).

$$\mathbf{s} = \begin{pmatrix} -\cos\delta\sin\theta \\ \sin\delta\cos - \cos\delta\sin\lambda\cos\theta \\ \cos\delta\cos\lambda\cos\theta + \sin\delta\sin\lambda \end{pmatrix} \quad \text{if } \lambda \geq 0 \text{ (Northern hemisphere)}$$

$$\mathbf{s} = \begin{pmatrix} -\cos\delta\sin\theta \\ -\sin\delta\cos + \cos\delta\sin\lambda\cos\theta \\ \cos\delta\cos\lambda\cos\theta + \sin\delta\sin\lambda \end{pmatrix} \quad \text{if } \lambda < 0 \text{ (Southern hemisphere)}$$

where θ is the solar time:

$$\theta = \frac{t - t_m}{d_d} 2\pi$$

where λ is the latitude and δ is the declination of the sun.

$$\delta = -\delta_{\max} \sin\left(\frac{t - t_a}{d_a} 2\pi \right)$$

Now, the solar radiation on the outside of an inclined plane can be calculated according to:

$$\begin{cases} R_g = S_0 r_s \left(0.29\cos\lambda + 0.52 I_n\right)\left(\mathbf{s} \bullet \mathbf{p}\right) & \text{if } \cos\zeta > 0 \wedge \left(\mathbf{s} \bullet \mathbf{p}\right) > 0 \\ R_g = 0 & \text{if } \cos\zeta \leq 0 \vee \left(\mathbf{s} \bullet \mathbf{p}\right) \leq 0 \end{cases}$$

Bibliography

Abdolahzadeh, A. M., B. L. Vachon, and A. R. Cabral (2011), Evaluation of the effectiveness of a cover with capillary barrier effect to control percolation into a waste disposal facility, *Can. Geotech. J.*, *48*(7), 996–1009, doi:10.1139/T11-017.

Abrol, I., J. Yadav, and F. Massoud (1988), *Salt-Affected Soils and their Management*, Food and Agriculture Organization of the United Nations. FAO soils bulletin 39, Rome 1988. M-53, ISBN 92-5-102686-6.

Aggelopoulos, C. A., and C. D. Tsakiroglou (2007), The longitudinal dispersion coefficient of soils as related to the variability of local permeability, *Water Air Soil Poll.*, *185*(1-4), 223–237, doi:10.1007/s11270-007-9445-6.

Albrecht, B., and C. Benson (2001), Effect of desiccation on compacted natural clays, *J. Geotech.and Geoenv. Eng.*, *127*(1), 67–75, doi:10.1061/(ASCE)1090-0241(2001)127:1(67).

Albright, W., and C. Benson (2003), Alternative cover assessment program 2002 annual report, *DRI publication 41182, Desert Research Institute, Univ. and Community College System of Nevada, Reno, Nev.*

Albright, W., C. Benson, G. Gee, A. Roesler, T. Abichou, P. Apiwantragoon, B. Lyles, and S. Rock (2004), Field water balance of landfill final covers, *J. Env. Quality*, *33*(6), 2317–2332.

Albright, W., C. Benson, and P. Apiwantragoon (2013), Field hydrology of landfill final covers

with composite barrier layers, *J. Geotech. Geoenv. Eng.*, *139*, 1–12, doi:10.1061/(ASCE)GT.1943-5606.0000741.

Albright, W. H., C. H. Benson, G. W. Gee, T. Abichou, E. V. McDonald, S. W. Tyler, and S. A. Rock (2006), Field performance of a compacted clay landfill final cover at a humid site, *J. Geotech.and Geoenv. Eng.*, *132*(11), 1393–1403, doi:10.1061/(ASCE)1090-0241(2006)132:11(1393).

Anderson, J. E., and A. D. Forman (2002), The protective cap/biobarrier experiment: a study of alternative evapotranspiration caps for the idaho national enineering and environmental laboratory, *Report no: Stoller-eser-46, 60 pp*.

Bea, S. A., J. Carrera, C. Ayora, F. Batlle, and M. W. Saaltink (2009), Cheproo: A fortran 90 object-oriented module to solve chemical processes in earth science models, *Computat. Geosci.*, *35*(6), 1098–1112.

Bea, S. A., J. Carrera, C. Ayora, and F. Batlle (2010), Modeling of concentrated aqueous solutions: Efficient implementation of pitzer equations in geochemical and reactive transport models, *Computat. Geosci.*, *36*, 526–538, doi:http://dx.doi.org/10.1016/j.cageo.2009.09.004.

Benson, C., G. Bohnhoff, and Api (2004), Comparison of model predictions and field data for an et cover, *Proc. Tailings and Mine Waste '04, Balkema, Leiden, The Netherlands*, pp. 137–142.

Benson, C., G. Bohnhoff, A. Ogorzalek, C. Shackelford, P. Apiwantragoon, and W. Albright (2005), *Field Data and Model Predictions for a Monolithic Alternative Cover*, pp. 1–16, Waste Containment and Remediation, doi:10.1061/40789(168)29.

Blanco-Muriel, M., D. Alarcon-Padilla, T. Lopez-Moratalla, and M. Lara-Coira (2001), Computing the solar vector, *Solar Energy*, *70*(5), 431–441, doi:10.1016/S0038-092X(00)00156-0.

Bohnhoff, G. L., A. S. Ogorzalek, C. H. Benson, C. D. Shackelford, and P. Apiwantragoon (2009), Field Data and Water-Balance Predictions for a Monolithic Cover in a Semiarid Climate,

J. Geotech.and Geoenv. Eng., *135*(3), 333–348, doi:10.1061/(ASCE)1090-0241(2009)135:3(333).

Boulet, G., I. Braud, and M. Vauclin (1997), Study of the mechanisms of evaporation under arid conditions using a detailed model of the soil-atmosphere continuum. Application to the EFEDA I experiment, *J. Hydrol.*, *193*(1-4), 114–141.

Burns, E. R., J. S. Selker, J. Y. Parlange, and R. B. Guenther (2006), Effects of sodium chloride on constitutive relations in variably saturated porous media, *Water Resour. Res.*, *42*(5), W05,405, doi:10.1029/2005WR004060.

Campbell, G. S., and J. M. Norman (1998), *An introduction to environmental biophysics*, Springer-Verlag, New York.

Carrera, J., H. Alfageme, and G. Galarza (1991), Estudio del transitorio de concentraciones en el acuífero de la fua., *Publicació técnica ENRESA*, *IT-35*, 90.

Dwyer, S. (1998), Alternative landfill covers pass the test, *Civil Eng.*, *68*(9), 50–52.

Dwyer, S. (2003), Water balance measurements and computer simulations of landfill covers, Ph.D. thesis, University of New Mexico, Alburquerque, NM.

Dwyer, S. F. (1997), Cost comparisons of alternative landfill final covers, in *Proc., Int. Contain. Tech. Conf.*, pp. 400–406, U.S. Dept. of Energy, Germantown, Md.

Edlefsen, N., and A. B. C. Anderson (1943), Thermodynamics of soil moisture, *Hilgardia*, *vol. 15, no. 2*, 31–298.

Fayer, M. J., and C. S. Simmons (1995), Modified soil-water retention functions for all matric suctions, *Water Resour. Res.*, *31*(5), 1233–1238.

Felmy, A. R., and J. H. Weare (1986), The prediction of borate mineral equilibria in natural-waters - application to searles lake, california, *Geochim. Cosmochim. Ac.*, *50*(12), 2771–2783.

Fujimaki, H., T. Shimano, M. Inoue, and K. Nakane (2006), Effect of a salt crust on evaporation from a bare saline soil, *Vadose Zone J.*, *5*(4), 1246–1256, doi:10.2136/vzj2005.0144.

Gaglio, M., W. Mackay, D. Padilla, R. Webb, and D. LeMOne (2001), The effectiveness of biobarrier layers within protective caps at preventing penetration of waste sites by the harvester ant pogonomyrmex salinus olsen, in *WM'01 Conference, Tucson, AZ.*

Galarza, G., J. Carrera, H. Alfageme, and M. De Andrés (2001), Simulation of infiltration processes in arid and semi-arid zones. application to the design of the fua engineering cover., *Boletín Geológico y Minero*, *112*(2), 37–50.

Gee, G., J. Felmy, D.G.and Ritter, M. Campbell, J. Downs, M. Fayer, R. Kirkham, and S. Link (1993), Field lysimeter test facility status report iv: Fy 1993, *Tech. rep.*, Pacific Northwest Laboratory, Richland, Wash., doi:10.2172/10194920.

Gee, G., C. Benson, and W. Albright (2006), Comment on "Evaluation of evapotranspirative covers for waste containment in arid and semiarid regions in the southwestern USA", *Vadose Zone J.*, *5*(2), 809–812, doi:10.2136/vzj2005.0090.

Gens, A., M. Sanchez, L. D. N. Guimaraes, E. E. Alonso, A. Lloret, S. Olivella, M. V. Villar, and F. Huertas (2009), A full-scale in situ heating test for high-level nuclear waste disposal: observations, analysis and interpretation, *Geotechnique*, *59*(4), 377–399, doi:10.1680/geot.2009.59.4.377.

Gowing, J. W., F. Konukcu, and D. A. Rose (2006), Evaporative flux from a shallow watertable: The influence of a vapour-liquid phase transition, *J. Hydrol.*, *321*(1-4), 77–89.

Gran, M., J. Carrera, J. Massana, M. Saaltink, S. Olivella, C. Ayora, and A. Lloret (2011), Dynamics of water vapor flux and water separation processes during evaporation from a salty dry soil, *J. Hydrol.*, *396*(3-4), 215 – 220, doi:10.1016/j.jhydrol.2010.11.011.

Hammarstrom, J., R. S. II, A. Meier, and J. Kornfeld (2005), Secondary sulfate minerals associated

with acid drainage in the eastern us: recycling of metals and acidity in surficial environments, *Chem. Geol.*, *215*(1-4), 407 – 431.

Heitman, J. L., R. Horton, T. Ren, I. N. Nassar, and D. D. Davis (2008), A test of coupled soil heat and water transfer prediction under transient boundary temperatures, *Soil Sci. Soc. Am. J.*, *72*(5), 1197–1207, doi:10.2136/sssaj2007.0234.

Ho, C., and S. Webb (1998), Capillary barrier performance in heterogeneous porous media, *Water Resour. Res.*, *34*(4), 603–609, doi:10.1029/98WR00217.

Hopp, L., J. McDonnell, and P. Condon (2011), Lateral Subsurface Flow in a Soil Cover over Waste Rock in a Humid Temperate Environment, *Vadose Zone J.*, *10*(1), 332–344, doi:10.2136/vzj2010.0094.

Hu, J., X. D. Xiao, D. F. Ogletree, and M. Salmeron (1995), Imaging the condensation and evaporation of molecularly thin-films of water with nanometer resolution, *Science*, *268*(5208), 267–269.

Huinink, H. P., L. Pel, and M. A. J. Michels (2002), How ions distribute in a drying porous medium: A simple model, *Phys. Fluids*, *14*(4), 1389–1395, doi:10.1063/1.1451081.

Jackson, R. D., R. J. Reginato, B. A. Kimball, and F. S. Nakayama (1974), Diurnal soil-water evaporation - comparison of measured and calculated soil-water fluxes, *Soil Sci. Soc. Am. J.*, *38*(6), 861–866.

Jessberger, H., and K. Stone (1991), Subsidence effects on clay barriers, *Geotechnique*, *41*(2), 185–194.

Jimenez-Martinez, J., K. Tamoh, L. Candela, F. J. Elorza, and D. Hunkeler (2012), Multiphase transport of tritium in unsaturated porous media-bare and vegetated soils, *Mathematical Geosciences*, *44*(2, SI), 187–208, doi:10.1007/s11004-012-9383-8.

Kelly, S. F., and J. S. Selker (2001), Osmotically driven water vapor transport in unsaturated soils, *Soil Sci. Soc.Am. J.*, *65*(6), 1634–1641.

Khire, M., C. Benson, and P. Boscher (1994), Final cover hydrologic evaluation - phase iii, *Envir. Geotech. Rep.94-4. Dep. Civil and Envir. Eng., University of Wisconsin, Madison, Wisc.*

Khire, M., C. Benson, and P. Bosscher (1999), Field data from a capillary barrier and model predictions with unsat-h, *J. Geotech. Geoenv. Eng.*, *125*(6), 518–527, doi:10.1061/(ASCE) 1090-0241(1999)125:6(518).

Khire, M., C. Benson, and P. Bosscher (2000), Capillary barriers: Design variables and water balance, *J. Geotech.and Geoenv. Eng.*, *126*(8), 695–708, doi:10.1061/(ASCE)1090-0241(2000) 126:8(695).

Khire, M., C. Benson, and P. Bosscher (1997), Water balance modeling of earthen final covers, *J. Geotech.and Geoenv. Eng.*, *123*(8), 744–754, doi:10.1061/(ASCE)1090-0241(1997)123: 8(744).

Konucku, F., A. Istanbulluoglu, and I. Kocaman (2004), Determination of water content in drying soils: incorporating transition from liquid phase to vapour phase, *Aust. J. Soil Res.*, *42*(1), 1–8.

Lasaga, A. C. (1998), *Kinetic Theory in the Earth Sciences*, 728 pp pp., Princeton University Press.

Milly, P., and P. Eagleson (1982), Parameterization of moisture and heat fluxes across the land surface for use in atmospheric general circulation models, *Tech. Rep. 279*, R.M. Parsons Laboratory, Dept. of Civil Eng., MIT, Cambridge.

Milly, P. C. D. (1996), Effects of thermal vapor diffusion on seasonal dynamics of water in the unsaturated zone, *Water Resour. Res.*, *32*(3), 509–518.

Miranda, P. B., V. Pflumio, H. Saijo, and Y. R. Shen (1997), Conformation of surfactant monolayers at solid/liquid interfaces, *Chem. Phys. Lett.*, *264*(3-4), 387–392.

Morris, C., and J. Stormont (1997), Capillary barriers and subtitle D covers: Estimating equivalency, *J. Env. Eng. ASCE*, *123*(1), 3–10, doi:10.1061/(ASCE)0733-9372(1997)123:1(3).

Murray, F. W. (1967), On the computation of saturation vapor pressure, *J. Appl. Meteor.*, *6*, 203–204, doi:http://dx.doi.org/10.1175/1520-0450(1967)006⟨0203:OTCOSV⟩2.0.CO;2.

Nachshon, U., N. Weisbrod, M. I. Dragila, and A. Grader (2011), Combined evaporation and salt precipitation in homogeneous and heterogeneous porous media, *Water Resour. Res.*, *47*, W03,513, doi:10.1029/2010WR009677.

Nassar, I., and R. Horton (1989a), Water transport in unsaturated non-isothermal salty soil. 1. Experimental results, *Soil Sci. Soc. Am. J.*, *53*(5), 1323–1329.

Nassar, I. N., and R. Horton (1989b), Water transport in unsaturated non-isothermal salty soil .2. Theoretical Development, *Soil Sci. Soc. Am. J.*, *53*(5), 1330–1337.

Nassar, I. N., R. Horton, and A. M. Globus (1992), Simultaneous transfer of heat, water, and solute in porous-media .2. Experiment and Analysis, *Soil Sci. Soc. Am. J.*, *56*(5), 1357–1365.

Nimmo, J. R. (2012), Preferential flow occurs in unsaturated conditions, *Hydrol. Processes*, *26*(5), 786–789, doi:{10.1002/hyp.8380}.

Nyhan, J., T. Hakonson, and B. Drennon (1990), A water-balance study of 2 landfill cover desings for semiarid regions, *J. Env. Quality*, *19*(2), 281–288.

Odelius, M., M. Bernasconi, and M. Parrinello (1997), Two dimensional ice adsorbed on mica surface, *Phys. Rev. Lett.*, *78*(14), 2855–2858.

Ogorzalek, A., G. Bohnhoff, C. Shackelford, C. Benson, and P. Apiwantragoon (2008), Comparison of field data and water-balance predictions for a capillary barrier cover, *J. Geotech.and Geoenv. Eng.*, *134*(4), 470–486, doi:10.1061/(ASCE)1090-0241(2008)134:4(470)).

Olivella, S., J. Carrera, A. Gens, and E. E. Alonso (1994), Nonisothermal multiphase flow of brine and gas through saline media, *Transp. Porous Media*, *15*(3), 271–293.

Olivella, S., J. Carrera, A. Gens, and E. E. Alonso (1996a), Porosity variations in saline media caused by temperature gradients coupled to multiphase flow and dissolution/precipitation, *Transp. Porous Media*, *25*(1), 1–25.

Olivella, S., J. Carrera, A. Gens, and E. E. Alonso (1996b), Porosity variations in saline media caused by temperature gradients coupled to multiphase flow and dissolution/precipitation, *Transp. Porous Media*, *25*(1), 1–25.

Olivella, S., A. Gens, J. Carrera, and E. E. Alonso (1996c), Numerical formulation for a simulator (code_bright) for the coupled analysis of saline media, *Eng. Computations*, *13*(7), 87–112.

Peng, S., and H. Jiang (2009), A review on soil cover in waste and contaminant containment: design, monitoring, and modeling, *Frontiers of Earth Science in China*, *3*(3), 303–311, doi: 10.1007/s11707-009-0046-0.

Philip, J. R., and D. A. de Vries (1957), Moisture movement in porous materials under temperature gradient, *EOS Trans., AGU*, *38*, 222–232.

Pitzer, K. S. (1973), Thermodynamics of electrolytes .1. theoretical basis and general equations, *J. Phys. Chem.*, *77*(2), 268–277.

Prunty, L. (2003), Soil water retention and conductivity when vapor flow is important, *J. Irrigation and Drainage Eng.-Asce*, *129*(3), 201–207.

Rakhmatkariev, G. (2006), Mechanism of adsorption of water vapor by muscovite: A model based on adsorption calorimetry, *Clays and Clay Minerals*, *54*(3), 402–407, doi:10.1346/CCMN. 2006.0540311.

Rezanezhad, F., H.-J. Vogel, and K. Roth (2006), Experimental study of fingered flow through initially dry sand, *Hydrol. Earth Syst. Sci. Discussions*, *3*(4), 2595–2620, doi:10.5194/ hessd-3-2595-2006.

Ross, B. (1984), A conceptual model of deep unsaturated zones with negligible recharge, *Water Resour. Res.*, *20*(11), 1627–1629, doi:10.1029/WR020i011p01627.

Ross, P. J., J. Williams, and K. L. Bristow (1991), Equation for extending water-retention curves to dryness, *Soil Sci. Soc. Am. J.*, *55*(4), 923–927.

Rossi, C., and J. R. Nimmo (1994), Modeling of soil-water retention from saturation to oven dryness, *Water Resour. Res.*, *30*(3), 701–708.

Rutten, M. M., S. C. Steele-Dunne, J. Judge, and N. van de Giesen (2010), Understanding Heat Transfer in the Shallow Subsurface Using Temperature Observations, *Vadose Zone J.*, *9*(4), 1034–1045, doi:10.2136/vzj2009.0174.

Saaltink, M., C. Ayora, and S. Olivella (2008), *User's guide for RetrasoCodeBright (RCB) and VisualRetraso*, Dep. of Geotechnical Eng. and Geo-Sciences, Tech. Univ. of Catalonia (UPC), Institute of Earth Sciences Jauma Almera, Spanish Research Council (CSIC),Barcelona, Spain.

Saaltink, M. W., C. Ayora, and J. Carrera (1998), A mathematical formulation for reactive transport that eliminates mineral concentrations, *Water Resour. Res.*, *34*(7), 1649–1656.

Saaltink, M. W., F. Batlle, C. Ayora, J. Carrera, and S. Olivella (2004), Retraso, a code for modeling reactive transport in saturated and unsaturated porous media, *Geol. Acta*, *2(3)*, 235–251.

Saito, H., J. Simunek, and B. P. Mohanty (2006), Numerical analysis of coupled water, vapor, and heat transport in the vadose zone, *Vadose Zone J.*, *5*(2), 784–800.

Sakai, M., N. Toride, and J. Simunek (2009), Water and vapor movement with condensation and evaporation in a sandy column, *Soil Sci. Soc. Am. J.*, *73*(3), 707–717.

Scanlon, B., R. Reedy, K. Keese, and S. Dwyer (2005), Evaluation of evapotranspirative covers for waste containment in arid and semiarid regions in the southwestern usa, *Vadose Zone J.*, *4*(1), 55–71.

Scanlon, B., S. Tyler, and P. Wierenga (1997), Hydrologic issues in arid, unsaturated systems and implications for contaminant transport, *Reviews of Geophysics*, *35*(4), 461–490, doi:10.1029/97RG01172.

Scanlon, B. R. (1992), Evaluation of liquid and vapor water-flow in desert soils based on cl-36 and tritium tracers and nonisothermal flow simulations, *Water Resour. Res.*, *28*(1), 285–297.

Scanlon, B. R., and P. C. D. Milly (1994), Water and heat fluxes in desert soils .2. Numerical Simulations, *Water Resour. Res.*, *30*(3), 721–733.

Schneider-Zapp, K., O. Ippisch, and K. Roth (2010), Numerical study of the evaporation process and parameter estimation analysis of an evaporation experiment, *Hydrol. Earth Syst. Sci.*, *14*(5), 765–781.

Schneider-Zapp, K., O. Ippisch, and K. Roth (2010), Numerical study of the evaporation process and parameter estimation analysis of an evaporation experiment, *Hydrol. Earth Syst. Sci (HESS)*, *14*(5), 765–781, doi:10.5194/hess-14-765-2010.

Scotter, D. R. (1974), Salt and water movement in relatively dry soil, *Aust. J. Soil Res.*, *12*(1), 27–35.

Selker, J. (1997), Design of interface shape for protective capillary barriers, *Water Resour. Res.*, *33*(1), 259–260, doi:{10.1029/96WR03138}.

Sghaier, N., M. Prat, and S. Ben Nasrallah (2007), On ions transport during drying in a porous medium, *Transport Porous Med.*, *67*(2), 243–274, doi:10.1007/s11242-006-9007-1.

Shokri, N., P. Lehmann, and D. Or (2010), Liquid-phase continuity and solute concentration dynamics during evaporation from porous media: Pore-scale processes near vaporization surface, *Phys. Review E*, *81*(4), 046,308, doi:10.1103/PhysRevE.81.046308.

Shuttleworth, W. J. (2007), Putting the ”vap” into evaporation, *Hydrol. Earth Syst. Sci.*, *11*(1), 210–244.

Smith, E., R. Luxmore, and S. G.W. (1997), Natural physical and biological processes compromise the long-term integrity of compacted clay caps., *Barrier Technologies for Environmental Management: Summary of a Workshop. National Academy Press*.

Sproul, A. (2007), Derivation of the solar geometric relationships using vector analysis, *Renewable Energy*, *32*(7), 1187–1205, doi:10.1016/j.renene.2006.05.001.

Thorstenson, D. C., and D. W. Pollock (1989), Gas-transport in unsaturated zones - multicomponent systems and the adequacy of fick laws, *Water Resour. Res.*, *25*(3), 477–507.

Van-Camp, L., B. Bujarrabal, A.-R. Gentile, J. R.J.A., L. Montanarella, C. Olazabal, and S.-K. Selvaradjou (2004), Reports of the tech. working groups established under the thematic strategy for soil protection, *Tech. rep.*, EUR 21319 EN/2, 872 pp.. Office for Official Publications of the European Communities, Luxembourg.

van Genuchten, M. (1980), A closed-form equation for predicting the hydraulic conductivity of unsaturated soils, *Soil Sci. Soc. Am. J.*, *44*, 892–898.

Villar, M. (2011), Resultados de los ensayos de caracterización de los materiales de cobertera, *Informe técnico CIEMAT/DMA/2G208/06/11*.

Villar, M., and A. Fernández (2011), Caracterización de materiales de confinamiento de base hormigón/arcilla, *Informe técnico CIEMAT/DMA/2G208/1/12*.

Ward, A., and G. Gee (1997), Performance evaluation of a field-scale surface barrier, *J. Env. Quality*, *26*(3), 694–705.

Waugh, W., M. Thiede, D. Bates, L. Cadwell, G. Gee, and C. Kemp (1994), Plant cover and water-balance in gravel admixtures at an arid waste-burial site, *J. Env. Quality*, *23*(4), 676–685.

Webb, S. W., and K. Pruess (2003), The use of fick's law for modeling trace gas diffusion in porous media, *Transport Porous Med.*, *51*(3), 327–341.

Wheeting, L. C. (1925), Certain relationships between added salts and the moisture of soils, *Soil Sci.*, *19*(4), 287–299.

Yakirevich, A., P. Berliner, and S. Sorek (1997), A model for numerical simulating of evaporation from bare saline soil, *Water Resour. Res.*, *33*(5), 1021–1033.

Zheng, Z. P., G. X. Zhang, and J. M. Wan (2008), Reactive transport modeling of column experiments on the evolution of saline-alkaline waste solutions, *J. Contaminant Hydrol.*, *97*(1-2), 42–54, doi:10.1016/j.jconhyd.2007.12.002.